Development of Functional Optical Coherence Tomography for Structural and Microangiography Assessment of Heart and Skin

Zhiying Xie

A dissertation
submitted in partial fulfillment of the
requirements for the degree of

Doctor of Philosophy

University of Washington

2025

Reading Committee:
Ruikang K. Wang, Chair
Ying Zheng
Steven L. Jacques

Program Authorized to Offer Degree:
Bioengineering

University of Washington

Abstract

Development of Functional Optical Coherence Tomography for Structural and Microangiography Assessment of Heart and Skin

Zhiying Xie

Chair of the Supervisory Committee:
Ruikang K. Wang
Department of Bioengineering

This thesis explores the potential of developing functional Optical Coherence Tomography (OCT) in structural and microangiographic applications for heart and skin tissues. OCT, as a noninvasive imaging technique, has revolutionized fields such as ophthalmology, cardiology, and dermatology by offering high-resolution visualization of biological structures and microvasculature. However, its capacity to capture physiological characterization, both qualitative and quantitatively, remains limited. This research seeks to bridge the gap by advancing functional OCT techniques to provide novel insights into tissue and vascular behavior in complex vascularized areas like coronary microcirculation and skin.

In **Chapter 1**, the thesis introduces OCT principles and their clinical significance for noninvasive imaging. **Chapter 2** delves into advanced OCT techniques for assessing microvascular networks and tissue composition. Methods such as Optical Microangiography (OMAG) and OCT velocimetry are presented to demonstrate OCT's ability to visualize capillary morphology and blood flow without contrast agents and to characterize hemodynamic properties and microvascular health quantitatively. Additionally, OCT structural imaging technique, such as calibrated optical attenuation coefficient (OAC), is presented to differentiate tissue compositions in distinct skin layers based on scattering properties.

In **Chapter 3**, OCT Angiography (OCTA) is applied to assess microvascular damage

in infarcted hearts, uncovering structural and functional changes post-myocardial infarction (MI), such as capillary loss, vessel enlargement, and altered blood flow— insights for understanding coronary network remodeling. **Chapter 4** investigates OCTA's ability to detect depth-resolved distinct blood flow signals and pulse patterns across different skin layers, which offers potential applications in non-invasive cardiovascular monitoring.

Chapter 5 explores OCT's dermatological applications in monitoring skin aging, UV-induced changes, and light-tissue interactive behaviors. It demonstrates OCT's ability to detect subclinical changes—such as vessel dilation, epidermal thickening, and structural organization differences—before clinically visible signs appear, supporting early intervention.

Contents

ACKNOWLEDGEMENT

First and foremost, I would like to express my deepest gratitude to my PhD mentor and advisor, Professor **Ruikang K. Wang**. Although my background was not initially aligned with his specific research area, he believed in my potential, provided thorough training, and always patiently answered my many questions. Thank you for your patience and for allowing me to grow and improve slowly but organically. His support allowed me to explore my curiosity, often leading to new ideas and findings. Since joining Professor Wang's lab, I have been immensely grateful for his encouragement, patience, and the nurturing environment he fostered, which enabled my personal and professional growth. My PhD experience and the outcome of this thesis would have been vastly different without his mentorship and unwavering support.

I am also deeply thankful to my PhD dissertation committee members, Professors **Ying Zheng** and **Steven L. Jacques**, for dedicating their time to review my work and provide valuable feedback and to Professor **Jia Zhu**, my Graduate School Representative, for ensuring my research met the high standards expected of graduate students. Their insights and guidance have strengthened my work in countless ways.

A special acknowledgment goes to dear Professor **Ying Zheng** and Professor **Charles E. Murry**, whose collaborative support and encouragement have constantly motivated me throughout my PhD journey. Professor Zheng's kindness, collaborative spirit, and dedication to research have profoundly impacted my work and personal growth. Their collaboration opened new doors for me in heart microvasculature research, an impactful and novel field that remains underexplored. I am grateful for their guidance, which has inspired me to contribute to a field with such potential.

I am immensely grateful for your wisdom and guidance for dear Professor **Steven L. Jacques**, which led me to tissue optics and skin imaging. Your encouragement has rekindled my passion for research and shown me that my curiosity and courage to explore scientific gaps are alive and well, even through the challenges of a PhD. Your dedication to teaching, enthusiasm for science, and depth of knowledge have inspired me to envision the kind of researcher I aspire to become. Thank you for your guidance and encouragement and the many enjoyable moments we shared.

Finally, I wish to extend my heartfelt thanks to my parents, dear Dr. **Yun Wang** and Dr. **Jinsheng Xie**, and my husband, dear **Yangyang Liu**, whose support and encouragement have been the foundation of all my achievements. None of this would have been possible without their love, guidance, and inspiration. I hope, in some small way, I have made them proud and brought them happiness.

Dedication

To my dear parents, husband, and friends.

1 INTRODUCTION

OCT is revolutionizing biomedical imaging for diagnostics and research, bridging the gap by delivering high-resolution insights into tissue and microvasculature.

This thesis explores innovative methodologies for functional Optical Coherence Tomography (OCT) with applications across heart and skin imaging. The primary objective is to demonstrate new functional OCT's capabilities in visualizing and quantifying microvascular structures, such as providing assessments of vessel remodeling in ischemic heart disease or diving deep into optical attenuation coefficient (OAC) for measuring tissue properties quantitatively in characterizing tissue nanostructure and composition.

1.1 Optical Coherence Tomography

Optical Coherence Tomography (OCT) is a non-invasive imaging technique that has revolutionized biomedical imaging since its introduction in 1991. It enables high-resolution, three-dimensional imaging of biological tissues without the need for contrast agents, making it particularly well-suited for in vivo applications. OCT is especially effective for imaging the human eye, which has relatively transparent optical properties. Over the past decade, OCT has transformed ophthalmology by enabling detailed structural and functional imaging, significantly benefiting clinical practice and research.

OCT operates on the principle of low-coherence interferometry, using a near-infrared light source directed into tissue. Different tissue layers partially reflect light, and the backscattered light

is compared to light reflected from a reference mirror within an interferometer, creating an interference pattern that encodes depth information. This allows for depth-resolved imaging with micrometer-scale resolution by measuring the time delay of backscattered light, corresponding to its path length in the tissue.

Advancements in OCT technology include the shift from Time-Domain OCT (TD-OCT) to Fourier-Domain OCT (FD-OCT), which encompasses Spectral-Domain OCT (SD-OCT) and Swept-Source OCT (SS-OCT). SD-OCT captures a full spectrum of light simultaneously, enabling faster image acquisition but with limited depth penetration. In contrast, SS-OCT employs a tunable laser that sweeps through wavelengths, allowing for deeper tissue penetration, faster acquisition, and improved sensitivity, which is particularly beneficial for imaging deeper structures like the choroid and sclera in the eye.

OCT's applications extend beyond ophthalmology, including endoscopic imaging for internal organs, dermatology for high-precision skin lesion assessment, and cardiac imaging for visualizing coronary arteries and cardiovascular conditions. OCT continues establishing itself as an essential tool in clinical and research environments. The evolution of its technology, particularly through advancements in FD-OCT and SS-OCT, has significantly expanded its capabilities, offering valuable insights into a wide range of biological tissues and promising further breakthroughs in imaging.

1.1.1 Technical Background: Principles of OCT

Optical Coherence Tomography (OCT) is a pivotal imaging modality in biomedical applications, particularly in ophthalmology. The foundational principle of OCT is Michelson interferometry, a concept that has existed for over a century. The technology can be classified into two primary categories: Time-Domain OCT (TD-OCT) and Fourier-Domain OCT (FD-OCT). The initial suggestions for utilizing OCT in imaging applications emerged in the 1990s, but it was the development of FD-OCT that catalyzed the rapid development of OCT applications. FD-OCT leverages the Fourier transformation of spectral interference data to generate depth-resolved images

efficiently. This technique allows for the simultaneous acquisition of depth information without the need for mechanical movement of the reference mirror, which is a notable advantage over TD-OCT.

The interference signal $I(k)$ in FD-OCT can be mathematically expressed as:

$$I(k) = S(k)\big(r_R^2 + r_S^2 + 2r_R r_S \cos(2k\Delta z)\big)$$

Where $S(k)$ is the source spectral intensity as a function of wavenumber $k = \frac{2\pi}{\lambda}$, r_R and r_S are the reflectivities of the reference and sample arms, respectively, and Δz is the optical path length difference between the reference arm and a specific depth in the sample. The cosine term encodes depth information, producing a fringe pattern that varies with depth. Structures located deeper within the sample generate higher-frequency components in the interferogram, which are essential for reconstructing the depth profile.

To retrieve the depth profile from the interference signal, an inverse Fourier transform is performed:

$$I(z) = \mathcal{F}^{-1}\{I(k)\}$$

This operation transforms the frequency-domain signal into the spatial (depth) domain, yielding a depth-resolved reflectivity profile $I(z)$, commonly referred to as an A-scan. z is related to the optical path length difference Δz. This profile reveals the reflectivity of structures at various depths within the sample, effectively mapping the internal architecture of the tissue.

FD-OCT is primarily implemented in two modalities: Spectral-Domain OCT (SD-OCT) and Swept-Source OCT (SS-OCT). Both techniques utilize the principles of low-coherence interferometry but differ in their operational mechanisms. SD-OCT employs a broadband light source and a spectrometer equipped with a CCD or line-scan camera to capture all wavelengths simultaneously. The spectrometer splits the interference pattern into its constituent wavelengths, allowing for the simultaneous recording of the spectral interferogram. This parallel acquisition of

spectral data enables faster imaging speeds and improved sensitivity compared to TD-OCT. However, SD-OCT is limited by its depth penetration due to the spectral resolution of the light source.

SS-OCT uses a tunable laser that sweeps across a range of wavelengths sequentially. A single photodiode detects the interference pattern over time as the wavelength sweeps, creating a spectral interferogram. This technique offers deeper tissue penetration and faster acquisition times compared to SD-OCT. Sequentially acquiring spectral data allows for enhanced sensitivity and the ability to visualize structures that are challenging to image with SD-OCT.

In summary, Optical Coherence Tomography has evolved significantly from its initial concepts to become a cornerstone of biomedical imaging. The transition from Time-Domain to Fourier-Domain techniques, particularly the advancements in Spectral-Domain and Swept-Source OCT, has enhanced the capabilities of OCT, allowing for high-speed, high-resolution imaging of biological tissues. As research continues exploring new applications and refining existing technologies, OCT is poised to remain a vital tool in clinical and research settings.

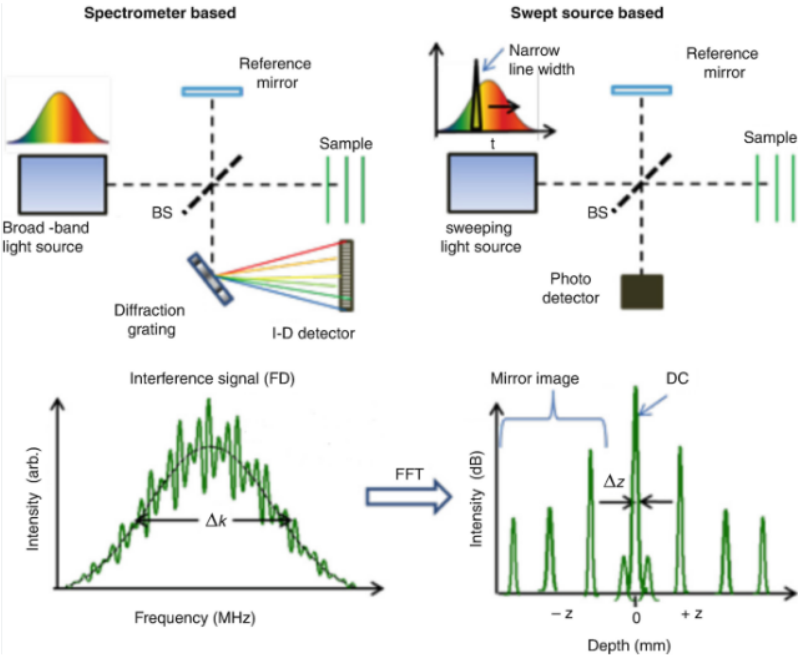

Figure 1.1: Schematic representation of spectrometer-based and swept-source-based Fourier-domain Optical Coherence Tomography (FD-OCT) systems. Figure adapted from [29]

1.1.2 Axial and Lateral Resolution in Fourier-Domain OCT

While the axial resolution in Fourier-Domain OCT (FD-OCT) is primarily determined by the spectral bandwidth of the light source, the lateral resolution depends on the focusing optics used in the system. Lateral resolution refers to the ability of the OCT system to distinguish fine details in the plane perpendicular to the imaging depth (x-y plane). It is influenced by the numerical aperture (NA) of the objective lens and the wavelength of the light source.

In OCT, there is often a trade-off between lateral and axial resolution: Increasing the NA improves lateral resolution but reduces the depth of field, resulting in a more limited range over which high lateral resolution is maintained. The axial resolution is not affected by NA but is determined by the light source's spectral bandwidth.

As a result, OCT systems must balance axial and lateral resolution requirements depending on the imaging application. For example, retinal imaging often prioritizes high axial resolution to resolve retinal layers, while skin imaging may require high lateral resolution for cellular-level detail over a large depth range.

The axial resolution in FD-OCT depends on the spectral bandwidth of the source and is given by:

$$\text{Axial Resolution} \approx \frac{2\ln(2)}{\pi} \cdot \frac{\lambda_0^2}{\Delta\lambda} \tag{1.1}$$

Where λ_0 is the central wavelength of the light source, $\Delta\lambda$ is the full width at half maximum (FWHM) of the source spectrum. A broader bandwidth $\Delta\lambda$ results in a narrower point spread function (PSF) along the depth axis, improving the axial resolution. The axial PSF in FD-OCT is primarily determined by the source's coherence length, which limits the system's ability to resolve structures along the depth axis.

The lateral resolution in OCT is approximated by:

$$\text{Lateral Resolution} \approx \frac{0.61\lambda_0}{\text{NA}} \tag{1.2}$$

Where λ_0 is the central wavelength of the light source, NA and is the numerical aperture of the objective lens. A higher NA results in better lateral resolution, allowing the light beam to be focused more tightly in the lateral dimension.

Unlike axial resolution, which remains nearly constant throughout the imaging depth, the lateral resolution in OCT is depth-dependent. OCT systems have a focal plane where the lateral PSF is narrowest, providing the best lateral resolution. As you move away from this focal plane, either above or below, the lateral PSF broadens due to the divergence of the Gaussian beam. This effect, known as depth-dependent lateral resolution or lateral roll-off, reduces lateral resolution for structures farther from the focal plane.

The confocal parameter b, also called the depth of field, defines the depth range over which good lateral resolution is maintained. It is given by:

$$b = \frac{2\lambda_0}{\mathrm{NA}^2} \tag{1.3}$$

This parameter indicates the range along the depth axis over which the lateral PSF remains relatively focused. Structures outside this range will appear blurred in the lateral direction due to the defocusing effect.

1.1.3 Signal Roll-Off and Sensitivity

In FD-OCT, roll-off occurs, where signal sensitivity decreases with increasing depth. This roll-off is due to the detector or spectrometer's limited spectral resolution, which affects the ability to detect high-frequency components corresponding to deeper structures. A Gaussian decay model effectively represents the signal attenuation with depth. As depth increases, the interference fringes in the spectral interferogram produce higher spatial frequencies. However, the finite spectral resolution of the detector limits its ability to distinguish these high-frequency components, resulting in a progressive loss of sensitivity. This inability to resolve fine spectral details causes a decay in

signal intensity that resembles a Gaussian function. The Gaussian decay model can be expressed as:

$$I(z) \propto e^{-(\gamma z)^2} \tag{1.4}$$

where $I(z)$ is the intensity at depth z, and γ is a parameter reflecting the system's spectral resolution. This model captures how unresolved high frequencies blur together, creating a Gaussian-shaped attenuation of signal strength as depth increases. The Gaussian decay profile is thus particularly suitable for describing roll-off in OCT systems where spectral resolution constraints, rather than intrinsic absorption or scattering, dominate the sensitivity loss with depth.

1.1.4 Geometric Factor of Numerical Aperture (NA)

In OCT, the Geometric Factor G is used to quantify the impact of numerical aperture (NA) on the light collection efficiency and focusing properties of the system. G is often defined as an integral over the angular distribution of light, which considers both the Gaussian beam profile and the angular spread created by the NA.

The geometric factor G can be expressed as:

$$G_{\mathrm{NA}} \approx 1/cos(theta_c) \tag{1.5}$$

where θ is the angle from the optical axis; the Gaussian term represents the Gaussian intensity profile of the light beam $\cos\theta$ and $\sin\theta$ accounts for the projection and angular distribution of the light collection area in the system.

The $\cos\theta$ term accounts for this projection effect. When light is collected at an angle θ, the effective collection area along the direction of propagation is proportional $\cos\theta$, indicating that light collected at larger angles contributes less to the total detected signal. Additionally, as θ increases, the path length for light to reach the detector also increases, causing a natural drop-off in signal strength. The $\cos\theta$ term models this combined effect, representing the reduction in effective collection efficiency at higher angles.

The geometric factor G plays a crucial role in OCT system design, particularly in determining the appropriate NA for different imaging applications. A higher G is typically associated with high-NA objectives that maximize lateral resolution but may reduce depth of field. For shallow, high-resolution imaging tasks (e.g., retinal imaging), a higher NA and, consequently, a higher G are advantageous. Conversely, for applications requiring a larger depth of field (e.g., tissue imaging), a lower NA and a lower G are chosen to maintain consistent resolution over greater depths.

1.2 Modeling Tissue Scattering in OCT

Light scattering in biological tissues provides valuable information about the nanoarchitecture and organization of cells and subcellular structures. When light interacts with tissues, it encounters structures of various sizes, some larger and others smaller than the wavelength of light. The scattering properties depend on these structural dimensions relative to the wavelength, allowing OCT to probe and characterize cellular and tissue microstructure.

The scattering of light by tissue can be broadly divided into two categories. Mie scattering occurs when the scattering structures (e.g., organelles, cell nuclei, collagen fibers) are comparable in size toor less than the wavelength of light (typically 300–1300 nm). Rayleigh scattering occurs when the scattering structures are significantly smaller than the wavelength, producing a scattering intensity that decreases rapidly with increasing wavelength.

1.2.1 Scattering coefficient and anisotropy

In OCT applications, the scattering coefficient μ_s and anisotropy factor g are key parameters that describe the light-scattering properties of tissue. Based on the size distribution of tissue structures, these parameters can be modeled using Mie and Rayleigh scattering theories.

The scattering cross-section σ (in μm^2) represents the effective "shadow" area cast by a scattering particle, quantifying how much light is scattered by a single particle. The scattering coefficient μ_s (in μm^{-1}) is then given by:

$$\mu_s = \rho \cdot \sigma \tag{1.6}$$

where ρ is the number density of scatterers (in μm^{-3}). This coefficient indicates the probability of scattering per unit distance and is essential for quantifying tissue scattering. The anisotropy factor g describes the average cosine of the scattering angle θ, where:

$$g = \langle \cos(\theta) \rangle \tag{1.7}$$

A value of $g \approx 1$ indicates highly forward-scattered light, while $g \approx 0$ indicates equal forward and backward scattering; isotropic scattering is a special case of g = 0. Biological tissues typically have g values between 0.7 and 0.9, meaning light tends to scatter predominantly in the forward direction.

Mie theory is commonly used to model light scattering by larger tissue structures, such as mitochondria and collagen fibers. The Mie scattering intensity decreases approximately as λ^{-1} with increasing wavelength. This theory is suitable for structures with sizes on the order of the light wavelength (e.g., 1–10 μm in diameter). The scattering amplitude for a Mie scatterer depends on the relative refractive index and size of the scattering particle. For example, for a spherical particle of radius r and refractive index n, the Mie scattering cross-section σ is derived from Mie solutions to Maxwell's equations and varies with particle size and wavelength.

Rayleigh scattering, relevant for smaller structures (sub-wavelength scale, much smaller than the light wavelength), produces an intensity that decreases as λ^{-4}. This type of scattering occurs in tissues with nanoscale structures, such as small organelles or fine filaments. Rayleigh scattering is important for understanding the background scattering in tissue, as small-scale refractive index fluctuations contribute to the overall OCT signal.

In biological tissues, structures often exhibit a wide range of sizes, leading to both Mie and Rayleigh scattering contributions. Tissues can be modeled as a distribution of scatterers with varying sizes, each contributing to the overall scattering coefficient μ_s. The sum of Mie and Rayleigh scattering components can represent this combined scattering model. $\mu_{s,\text{Mie}}$ accounts for the scattering contribution of larger structures using Mie's theory. $\mu_{s,\text{Rayleigh}}$ accounts for scattering by

smaller structures using Rayleigh theory. This approach provides a more realistic representation of tissue scattering by capturing the contributions from large and small tissue structures.

1.2.2 Tissue Backscattering Modeling

Biological tissues are highly scattering media with structures that reflect and scatter light at varying angles. To effectively capture the scattering behavior of tissues, a phase function is employed to describe the angular distribution of scattered light. A commonly used model in OCT for this purpose is the Henyey-Greenstein phase function, which provides an efficient approximation for scattering in biological tissues, including skin, retina, and other highly scattering structures.

The Henyey-Greenstein phase function is defined by:

$$p(\cos\theta) = \frac{1 - g^2}{(1 + g^2 - 2g\cos\theta)^{3/2}} \tag{1.8}$$

where θ represents the scattering angle, and g is the anisotropy factor. The anisotropy factor g is a dimensionless parameter that characterizes the directionality of scattering. In most biological tissues, g is typically close to 1, as scattering events tend to be strongly forward-directed due to the refractive index variations of cellular structures and extracellular matrix components.

The backscatter factor is critical in OCT as it quantifies the fraction of light scattered back toward the detector, which is crucial for generating depth-resolved images. The Henyey-Greenstein phase function allows for modeling this backscattering behavior by considering the angular dependence of scattered light. In OCT, only the light that is backscattered within the acceptance angle of the detection system contributes to the image signal. Light backscattered within the detection system's acceptance angle will return to the detector and depend on the directional scattering probabilities of the tissue.

Modeling tissue scattering with the Henyey-Greenstein phase function enhances our ability to approximate how much light is scattered in the backward direction relative to the predominant forward direction. This backscatter component is essential in OCT because it directly impacts the achievable contrast and imaging depth. A higher proportion of backscattered light improves

image brightness and allows for better visualization of deeper structures. However, because biological tissues generally have high anisotropy values (i.e., $g \approx 0.8 - 0.9$), most light is scattered in the forward direction, meaning only a fraction of the initial light returns to the detector.

The Henyey-Greenstein phase function is widely used in OCT and other biomedical imaging modalities as it provides a simple yet effective model of tissue scattering. By adjusting the anisotropy factor g, the function can be tuned to match the scattering characteristics of different types of tissue. This flexibility makes the Henyey-Greenstein phase function a valuable tool for modeling scattering in both homogeneous and heterogeneous tissues. Furthermore, it enables quantitative analyses that can improve the interpretation of OCT images, particularly in applications requiring accurate tissue microstructure characterization, such as in ophthalmology and dermatology.

1.3 Significance and Motivation

Optical Coherence Tomography (OCT) has emerged as a non-invasive imaging modality. Initially developed for ophthalmology, OCT's high-resolution imaging capabilities have broadened its adoption in cardiology, dermatology, and oncology, where it is utilized for more disease diagnosis, monitoring progression, and evaluating subclinical changes. The non-invasive nature of OCT allows for repeated imaging without the risks associated with traditional invasive procedures.

OCT's three-dimensional imaging capabilities enable volumetric reconstructions of complex tissue structures. For example, 3D OCT is employed in dermatology to evaluate the depth and extent of skin lesions, providing critical insights that inform treatment decisions. In addition to structural imaging, OCT has evolved to include functional imaging capabilities, such as OCT angiography (OCTA), which visualizes blood flow without needing contrast agents. This advancement significantly broadens its application, particularly in assessing vascular health in the retina or other tissues.

Moreover, OCT's non-contact and noninvasive nature makes it ideal for longitudinal imaging, particularly for chronic disease management. This allows for effective long-term monitoring that

may improve patient outcomes. The ability to scan sensitive areas without direct contact minimizes patient discomfort and reduces the risk of infection, further enhancing OCT's utility in clinical settings.

OCT's strength in early detection is particularly beneficial for identifying minor changes at the onset of diseases, often before clinical symptoms appear. This capability is important for detecting conditions such as microvasculature damage in the heart after heart infarction, which will be presented in Chapter 3. OCT also enables the assessment of UV-induced skin damage, inflammation, and structural changes, which will be discussed in Chapter 5.

In conclusion, OCT has played a key role in non-invasive medical imaging through its unique value. It is widely applied across medical fields, particularly for early detection and ongoing disease management. As the technology of functional OCT advances, the potential for OCT to further enhance patient care remains significant.

1.3.1 Application of OCT in Coronary Microcirculation Imaging

Coronary microcirculation plays a crucial role in maintaining the function of the heart. Myocardial infarction (MI), a condition that occurs when a major coronary artery becomes blocked, would lead to tissue ischemia and necrosis. The phenomenon of "no-reflow," where blood flow is not adequately restored despite the successful reopening of larger coronary arteries, can lead to further myocardial injury and adverse outcomes. Notably, smaller capillaries within the microcirculation are the first to be damaged during ischemic events. Understanding the mechanisms and implications of coronary microvascular dysfunction is essential for improving patient prognosis after MI.

To understand and mitigate the risks associated with MI and reperfusion injury, direct imaging of the coronary microcirculation may be helpful but is challenging. The coronary microvasculature, with vessels typically smaller than 200 μm in diameter, is particularly challenging to observe in clinical settings due to its size and the limitations of conventional imaging techniques. Modalities like cardiac MRI and PET lack the spatial resolution required to visualize these small vessels

or capture their dynamic responses during ischemic and reperfusion events. This limitation often leaves clinicians reliant on indirect assessments of epicardial flow, overlooking crucial microvascular disruptions.

While foundational data exists on the anatomy of coronary microcirculation under normal conditions, the quantitative and detailed characterization of dynamic microvascular changes following MI remains limited. OCT offers a promising solution to these limitations. OCT angiography (OCTA) enables high-resolution, cross-sectional imaging of microvasculature interferometry using a motion-sensitive algorithm at a microscopic scale. While foundational data exist on the anatomy of coronary microcirculation under normal conditions, OCT holds unique potential for quantitatively characterizing microvascular changes. OCT's ability to generate three-dimensional images of the coronary microvasculature allows for precise mapping and analysis of its complex architecture, capturing data on capillary density, vessel diameter, and perfusion dynamics.

One of the primary benefits of using OCT to image heart surface microvasculature is its non-invasive nature, allowing for real-time imaging of microvascular changes during ischemia and reperfusion without introducing contrast agents that could potentially harm the tissue. This capability is particularly important in ex vivo models, such as the Langendorff-perfused heart, where maintaining tissue integrity is crucial for accurately assessing microvascular function and pathology. By providing high-resolution images of capillary diameter, morphology, and resistance, OCT enables researchers to investigate how these parameters affect circulatory functioning and oxygen extraction efficiency.

The Langendorff model serves as an effective ex vivo system to replicate the microfluidic behavior of the heart under conditions of ischemia and reperfusion. In this model, OCT can visualize the heterogeneity of blood flow properties, which is essential for understanding the mechanisms behind the "no-reflow" phenomenon. According to Poiseuille's law, flow rate is proportional to r^4, where r is the capillary radius. Similarly, resistance is proportional to $1/r^4$, meaning that any changes in capillary diameter or morphology can significantly impact overall blood flow and oxygen delivery to myocardial tissues. Using OCT, the changes can be quantified and correlated with

functional outcomes, providing insights into how microvascular dysfunction contributes to myocardial injury.

The significance of using OCT lies in its ability to provide high-resolution, quantitative insights into microvascular abnormalities and perfusion dynamics, which are not adequately captured by traditional imaging methods. OCT can directly visualize disruptions in myocardial perfusion at the capillary and microcirculatory level, offering a detailed assessment of structural and functional changes in vessels smaller than 200 μm in diameter.

By applying quantitative parameters, OCTA goes beyond the limitations of qualitative assessments, allowing for precise measurement of blood flow changes within the heart's microvascular system. This provides a more comprehensive understanding of how ischemia and reperfusion injuries affect microcirculation, enabling researchers to quantify the extent of blood flow disruptions. Such advancements are critical for translating this technique into in vivo heart studies, bridging the gap between preclinical research and clinical applications. Ultimately, this approach could lead to better monitoring of tissue engernering interventions and a deeper understanding of cardiovascular diseases at the microvascular level.

1.3.2 Application of OCT in Skin Angiography and micro-structural imaging

The need for in-depth, non-invasive imaging techniques has become increasingly evident in dermatology assessments. The skin's microstructure reveals details of layers such as the epidermis and dermis, allowing for the detection of abnormalities, including lesions, scars, and signs of aging. Examining the skin capillaries—the network of small blood vessels within the skin—yields insights into blood flow dynamics and helps detect vascular changes associated with inflammation and wound healing. These structural and vascular insights support more sub-clinical assessments, improving diagnostics, treatment planning, and skin health monitoring.

Traditional diagnostic methods, like biopsies and blood tests, provide valuable information but are invasive and limited to isolated time points. Confocal microscopy offers high-resolution, 3D

imaging but often requires biopsy and has limited repeatability. Vivascope^{T} $Masanexampleof3D-confocalmicroscopythatisdoneinvivo(depthresolution = 200\mu m)$, but with very good lateral resolution. Similarly, dermoscopy allows detailed two-dimensional surface imaging but lacks the depth needed for comprehensive analysis. High-resolution ultrasound can penetrate deeper into tissues than dermoscopy but often lacks the precision required for microstructural and microvascular assessment. Despite advancements, there remains a need for imaging that combines high resolution with adequate depth penetration for detailed functional analysis of skin tissue.

OCT has emerged as a promising solution to these limitations. As a high-resolution, cross-sectional imaging method, OCT allows visualization of the internal microstructure of the skin and has been effectively applied to study conditions like actinic keratosis, wound healing, and basal cell carcinoma. Its ability to visualize the layered structure of the skin supports more precise and non-invasive assessment of abnormalities. Initially developed for ophthalmology, OCT has been adapted for skin imaging by addressing the challenges of highly scattered skin tissue. Achieving adequate penetration depth has been essential for OCT in dermatology. Standard OCT can visualize up to 1.5 mm beneath the skin surface, covering the epidermis and upper dermis.

A significant gap in dermatology lies in the ability to quantitatively assess tissue properties such as attenuation, anisotropy, and reflectivity, which are critical for understanding skin structure and composition. Optical Coherence Tomography (OCT) addresses this gap by providing high-resolution, non-invasive imaging to identify microstructural and compositional changes. OCT's sensitivity to attenuation and reflectivity reveals abnormalities in cellular architecture and tissue integrity, while its ability to measure anisotropy highlights directional organization, such as collagen alignment, crucial for evaluating conditions like fibrosis, skin aging, and wound healing. By quantifying these properties, OCT offers a powerful tool to detect early pathology, monitor disease progression, and assess treatment response, significantly advancing the understanding and management of skin health.

Although cutaneous blood flow accounts for approximately 4% of the body's total blood volume, it is critical for maintaining skin health and supporting physiological processes such as ther-

moregulation and immune defense. Capillaries within the skin play a pivotal role in this circulation, but subtle changes in their structure and perfusion often occur before clinical symptoms become apparent, signaling the early stages of conditions like inflammation, wound healing disruptions, or vascular disorders.

Despite its potential, the application of Optical Coherence Tomography (OCT) in dermatology faces notable gaps that limit its broader adoption and impact. Unlike ophthalmology, where OCT is highly standardized and calibrated, dermatological OCT lacks established protocols and functional extensions to reliably interpret key metrics such as tissue attenuation and blood flow speed. This lack of standardization and functional imaging capabilities results in inconsistencies in diagnosis and limits its clinical utility. Additionally, qualitative and quantitative biomarkers are limited for pathology detection, such as identifying changes in blood vessels or delineating tissue abnormalities like cancer boundaries. This gap underscores the need for enhanced methods to extract and interpret meaningful information from OCT images for accurate pathology assessment.

In summary, while OCT has evolved from its origins in ophthalmology into a valuable imaging modality for dermatology, it is critical to address these challenges through standardization, functional imaging developments, and biomarker integration. These advancements would enable consistent diagnosis, improved tissue and vascular change interpretation, and more effective detection of skin pathologies, significantly advancing dermatological care.

1.4 Summary of OCT Application and Limitation

Optical Coherence Tomography (OCT) has established itself as a micrometer-scale-resolution noninvasive imaging modality with broad applications across various medical fields. Its high-resolution, three-dimensional imaging ability has made it invaluable for detecting subclinical changes and assessing disease across multiple fields. This thesis is motivated to research OCT's unique strengths and the gaps in current imaging methodologies, particularly in heart and skin imaging applications.

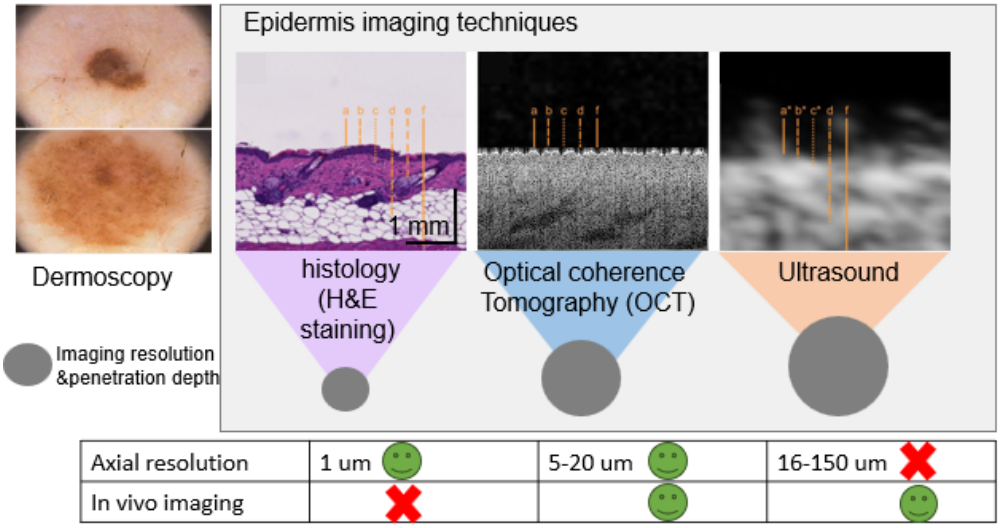

Figure 1.2: 1 Comparison of epidermis imaging techniques based on resolution, penetration depth, and capability for in vivo imaging. The figure displays four methods: dermoscopy, histology (H&E staining), OCT, and ultrasound. Figure adapted from [3, 157].

In cardiovascular applications (Chapter 3), OCT is uniquely positioned to overcome the limitations of conventional imaging techniques like MRI and PET, which lack the resolution to capture microvascular dynamics. The study demonstrated the critical role of OCT in imaging coronary microcirculation, especially in the context of ischemia and reperfusion injuries. The Langendorff model assists OCT's capability to map microvascular changes and quantify capillary morphology, flow dynamics, and perfusion. This research addresses the pressing need for non-invasive methods to evaluate and manage coronary microvascular dysfunction.

In dermatology applications (Chapters 4 and 5), OCT's ability to visualize skin microstructure and vasculature non-invasively offers significant advantages over traditional diagnostic methods such as biopsies and dermoscopy. The study explores OCT's potential to detect subtle structural and vascular changes in skin tissue, particularly in the context of wound healing, UV exposure, and aging assessment. The quantitative analysis of tissue properties like attenuation, anisotropy, and reflectivity further broadened OCT's ability to reveal microstructural properties of the different layers of skin (epidermis, papillary dermis and reticular dermis).

Despite its expanding applications, several limitations prevent the broader adoption of OCT across diverse fields. One major challenge is the limited information provided by conventional structural OCT scans, which primarily offer micro-level 3D scans of tissue morphology but do not provide extra insights into the physiological or functional aspects of the condition of the skin and heart. This limitation restricts its utility in applications, for example, understanding tissue dynamics such as capillary blood flow, tissue characteristics, or collagen conditions.

This study aims to address these gaps by leveraging OCT's capabilities in imaging coronary microcirculation and skin angiography while driving the development of functional OCT techniques. Approaches such as OCT velocimetry for blood flow measurement, OCT angiography for microvascular visualization, OAC for tissue attenuation and anisotropy, and polarization-sensitive OCT for tissue composition analysis could provide complementary information and expand the diagnostic scope of OCT. By introducing these functional capabilities, OCT could deliver more comprehensive diagnostic information, facilitate early disease detection, and enable effective monitoring of disease progression before any clinical significance. Ultimately, this work seeks to refine OCT's utility for broader research applications, advancing our understanding of tissue microstructure and vascular dynamics.

In summary, while OCT has established itself as a valuable tool for noninvasive imaging, further advancements in functional OCT could broaden its application across diverse clinical and research fields.

2 FUNCTIONAL EXTENSIONS OF OCT

Functional OCT enhances its diagnostic power by providing structural imaging and valuable insights into tissue physiology and microvascular health, broadening its applications in clinical and research settings.

Optical Coherence Tomography (OCT) offers a range of techniques for both qualitative and quantitative imaging, enabling a comprehensive assessment of (1) microvascular information and (2) tissue composition. As introduced in Chapter 1, OCT combines high-resolution imaging with non-invasive capabilities, making it a versatile tool for diverse clinical and research applications. Building on the foundational principles outlined in Chapter 1, this chapter delves into the application of advanced OCT techniques.

OCT Angiography (OCTA), is a powerful modality for visualizing microvascular networks and assessing blood flow without requiring contrast agents. Methods like Optical Microangiography (OMAG) and OCT velocimetry, which were briefly introduced earlier, are employed in this chapter to provide detailed insights into capillary morphology and blood flow velocity. These capabilities allow for precise analysis of hemodynamic properties and microvascular health, which are critical for understanding disease progression through the microvasculature damages.

In addition to OCTA, OCT Structural Imaging Techniques support quantitative assessments such as measuring epidermal thickness and optical attenuation coefficients. These methods enable the identification of tissue compositions based on scattering properties and provide complementary information to enhance the interpretation of OCT signals.

Together, the techniques described in this chapter will be extensively utilized throughout this chapter to address specific research questions and challenges. By integrating these advanced OCT

methods, this chapter aims to extend the broader applicability of OCT discussed in Chapters 3-6 into focused studies on assessing tissue structure and microvascular health.

2.1 Optical Coherence Tomography Angiography

Optical Coherence Tomography Angiography (OCTA) is an advanced imaging technique that utilizes the movement of red blood cells (RBCs) within blood vessels to create high-contrast maps of blood flow without the need for invasive dye injections. OCTA's fundamental principle relies on tracking changes in the OCT signal at the same location over time (M-scan) to differentiate moving particles, like RBCs, from static tissue structures. This time-dependent fluctuation in backscattered signals allows for the clear visualization of vascular networks, aiding research and clinical applications across a variety of biological tissues.

OCTA technology leverages the complex nature of OCT signals, which contain both amplitude and phase information, enabling a range of algorithms to analyze blood flow dynamics. These algorithms can be categorized based on which component they emphasize: phase-signal-based, intensity-signal-based, or complex-signal-based OCTA.

Optical Microangiography (OMAG), initially proposed by Wang et al. in 2007 and refined in subsequent years, utilizes both amplitude and phase information to enhance sensitivity in detecting blood flow. This algorithm calculates blood flow by averaging differences in complex signals across repeated B-scans at the same location. The OMAG algorithm computes the flow signal by subtracting consecutive complex OCT signals at the same spatial location. The complex OCT signal $C(x, z, t)$ at a given location (x, z) and time t can be represented as:

$$C(x, z, t) = I(x, z, t)e^{i\Phi(x,z,t)} \tag{2.1}$$

where $I(x, z, t)$ is the amplitude component and $\Phi(x, z, t)$ is the phase component. The OMAG flow signal, $\text{Flow}_{\text{OMAG}}(x, z)$, is calculated by averaging the absolute differences between consecutive complex signals across N repeated B-scans:

$$\text{Flow}_{\text{OMAG}}(x, z) = \frac{1}{N-1} \sum_{i=0}^{N-1} |C_{i+1}(x, z) - C_i(x, z)| \tag{2.2}$$

where $C_i(x, z)$ is the complex signal at the i-th B-scan.

OMAG is a highly sensitive OCTA technique that detects microcirculation in human tissues, including the mouse brain, human skin, and retina. Its ability to visualize fine vascular structures, such as retinal capillaries, choriocapillaries, and radial retinal capillaries, has proven valuable in distinguishing diseased eyes from normal ones and detecting disease development and progression.

OCTA's clutter rejection capabilities further enhance its reliability in detecting flow. Advanced filtering techniques address clutter from static tissues and motion artifacts, which is more suitable for small vessels. Overall, OCTA represents a powerful and non-invasive approach for imaging vascular structures, with versatile algorithms like OMAG driving its applicability in visualizing dynamic microcirculatory systems in the body.

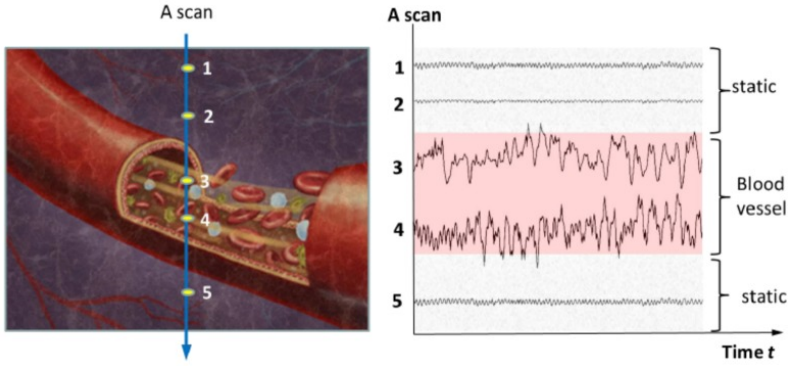

Figure 2.1: Illustration of an OCT A-scan along a blood vessel showing static and dynamic regions. Positions 1 and 2 represent static tissue above the vessel, while positions 3 and 4 indicate blood flow within the vessel. Position 5 represents static tissue below the vessel. The plot on the right shows the OCT signal over time for each position, with the central region corresponding to blood flow marked in red, displaying higher fluctuations than the static regions.[52]

2.1.1 Eigendecomposition-based Optical Microangiography (ED-OMAG)

The interference signal of one OCT scan can be expressed as:

$$I(t,k) = S(t,k)\cdot E_R^2 + 2S(t,k)\cdot E_R \int a(z,t)\cos(2kn(t)z)\,dz + 2S(t,k)\cdot E_R a(z_l)\cos[2kn(t)(z_l - vt)] \tag{2.3}$$

where $I(t,k)$ is the detected light intensity at time t and wavenumber k, E_R is the light reflected from the reference mirror, $S(k)$ is the spectral density of the light source at k, n is the refractive index of the tissue, z is the depth coordinate, $a(z)$ is the amplitude of the backscattered light, z_l is the depth from which the light is backscattered, and v is the velocity of moving particles, such as blood cells, at depth z_l.or can be written as the simplified version:

$$I(k) = I_{\mathrm{DC}} + I_{\mathrm{AC}}\cos(2knz) \tag{2.4}$$

In this simplified expression, the DC term I_{DC} corresponds to the signal from static tissue structures, and the oscillating term $I_{\mathrm{AC}}\cos(2knz)$ represents the interference from the backscattered light. The AC term encodes depth information and is sensitive to moving particles, like red blood cells.

To analyze blood flow and distinguish it from clutter (static tissue signals), we look at the complex OCT signal X formed by repeated A-line acquisitions at a specific depth. Each sample X contains information about the amplitude and phase, which are sensitive to motion (e.g., blood flow). Since X is Gaussian, it is characterized by its correlation matrix R_x of X characterizes these signals and is defined as:

$$R_x = E[XX^H] \tag{2.5}$$

Where E is the expectation, and X^H is the Hermitian transposed X. In practice, the expectation E is approximated by averaging across multiple depth locations or repeated measurements.

Assuming that clutter is the dominant signal and that its characteristics are similar along the depth, we can estimate the clutter correlation matrix $\hat{R}_c$ by spatially averaging the correlation of the received signals along the axial direction:

$$\hat{R}_c = \frac{1}{M} \sum_{i=1}^{M} X_i X_i^H \tag{2.6}$$

Where X_i the complex OCT signal from the i-th depth location M is, the number of depth locations used for averaging is $()^H$ denoted by the Hermitian transpose. This spatial averaging helps estimate the clutter component by capturing stable signal characteristics across the depth, effectively filtering out the dynamic blood flow component.

The resulting correlation matrix $\hat{R}_c$ represents the clutter, which can then be decomposed through eigendecomposition to further isolate and remove these static components from the signal. The estimated correlation matrix $\hat{R}_c$ is then decomposed into its eigenvalues and eigenvectors:

$$\hat{R}_c = E \Lambda E^H \tag{2.7}$$

where $E = [e_1, e_2, \ldots, e_N]$ is the $N \times N$ unitary matrix of eigenvectors, and $\Lambda = \text{diag}\{\lambda_1, \lambda_2, \ldots, \lambda_N\}$ is the diagonal matrix of eigenvalues with $\lambda_1 \geq \lambda_2 \geq \cdots \geq \lambda_N = \sigma_n^2$.

To retrieve flow information, multiple A-lines are acquired from the same location. The observation X can be modeled as the sum of three independent zero-mean complex Gaussian processes: a clutter component c, a blood component b, and additive white noise n:

$$X = c + b + n \tag{2.8}$$

Since X is Gaussian, it is characterized by its correlation matrix R_x:

$$R_x = R_c + R_b + \sigma_n^2 I \tag{2.9}$$

where R_c is the clutter correlation matrix, R_b is the blood correlation matrix, σ_n^2 is the noise variance, and I is the identity matrix. Assuming that the clutter space is spanned by the first K eigenvectors, an eigenregression filter is applied to the received signal to remove the clutter components:

$$\text{Flow}_{\text{OMAG}} = \left(I - \sum_{i=1}^{K} e_i e_i^H \right) X \tag{2.10}$$

$Flow_{\text{OMAG}}$ is the signal obtained after removing the clutter through eigendecomposition-based filtering, which now predominantly contains flow information from moving particles, such as red blood cells, while minimizing interference from stationary tissue structures. The term $\sum_{i=1}^{K} e_i e_i^H$ represents the projection matrix onto the subspace spanned by the first or second K eigenvectors associated with the clutter, depending on the number of repeats collected and the quality of the data.

2.2 Optical Coherence Tomography Velocimetry

2.2.1 Combining ED-based Statistics with the Autocorrelation Function

The fluctuation of flow frequency in the OCT complex signal is influenced by flow vectors, such as flow direction and speed. The power spectrum of the OCT complex signal detected from vessel flow can be obtained by applying the Fourier transform to the autocorrelation function. According to Wiener-Khinchine's theorem, the relationship between the autocorrelation function $R(\tau)$ and the power spectrum $P(\omega)$ is given by:

$$P(\omega) = \int_{-\infty}^{\infty} R_x(\tau) e^{-i\omega\tau} \, d\tau \tag{2.11}$$

where τ represents the correlation time in the autocorrelation function. The maximum and minimum range for velocity measurement depends on the integration of the scan time and the interval

between each B-frame scan. The mean angular frequency of the frequency spectrum can be estimated from the autocorrelation values at $\tau = 0$ and $\tau = T$ as follows:

$$\bar{\omega} = \dot{\phi}(0) = \frac{\phi(T)}{T} \tag{2.12}$$

Since the eigendecomposition of flow fluctuation is analogous to the Fourier transform, each eigen component carries a specific mean frequency. The lag-one autocorrelation value for each eigenvector can be used to estimate the center frequency for the k-th eigenvector. The estimated central frequency $\hat{f}_c$ is calculated as:

$$\hat{f}_c = \frac{1}{2\pi}\phi(T) = \frac{1}{2\pi}\arg(R_y(1)) \tag{2.13}$$

where $\hat{f}_c$ is the central frequency associated with each eigen component k, and $R_y(1)$ is the lag-one autocorrelation value for the k-th eigenvector. For N_D eigenvectors, $R_y(1)$ is defined as:

$$R_y(1) = \frac{1}{N_D - 1}\sum_{m=0}^{N_D-2} e_k^*(m)e_k(m+1) \tag{2.14}$$

Thus, the central Doppler frequency $\bar{\omega}$ can be obtained by taking the weighted average of each frequency with its corresponding spectral band information:

$$\bar{\omega} = \frac{1}{P}\int_{-\pi}^{\pi} \omega G(\omega)\, d\omega \tag{2.15}$$

where $G(\omega)$ is the spectral band information of each eigenvector, which is also represented by its eigenvalue.

2.2.2 Phantom Studies

2.2 illustrates the spectral band information and the estimated mean frequency for each eigen-decomposed component relative to the selected signal. For static tissue, the first principal component typically shows high spectral band energy but has a low central frequency estimation (2.2)d.

Subsequent components from static signals may reflect noise artifacts, leading to non-zero central frequency estimations but with minimal spectral band energy. For low signals, the central Doppler frequency estimated for the first to third components aligns closely with the actual mean flow frequency, with most of the eigen spectral energy concentrated along these eigenvectors, corresponding to Doppler shifts indicative of motion (2.2). In contrast, the spectral band energy for noise signals tends to spread across other eigenvalues, resulting in a randomly distributed eigen spectral power across components (2.2). This random phase shift due to time variation can cause noise signals to resemble flow signals due to the rate of phase change.

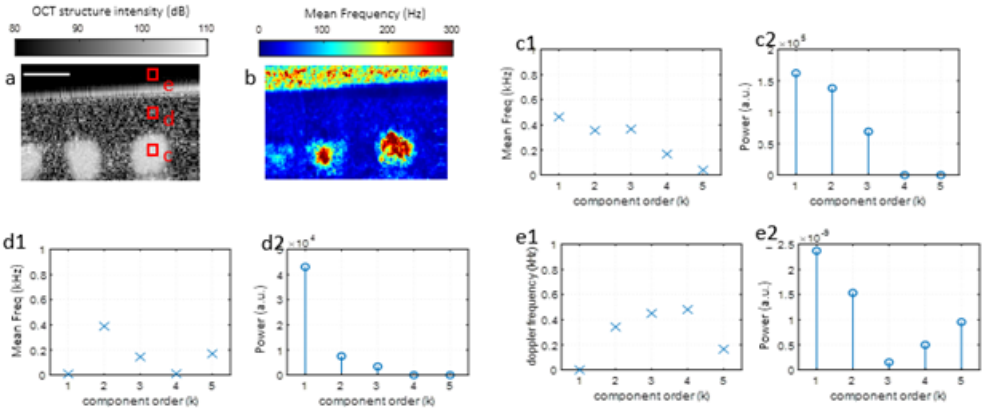

Figure 2.2: "Analysis of central doppler frequency and power distribution across different signal types in OCT imaging. (a) OCT structural intensity image, (b) mean frequency map. The highlighted red boxes in (a) and (b) indicate regions of interest for different signal types. The measured central Doppler frequency (left) and corresponding power (right) of voxels related to different types of signals: (c) flow signal, (d) static structure, and (e) noise.

In this study, we evaluated the capability of OMAG velocimetry with Doppler in detecting flow characteristics within a microfluidic phantom perfused with a 1% Intralipid solution. The microfluidic phantom consisted of three distinct channels, representing various flow conditions that mimic microvascular structures.

Figure 2.3 provides a detailed comparison of structural OCT, OCTA flow signal, Doppler velocity, and OMAG velocimetry images. Panel (a) shows the structural OCT image, which highlights the physical layout of the microfluidic channels, with clear boundaries of each channel.

Panel (b) displays the OCTA flow signal, which indicates the presence and distribution of flow within the channels, providing an overview of flow-related intensity across the microfluidic structure.

In panel (c), the Doppler velocity signal reveals the absolute velocity within the channels, offering quantitative information about flow speed. However, phase-wrapping artifacts are evident, especially in regions with high flow velocity, which complicates precise velocity measurements. Panel (d) shows the OMAG velocimetry signal, which enhances flow detection by compensating for phase-wrapping issues observed in Doppler imaging, allowing for clearer differentiation between low and high flow areas.

The normalized signal profiles of OMAG flow intensity, velocimetry, and Doppler velocity are presented in panel (e). The profiles demonstrate a consistent pattern across the three channels, with the velocimetry signal showing a smoother and more continuous profile compared to Doppler velocity, which exhibits fluctuations due to phase-wrapping artifacts (highlighted by yellow arrows). These artifacts are likely caused by the limitations of Doppler imaging in handling high-flow velocities, which velocimetry mitigates through enhanced signal processing.

Overall, the results indicate that OMAG velocimetry provides a reliable and artifact-free representation of flow in microfluidic channels, effectively differentiating between various flow velocities across the channels. The findings support the utility of OMAG velocimetry in applications requiring precise flow visualization, particularly in complex microvascular environments.

The ability of OMAG velocimetry to quantify flow velocity was evaluated using a plastic tube phantom perfused with 1% Intralipid solution and whole blood. The cross-sectional OMAG image in Figure 2.4(a) shows the structure of the plastic tube, with concentric circles indicating the center for radial averaging measurements.

Figures 2.4(b) and 2.4(c) present the velocity cross-sectional images of the tube perfused with 1% Intralipid at two different flow rates, 0 μm/s and 200 μm/s, respectively. The color-coded images illustrate a clear difference in velocity distributions across the tube, with higher flow rates

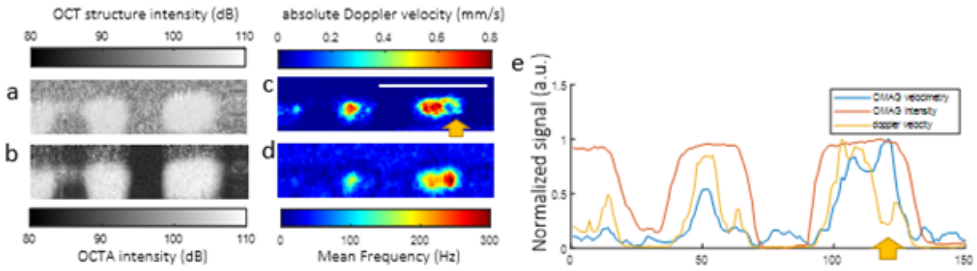

Figure 2.3: Representation of the OCT, OCTA, velocimetry, and Doppler images of microfluidic channels perfused with a 1% Intralipid solution. The cross-sectional images show (a) structural OCT, (b) OCTA flow signal, (c) Doppler velocity signal, and (d) OMAG velocimetry signal of the microfluidic flow phantom in the same cross-section. The three tube channels from right to left represent the microfluidic channels' first, second, and third inner branches. (e) Normalized signal profile for OMAG flow intensity, OMAG velocimetry, and Doppler velocity, respectively. The yellow arrows indicate suspected phase-wrapping artifacts from Doppler imaging.

resulting in a broader range of detected velocities. The OMAG velocimetry signal effectively captures the spatial distribution of flow within the phantom.

Figure 2.4(d) shows the normalized profile of OMAG vs. velocimetry signals along the central depth of the tube. The observed data points were fitted using a parabolic (least square) fit, indicated by the solid line. This parabolic profile demonstrates the characteristic flow velocity distribution across the tube's cross-section, with higher velocities near the center and lower velocities near the edges, consistent with laminar flow behavior in a confined channel.

Finally, Figure 2.4(e) provides quantitative analysis by plotting the mean radial frequency against the perfusion velocity for Intralipid and whole blood. The linear trend observed in both cases indicates a strong correlation between mean frequency and flow velocity, demonstrating the effectiveness of OMAG velocimetry in quantifying flow rates. The comparison between Intralipid and whole blood also highlights the consistency of OMAG measurements across different perfusates, with slightly higher frequencies observed for whole blood at comparable flow rates.

2.2.3 In vivo Studies: Skin Blood Flow Recovery

Additionally, a skin temperature recovery experiment tested the feasibility of OMAG velocimetry. Capillary flow plays a crucial role in maintaining tissue metabolism. The suppression of lo-

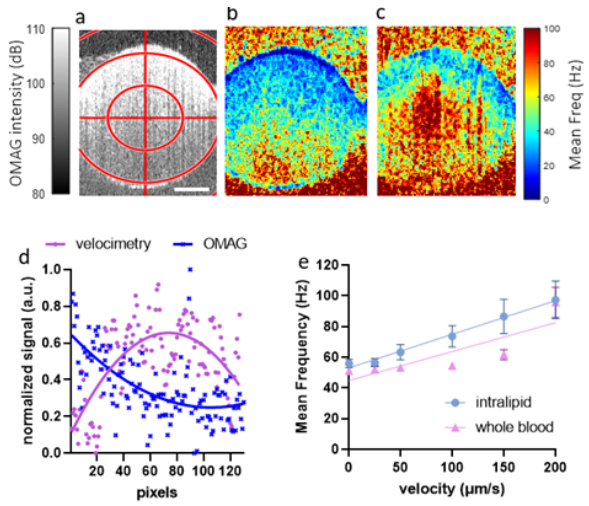

Figure 2.4: (a) OMAG cross-sectional image of a plastic tube perfused with 1% Intralipid, with a concentric circle indicating the center for radial averaging measurements. The scale bar represents 25 μm. (b) Velocity cross-sectional image of the plastic tube perfused with 1% Intralipid at 0 μm/s and (c) at 200 μm/s. (d) Normalized profile of the OMAG and velocimetry signals along the depth passing through the center of the plastic tube, with results fitted by a parabolic (least square) fit, shown as a solid line. (e) Quantification of the mean radial frequency when the plastic tube is perfused with Intralipid and whole blood at different perfusion rates, showing a linear relationship between mean frequency and perfusion velocity.

cal forearm temperature was observed in human tissue following cold stimulation applied with imaging gel (Figure 2.5(a)). A local temperature recovery response was also observed over time (Figure 2.5(b)).

The OCTA projection images before and during recovery are shown in Figure **??**. Quantitative analysis was conducted to assess vessel area density (VAD) throughout the recovery process. From the OMAG maximum intensity projection, an increase in observable vessels correlating with skin temperature recovery is evident, with the VAD showing an 85% increase from the cooled condition (16% ± 9%) to baseline (27% ± 8%). A consistent trend of increasing cutaneous flow response was observed across all volunteers (Figures 2.5(i) and 2.5(j)).

A map of the mean frequency (MF) of cutaneous flow on forearm skin was demonstrated for the condition after cold gel stimulation and following a two-minute recovery. From the maximum projection of the MF 3D volume, the capillary's mean frequency before and after a four-minute

recovery was visualized. MF quantification revealed a significant 52% increase in cutaneous blood flow velocity between the cold gel-stimulated condition (18 ± 8 Hz) and recovery (25 ± 6 Hz). Additionally, more vessels with lower MF values appeared in the recovered state, and a clear shift in flow velocity distribution toward faster flow was observed (Figure 2.5(k)).

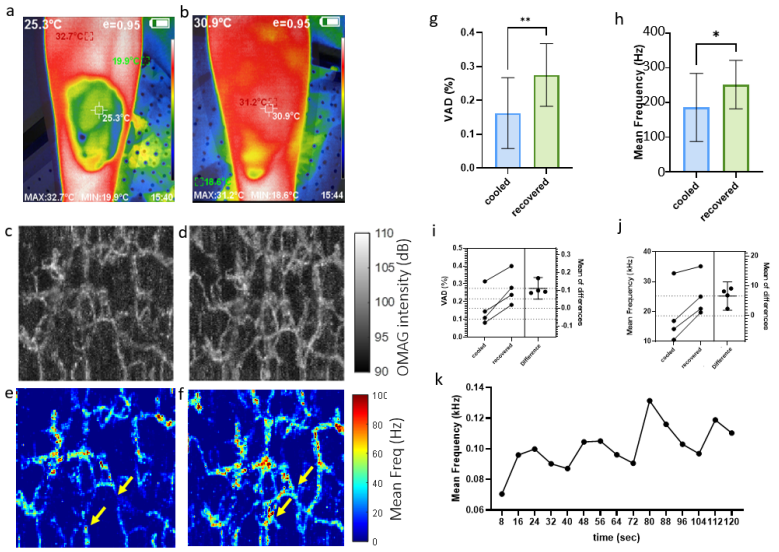

Figure 2.5: Demonstration of changes in forearm skin tissue after the application of imaging gel, visualized through vasculature maps and quantified metrics. Panels (a) and (b) show representative thermal images of the forearm color-coded by temperature, with (a) captured after application of cold gel and (b) after a 4-minute recovery. OCTA projection images and OMAG velocimetry projections of cutaneous blood flow are displayed in (c) and (e) following cold stimulation, and in (d) and (f) after a 2-minute recovery, respectively. Panels (g) and (h) present mean and standard deviation values for vessel area density (VAD) and mean frequency in the cooled and recovered conditions, with statistical significance indicated by * ($p < 0.05$) and ** ($p < 0.01$). Panels (i) and (j) show paired t-test plots illustrating individual differences in VAD and mean frequency across cooling and recovery states for each participant. Panel (k) depicts the mean frequency trend over time during the recovery period, highlighting dynamic changes in cutaneous blood flow.

2.3 OCT Optical Attenuation Coefficient

The optical attenuation coefficient (OAC) is commonly used in various dermatologic applications, such as skin layer segmentation, assessing wound healing, and differentiating pathological tissue [12, 50]. The attenuation of light in tissue can be described by the following equations:

$$I(z) = I_0 e^{-2\mu z} \tag{2.16}$$

where $I(z)$ is the OCT signal intensity as a function of depth z, I_0 is the initial intensity at the surface, and μ is the attenuation coefficient. Taking the natural logarithm of both sides, we obtain:

$$\ln(I(z)) = \ln(I_0) - \mu z \tag{2.17}$$

Letting $\rho = \ln(I_0)$, we can express the equation in a linear form:

$$\ln(I(z)) = \rho - \mu z \tag{2.18}$$

where ρ represents the logarithmic initial intensity, and the attenuation coefficient μ can be calculated as the derivative of $I(z)$ with respect to z:

$$\mu = -\frac{d\ln(I(z))}{dz} \tag{2.19}$$

The primary challenge in calculating optical attenuation in Optical Coherence Tomography (OCT) for dermatology, particularly in skin imaging, lies in accurately estimating the optical attenuation coefficient (OAC) from OCT data.

2.3.1 Correcting for Focus Function and System Roll-Off

While several studies have focused on estimating the attenuation coefficient using different models [12], the calculation of the attenuation coefficient in skin imaging, often neglects the influence of

the focus function and system roll-off. This distortion can lead to either an overestimation or underestimation of the attenuation coefficient, depending on the depth and characteristics of the sample 2.6.

In an ideal scenario, the OCT signal would decay exponentially with depth due to the tissue's attenuation coefficient. However, the focus function introduces additional loss, causing the signal to decay more rapidly than the expected tissue attenuation. The focus function follows a Gaussian-like profile due to light distribution at focusing optics. As light travels beyond the focal plane, it diverges and reduces the system's ability to collect backscattered photons. Focus function would cause a substantial drop in signal strength after the focus region, resulting in a rapid fall off of the OCT signal beyond this point.

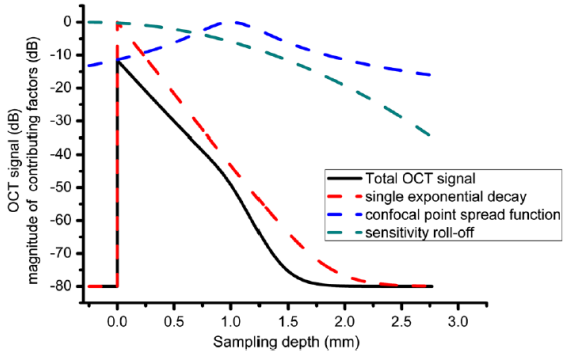

Figure 2.6: The relationship between the focus function and diffusion theory, showing deviations at depths where optical properties differ from theoretical assumptions. Figure adapted from [73]

To account for the focus function in OCT measurements, we define $F(z)$ it as the confocal point spread function, which describes the intensity distribution of a Gaussian beam as it propagates through tissue. The CPSF can be expressed as:

$$F(z - z_f) = \frac{1}{\sqrt{\left(\frac{z - z_f}{2nz_R}\right)^2 + 1}} \tag{2.20}$$

where z is the geometrical distance from the tissue boundary, z_f is the depth location of the focus relative to the tissue boundary, z_R is the Rayleigh length of the Gaussian beam incident on

the sample, and n is the average refractive index of the medium along the beam path. This expression captures the beam divergence correction factor, ensuring that the attenuation coefficient measurements are adjusted according to the focal properties of the OCT system. The factor 2 in the denominator, $2nz_R$, accounts for the increased Rayleigh length z_R for a diffuse reflector compared to a specular reflector.

As the beam penetrates deeper into the tissue, the signal intensity decreases due to the beam divergence, which can lead to inaccuracies in the measured attenuation coefficient if not corrected. The sensitivity roll-off, which describes how the system's sensitivity decreases with depth, is also an important factor to consider. This roll-off function, denoted as $h(z - z_0)$, is given by:

$$h(z - z_0) = \mathrm{sinc}\left(\frac{\pi(z - z_0)}{2z_D}\right) \tag{2.21}$$

where z_0 is the zero-delay position of the interferometer, $z_D = \frac{\lambda^2}{4n\Delta\lambda}$ is the maximum imaging depth, λ is the center wavelength, n is the average group refractive index, s is the ratio of spectral resolution to sampling pitch, and $\Delta\lambda$ is the spectral width. This roll-off model combines both the finite sampling density of interference fringes and the finite spectral resolution, which together affect the OCT signal as depth increases.

Incorporating the CPSF and sensitivity roll-off corrections allows for more accurate OCT measurements by compensating for depth-related distortions in signal intensity. This correction is essential for reliably estimating the attenuation coefficient across different tissue depths.

However, accurately mapping and correcting the focus function presents several challenges. One major challenge is the depth dependency of $F(z)$; as the focal plane shifts deeper into the tissue, the signal intensity decreases, introducing complexities in estimating $F(z)$ accurately across various depths. This depth dependency means that a single $F(z)$ model may not be universally applicable and may require adjustments depending on the tissue's depth and optical properties. Another challenge is the variability in sample properties, such as scattering and absorption, which affect the beam profile differently across different types of tissues. This variability complicates the development of a universal focus correction model that can be applied to diverse tissue types.

2.3.2 Focus Function Correction Using Standard Correction

Using standards, such as polystyrene spheres with accurately known optical properties, can correct the OCT signal using Beer's law:

$$\ln\left(\frac{i^2(z)}{i_0^2(z)}\right) = -2(\mu_t - \mu_{t0})z + a \tag{2.22}$$

where $i^2(z)$ is the OCT signal intensity as a function of depth z for the sample, $i_0^2(z)$ is the OCT signal intensity as a function of depth z for the calibration suspension, a is a constant for each A-scan dependent on the ratio of the OCT measurement between the sample and calibration suspension, and μ_t and μ_{t0} are the attenuation coefficients of the sample and the calibration suspension, respectively. This calibration process involves adjusting the OCT signal based on the known optical properties of the samples, allowing for a more accurate estimation of the attenuation coefficient. Using a calibration measurement in OCT measurements can ensure that the attenuation coefficient is reliable and comparable between studies. Chapter 5 will include more discussions.

3 OCTA Assessment of Microvascular Remodeling and Perfusion Impairment in Myocardial Infarcted Hearts

Optical Coherence Tomography Angiography (OCTA) enables high-resolution, non-invasive imaging of cardiac microcirculation without dyes or genetic labeling, offering a novel approach to understanding microvascular responses for ischemic heart disease.

Capillary on the heart is responsible for 75% of myocardial blood flow. Measuring heart microcirculation is critical despite the many challenges involved because it plays a vital role in understanding and addressing myocardial infarction (MI) and post-MI recovery. Microcirculatory dysfunction remains a significant barrier to full recovery. Even with successful revascularization of the larger coronary arteries, inadequate perfusion at the microvascular level can lead to persistent ischemic damage, heart failure, and, ultimately, increased morbidity and mortality. This "no-reflow" phenomenon and subsequent microvascular impairment underscore the necessity of measuring and understanding microcirculation to improve patient outcomes and develop new therapeutic strategies for limiting ischemic-reperfusion (IR) injury.

The journey to effectively image the heart's microcirculation has evolved through several pioneering phases, each marked by technological advancements and an increasing understanding

of the heart's microvascular dynamics. Initial studies in the late 1960s and 1970s focused on the anatomical and physiological aspects of coronary microvasculature, with researchers employing crude and labor-intensive techniques to capture static images of the beating heart. These early efforts were limited by the heart's deep anatomical location, high motion, and low transparency, making real-time imaging challenging [91].

In recent years, high-resolution imaging tools like laser scanning confocal microscopy, spinning disk confocal microscopy, and multiphoton microscopy have enabled real-time observatiocoronary microcirculation observation in diseased states. These techniques allow for precise visualization of red blood cell velocities, immune cell infiltration, and microvascular perturbations in response to ischemia and reperfusion. Despite these advancements, current imaging tools still face limitations, such as the inability to directly visualize capillaries smaller than 200 μm and accurately quantify microvascular flow in clinical settings.

The importance of measuring heart microcirculation builds directly on the foundational concepts of Optical Coherence Tomography (OCT) and its applications discussed in previous chapters. Earlier, this thesis explored how OCT and its advanced modalities, such as OCT Angiography (OCTA), offer high-resolution imaging and quantitative assessments of microvascular networks. This chapter addresses the critical role of heart microcirculation in understanding and managing MI and its consequences. As previously discussed, OCTA's capability to visualize capillary networks and measure blood flow velocity provides an essential tool for examining microvascular health. This chapter expands the understanding the "no-reflow" phenomenon and ischemia-reperfusion injury with OCTA as a novel imaging modality.

3.1 Quantifying Microvascular Structure in Healthy and Infarcted Rat Hearts Using Optical Coherence Tomography Angiography

Myocardial infarction (MI) is a life-threatening medical emergency resulting in coronary microvascular dysregulation and heart muscle damage. One of the primary characteristics of MI is capillary loss, which plays a significant role in the progression of this cardiovascular condition. In this study, we utilized optical coherence tomography angiography (OCTA) to image coronary microcirculation in fixed rat hearts, aiming to analyze coronary microvascular impairment post-infarction. Various angiographic metrics are presented to quantify vascular features, including the vessel area density, vessel complexity index, vessel tortuosity index, and flow impairment. Pathological differences identified from OCTA analysis are corroborated with histological analysis. The quantitative assessments reveal a significant decrease in microvascular density in the capillary-sized vessels and an enlargement for the arteriole/venule-sized vessels. Further, microvascular tortuosity and complexity exhibit an increase after myocardial infarction. The results underscore the feasibility of using OCTA to offer qualitative microvascular details and quantitative metrics, providing insights into coronary vascular network remodeling during disease progression and response to therapy.

3.1.1 Introduction

Heart diseases remain as the leading cause of death worldwide [66],[6]. A single myocardial infarction can kill 25% of the left ventricle's cardiomyocytes in a few hours, leading to scar tissue formation and a decline in cardiac function with very limited regeneration [104] –[18].

The microvasculature in the heart microcirculation, comprising capillaries, arterioles, and venules, plays a fundamental role in coronary blood flow, oxygen transfer, and microvessel pressure distribution [8]. Microvascular morphology mirrors the demand of myocardial tissue and infarction triggers substantial structural changes in vascular architecture and the surrounding myocardium [15],[19],[183]. Post-ischemic recovery necessitates re-establishing coronary blood flow via angio-

genesis and arteriogenesis to replenish nutrients and oxygen to the myocardium [19],[18],[183],[42], but the remodeled coronary vessels exhibit enlargement and tortuosity [15],[44].

Ex vivo imaging in rat heart models offers insight into the critical anatomical and functional characteristics of coronary circulation remodeling post-ischemic injury, which cannot be achieved through in vivo organ imaging. Challenges persist in characterizing the complex hierarchical architecture of the coronary vasculature and changes in vessel morphology (e.g., diameters, lengths, curvatures, and branching) and perfusion. Currently, a robust angiographic imaging method is needed to reveal changes in vascular structures at various scales and provide essential hemodynamic and perfusion information after acute myocardial infarction.

Histology examination via microscope is considered the gold standard for identifying pathological morphology changes. Light-based imaging techniques such as confocal microscopy, multiphoton microscopy, and light sheet fluorescent imaging allow for 3D visualization of microvasculature with capillary scale resolution (0.3∼1 μm) but come with numerous drawbacks. Confocal microscopy and light sheet fluorescent imaging have limited light penetration depth in tissue, relying on laborious preparation involving complex tissue-clearing protocols [9]. Moreover, artifacts are often introduced during tissue sectioning, fixation, processing, embedding, staining, and mounting procedures [166]. Tissue sectioning also increases difficulties in maintaining vascular integrity in a relatively large field of view. Additionally, multiphoton microscopy faces a significant challenge due to its slow imaging speed and limited field of view. Consequently, acquiring accurate localized images of functional microvascular and quantifying their characteristics can be challenging using microscope-based imaging techniques.

Optical coherence tomography-based angiography (OCTA) has emerged as a non-invasive optical-based imaging tool capable of generating blood flow images with capillary-level resolution [173],[209]. While OCTA was originally developed for and is primarily used in ophthalmic applications [27],[51], recent efforts have demonstrated its potential as a valuable tool for studying biological processes across various organs. This is attributed to its fast imaging speed (typically between ∼30 seconds per 3D scan for a clinical system) [188], user-friendly operation, relatively wide field of view (mil-

limeter scales) [163], high resolution (μm-order), and high penetration depth (millimeter scale). OCTA maintains sample and vessel integrity, eliminating potential artifacts during sample preparation, ensuring the generation of reliable microvascular images, and facilitating accurate quantification.

Despite the existing research on cardiac tissue morphology, there are very few quantitative evaluations of the microvasculature, primarily due to limitations in required spatial resolution, depth information, and the necessity for vascular network integrity. In this study, we employed a comprehensive OCTA analysis to visualize and quantify the coronary microvascular morphology information of both healthy and infarcted rat hearts, fixed in diastole with retrograde perfusion. We present a framework for image processing and establish several quantitative metrics with high repeatability related to vessel morphology and structure enabling a quantitative comparison among three distinct conditions: healthy (sham) hearts, infarct regions of hearts with induced ischemia, and unaffected regions in infarcted hearts. Specifically, we utilized vessel area density of the capillary (VAD_C) or arteriole/venule networks (VAD_L), vessel complexity index (VCI), vessel tortuosity index (VTI), and flow impairment density (FID), and we demonstrated the consistency between OCTA imaging and histological analysis. The repeatability of these metrics was examined with OCTA scans from the same heart. This approach obviates the need for physically sectioning the heart tissue or utilizing tissue-clearing techniques, which are standard requirements in existing microscopic imaging methods. Overall, our work demonstrates the feasibility of combining OCTA with retrograde heart perfusion to identify quantifiable differences in microscale morphological shifts induced by infarction. This approach may become critical when considering the application of this methodology in assessing therapeutic tissue-engineered vascular constructs.

3.1.2 Methods

Heart Preparation

All animal procedures were approved by the University of Washington Institutional Animal Care and Use Committee (IACUC, protocol #2225-04) and performed in accordance with US NIH Policy on Humane Care and Use of Laboratory Animals.

Eight-week-old male Sprague-Dawley rats (approximately 250-300 g, n=6) were randomly chosen to undergo surgery to induce a myocardial infarction as previously described [143], [14]. Briefly, rats were anesthetized, intubated, and mechanically ventilated. The heart was exposed via a thoracotomy, then the left anterior descending coronary artery (LAD) was temporarily occluded for 60 minutes to cause ischemia by threading a suture around the LAD and tying the suture around flexible tubing. At 60 minutes, the artery was reperfused by cutting the suture. For anesthesia, two intraperitoneal injections of 68.2 mg/kg ketamine and 4.4 mg/kg xylazine were given, one before the surgery and another after ischemia was induced.

Infarcted hearts (n=6) were then harvested four weeks after the ischemia/reperfusion surgery, along with n=6 hearts from an age-matched control group that did not undergo surgery prior to tissue harvest. For euthanasia, an intraperitoneal injection of 1.5 mL Euthasol was administered.

Once the rats were no longer breathing and were not responsive to a toe pinch, the heart was exposed by opening the chest. Before removing the heart, two solutions were circulated through the heart by injecting the solutions into the inferior vena cava while the heart was still beating. First, 50 U heparin was injected to prevent thrombosis, and then supersaturated potassium chloride was injected to arrest the heart in diastole. After excision, a blunt tip needle was used to cannulate the aorta and allow for retrograde perfusion. Then, the heart was perfused with PBS containing 4 mg/L Papaverin and 1 g/L adenosine to dilate the vasculature. Immediately following, the heart was perfused with 4% paraformaldehyde at a constant pressure of 100 mm Hg for 10 minutes. The hearts were further fixed in 4% paraformaldehyde overnight before being rinsed with and stored in PBS until imaging.

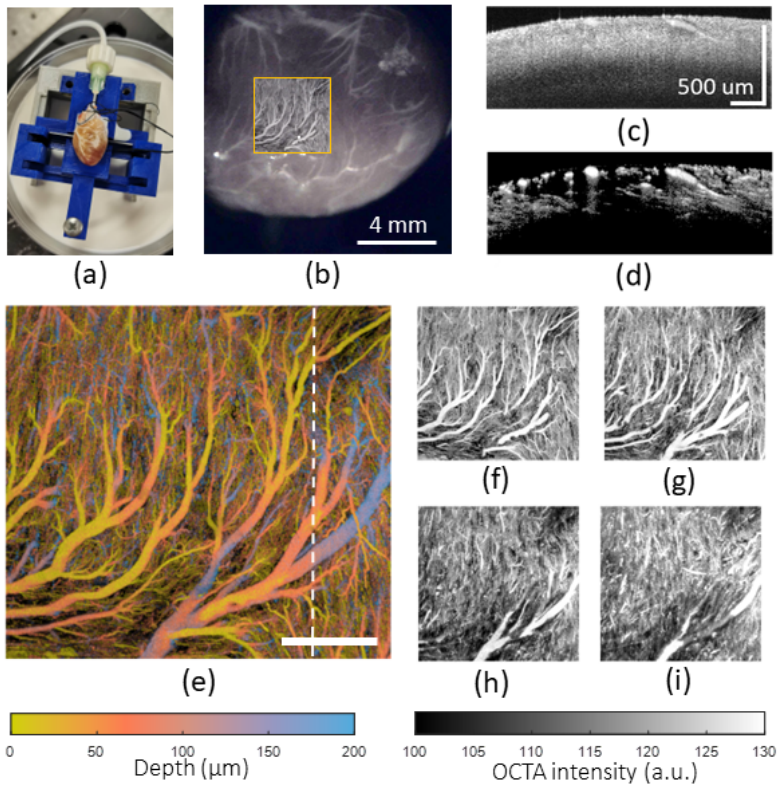

Figure 3.1: Experimental setup and imaging processing. (a) A representative rat heart fixed to a 3D printed mount with retrograde perfusion of Intralipid solution. (b) Representative white light image overlaid with a corresponding en face OCTA image. (c, d) Representative B-scan images of OCT structure and OCTA blood flow were acquired from the position marked by the dotted line in (e), where penetrating vessels can be appreciated. (e) Pseudo-color-coded OCTA projection image indicating the depth of vessel information. (f – i), Demonstrations of en face OCTA projection slices obtained from depth-resolved slabs defined by (f) 1-50 μm, (g) 51-100 μm, (h) 101-150 μm, and (i) 151-200 μm, respectively.

During imaging, 10% Intralipid solution (diluted in PBS by volume) was perfused through the coronary vasculature via retrograde perfusion through the cannulated aorta to provide a light-scattering contrast mechanism [14]. The Intralipid in the heart was allowed to flow under a stable pressure (100 mmHg) for 10 minutes prior to imaging to ensure microvascular perfusion and the pressure was maintained at 100 mmHg throughout the imaging process. A 50 μL drop of glycerol was applied to the tissue surface 10 minutes prior to imaging as an index-matching agent to minimize the effect of surface specular reflection on the final results [189] –[190]. During imaging,

each sample was placed at the center of a Petri dish using a 3-D printed mount to prevent sample motion (Fig. 1a).

Swept-Source Optical Coherence Tomography and Imaging Protocol

An SS-OCT imaging system that provided flexible focus alignment was used in this study, which has been described in detail elsewhere [163]. Briefly, the system used a vertical-cavity surface-emitting (VCSEL) swept laser source (SL1310V1-10048, Thorlabs Inc., Newton, NJ) with an A-scan speed of 200 kHz, a central wavelength of 1310 nm, and a spectral bandwidth of 100 nm, providing an axial resolution of ∼10 μm. The imaging probe incorporated a 5× objective lens (LSM03, Thorlabs Inc., NJ, USA) delivering a lateral resolution of ∼20 μm and a depth of focus of ∼130 μm (defined by the Rayleigh length). The sample arm included a built-in camera to provide a concurrent white-light image co-aligned with the OCT field of view (FOV) for ease of imaging. The imaging probe was fixed on a stable support stand with 3 degrees of freedom to allow for crude and fine (micrometer-level) focus alignment during imaging. This flexible focusing approach was specifically adopted to address and compensate for the challenges posed by the heart's curved surface geometry.

For the infarcted hearts, we selected and scanned four regions of interest near the left anterior descending coronary artery (area local to the infarct event) and four remote regions on the posterior side of the heart. The purpose of selecting remote regions in our study was to identify whether alterations in microvasculature are primarily localized or if there are systemic responses affecting multiple regions of the heart. For the healthy hearts, we selected and scanned four regions similar to those corresponding to the infarct and remote regions of the infarcted hearts. Each session consisted of a co-aligned white light image (∼12 mm × 12 mm) followed by a 4 mm × 4 mm × 1 mm (x, y, and z direction) OCTA 3D scan (Fig. 1b). The white-light image from each scan session provided anatomical markers used to verify regions for comparison of OCTA images between groups.

In all acquisitions, a B-M mode scanning protocol was performed where 800 A-scans were acquired along the X-direction (fast-scan axis) to compose a single B-scan and then repeated at the same location to create an MB-scan at 200 fps. Eight repeat B-scans were taken at each location to facilitate the reconstruction of OCTA microvascular and OCT structural images [51]. This B-M scan protocol was consecutively performed at 800 equal-spaced locations along the Y-direction (slow-scan axis) to complete a 3D scan, which took a total of ∼32 seconds.

OCTA Imaging Processing

The mean OCT intensity B-scan image was taken for each 8-repeated B-frames and then log-compressed to reconstruct a tissue structural image based on light scattering (Fig. 1c). Due to the scattering and absorption property of light in the cardiac tissue, the light was nearly attenuated to below the noise floor at depths greater than 400 μm in all samples (Fig. 1c).

Temporal changes across the eight repeated B-scans were used to reconstruct vascular structures using the eigen decomposition-based optical microangiography (ED-OMAG) method to create OCTA images [197]. ED-OMAG uses eigen decomposition statistical analysis as a high-pass frequency filter to remove the static signal that is related to motionless tissue. Fig. 1d is a representative OCTA B-scan image corresponding to 5.1c.

To quantify the vascular features, we followed a strategy commonly used in clinical ophthalmology, where *en face* images generated from 3D scans were often used to quantify retinal vascular networks (5.2). To generate the OCTA *en face* image, a user-guided semi-automated segmentation software was applied to the 3D OCT structural data to identify the tissue surface [194]. The *en face* image was generated from the 3D vascular image using the maximum-intensity projection of the flow signals. Depth-resolved mapping of microvasculature relative to the tissue surface within 200 μm depth is shown using a pseudo-color-coded projection image (5.1e), where the superficial vessels are colored in orange and the deeper vessels are colored in blue.

The capillary networks are substantially dense in the myocardium, requiring the use of thin segmentation layers (or slabs) to separately visualize them. Figs. 1 f-i shows representative depth-

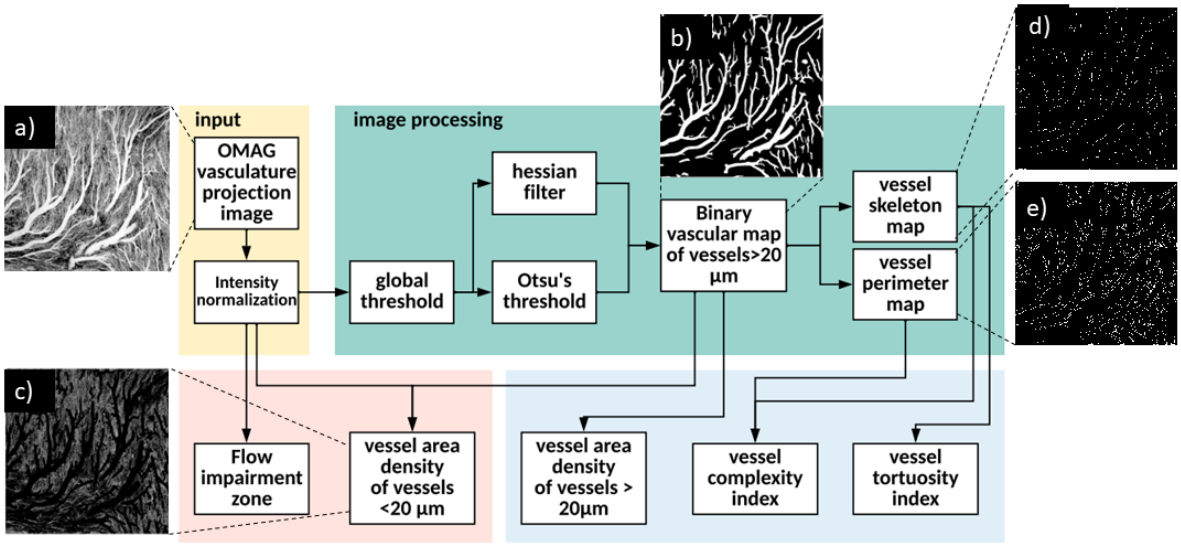

Figure 3.2: Illustration of the framework for quantification assessment, consisting of 4 blocks, i.e. "input", "image processing", "quantification of vessels 20 µm", and "capillary quantification", respectively, to derive the quantitative vessel area density (VAD), vessel complexity index (VCI), vessel tortuosity index (VTI), and flow impairment density (FID) according to the processing steps described in section II.D. (a) The input en face vascular image that is quantified. (b) binary map representing the vessels of 20 µm. (c) binary map representing capillary vessels. (d) vessel skeleton map from (d), and (e) vessel perimeter map from (d).

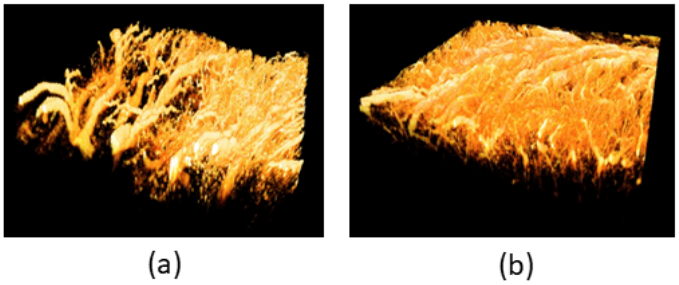

Figure 3.3: Visual demonstration of capillary loss in the 3D rendered OCTA images obtained from (a) infarct region, and (b) healthy region.

resolved en face projection images for depth slabs of 1-50 µm, 51-100 µm, 101-150 µm, and 151-200 µm below the heart tissue surface. A dense capillary bed could be well-appreciated across different depths. The *en face* image projected from 50 µm below the surface of the tissue was used for further quantification (Fig. 1f) due to the limited depth of focus in the system as well as the

surface curvature of the tissue. The relatively small axial range for producing projection images ensures most vessels remain within or close to the focal plane of the objective lens and provides consistent SNR and lateral resolution between scans [17].

Vascular Quantification

In this study, we employed a 20 μm cut off to distinguish capillaries (or small vessels) from relatively larger vessels. This choice was empirical and considered reasonable for the following reasons: 1) it encompasses the typical size range of capillaries, which generally falls between 5 and 10 μm, while excluding larger vessels, and 2) the lateral resolution of the imaging system is approximately 20 μm. This distinction is crucial for analyzing microvascular networks and understanding the perfusion dynamics within myocardium tissue. It is important to note that the specific cutoff value may vary depending on the context, the imaging system, and the characteristics of the tissue under investigation. With this consideration, we proposed to use five vascular metrics:VAD_C, VAD_L, VCI, VTI, and FID to quantify vessel morphological structures based on an automated processing scheme that was clinically validated in ophthalmic imaging (5.2) [20],[5]. The quantification workflow is shown in 5.2.

Briefly, the *en face* image generated from a superficial 50 μm thickness slab (5.2a) was passed through an image processing block, as shown in 5.2, to generate a series of binary images representing different characteristics of the vessel appearance for the later quantifications. To achieve this, the original image (5.2a) was first normalized/scaled to a dynamic range from 0 to 1 (0 to 255 digital depth). Subsequently, a combination of Otsu's thresholding method and Hessian-based Frangi vesselness filtering [65] was applied to generate a first binary image, representing the vessels with diameters greater than 20 μm (binarized larger vessel map, 5.2b). From this binary map, two additional binary maps of vessel skeleton (5.2d) and vessel perimeter (5.2e) were generated following the methods described in [181], where the vessel skeleton map represents the vessel lengths and vessel perimeter map indicates the perimeters of the vessels larger than 20 μm within the slab.

Lastly, a binary map that represents all the capillary vessels (5.2c) was generated from the binarized image of the original image (i.e., 5.2a) with the larger vessels (5.2b) removed.

The vessel area density of capillaries (VAD_C, e.g., from 5.2c) and of vessels with a diameter greater than 20 μm (VAD_L, e.g. from 5.2b) was calculated by the ratio between discrete pixels occupied by vessels to all pixels in the binary OCTA image.

The vessel tortuosity index (VTI) was determined from the skeletonized vessel map of large vessels (5.2d), where the skeletonized vessels were separated into multiple segments by each node and endpoint for VTI calculation. The skeletonization process and endpoints and branch point extraction were obtained with the built-in MATLAB function "bwmorph." The VTI value was calculated using a simple arc-to-chord ratio method, where the length of the curve between two endpoints of vessel branches was divided by the length of the curvature of each vessel between subsequent nodes or endpoints. The 'arc' to 'chord' ratio was quantified for each vessel segment separately. Finally, the global average VTI from all segments was calculated from the average of the local curve length of the nth vessel segment between two endpoints (representing the arc length), and the Euclidean distances between the ends of the nth vessel branch using the discrete locations of each node or endpoint of the vessel in the X- and Y- coordinate space. The vessel complexity index (VCI) was calculated by the ratio of vessel perimeter (5.2e) to vessel area (5.2b) of each vessel greater than 20 μm. The VCI is a unitless index that estimates the vessel structures' additive perimetric complexity. Additive means that the complexity of the shape is equal to the sum of the single shape complexities measured separately, where a single circle is the simplest shape that has a complexity of 1. This method has been demonstrated to show complexity characteristics in retinal vasculatures [181]. The flow impairment density (FID) was evaluated where the pixels without OCTA flow signal (Q_{ij}) were used to calculate the total no-flow regions. As such, the FID was calculated by the percentage of discrete pixels that do not have vessels in the binary OCTA image.

These five quantitative metrics above were quantified from the 4 mm × 4 mm OCTA *en face* images captured from each group. The mean and standard error of the mean (SEM) were cal-

culated for each condition: healthy, ischemic, and remote regions of the hearts. The differences between infarct and control regions were estimated using a nested one-way ANOVA to quantify variations in the mean values among each group (alpha <0.05). The null hypothesis for the nested one-way ANOVA test is defined as there is no difference in the mean value between the four hearts across the three groups. It is noteworthy for the healthy hearts that there was no significant difference in any of the metrics assessed above between the regions similar to those corresponding to the infarct sites and the remote regions, as expected.

Repeatability Testing

A repeatability study was conducted to determine each metric's reliability regarding imaging and focusing variations, using a series of scans from the same heart around similar regions. To perform the test, the scans were taken after removing the sample from the scanning probe and re-aligning it with the probe to explore how readjusting the sample may affect the quantification. The entire realignment procedure was repeated three times, resulting in 3 individual scans, each performed by the same user, to examine scanning and experimental variability. The coefficient of variation between the 3 scans was then calculated to express the repeatability of the quantification algorithm.

A small coefficient of variance ($< 5\%$) was determined for each metric when tested over multiple scans with overlapping FOV and slightly different focus positions. As such, quantitative metrics compared between samples and different imaging regions with coefficients of variances represent morphological changes independent of user setup.

Histology

Following OCTA imaging, each heart was sliced into 2 mm-thick sections from the apex and processed for paraffin embedding. Further, 4 μm sections were cut and stained for picrosirius red/fast green to visualize the infarcted regions or for Griffonia simplicifolia lectin (GSL) to visualize vascular lumens. For GSL staining, slides were blocked with 1.5% normal donkey serum

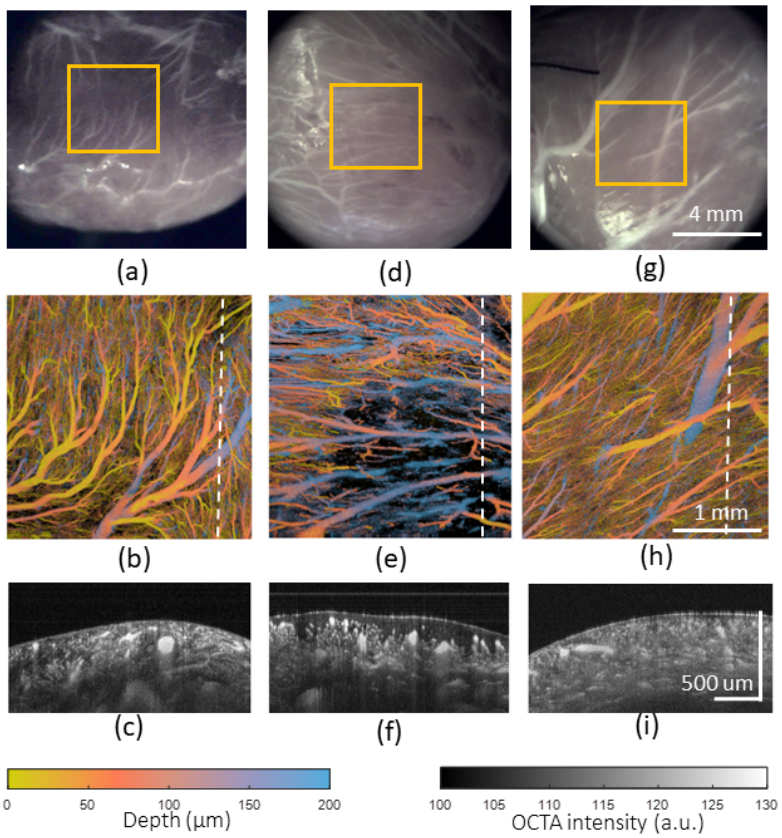

Figure 3.4: Representative white light and en face OCTA images of the cardiac microvasculature in (a-c) healthy, (d-f) infarct and (g-i) remote regions. (a, d, g) The regions marked with yellow boxes in the white light images indicate the scanned regions. (b, e, h) Depth-resolved en face OCTA images with depth information coded with colors shown in the color bar. (c, f, i) Representative cross-section OCTA images at the positions marked as dashed white lines in (b, e, h), respectively.

followed by sequential staining with GSL (Vector L-1100-5, 8 μg/mL), goat Ab to GSL (Vector AS-2104, 1:100), and a fluorescent secondary antibody. The infarct size was assessed from picrosirius red/fast green staining. The histological vessel area, density, and size were quantified with a custom MATLAB code that analyzes confocal microscopic images of GSL-stained slides. Statistical analysis (ANOVA) was used to determine the significance (alpha$<$ 0.05) between groups.

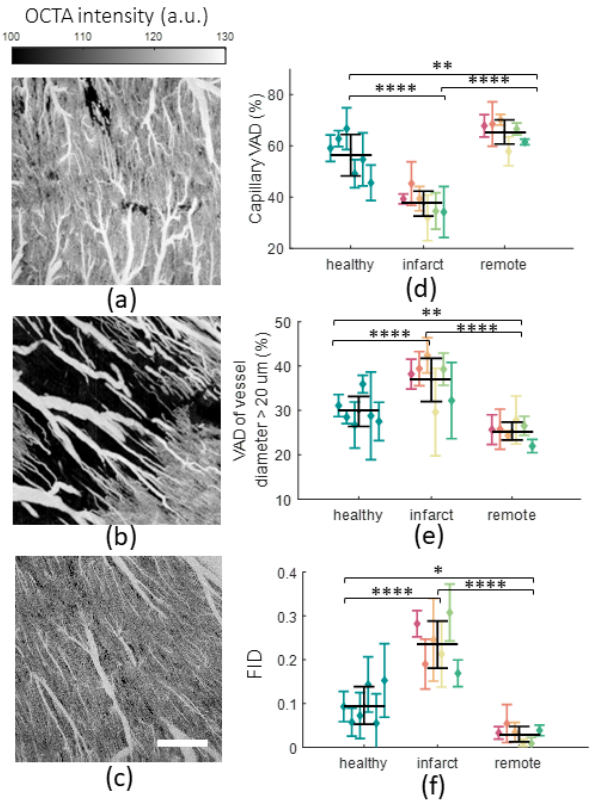

Figure 3.5: Quantification of vessel density. (a, b, c) Representative *en face* OCTA images of (a) healthy, (b) infarct, and (c) remote regions, respectively. (d, e) Quantification of vessel area density of (d) capillaries (<20 μm) and (e) arteriole/venule-sized vessels (>20 μm) as a percentage of total scan area. (f) Quantification of FID as a percentage of total area. The mean (± SEM) of each group was shown in black. The mean (± SEM) for each individual animal was shown in color with infarct and remote regions on the same heart shown in the same color. *, **, and **** represents statistical significance of p <0.05, 0.01, and 0.0001 correspondingly.

3.1.3 Results

OCTA of Healthy and Infarcted Hearts

3.13 demonstrates the visualization of the vascular information of an infarct (5.3a) and a healthy (5.3b) region from the 3D volume rendering, respectively. The left part of the 3D volume in the infarct region (5.3a) shows a dramatic loss in capillary vessels exposing the vessels, with relatively larger diameters in the tissue. To assess the differences in microvasculature between healthy and infarcted rat hearts, we created 2D *en face* 4 mm × 4 mm OCTA images for visualization

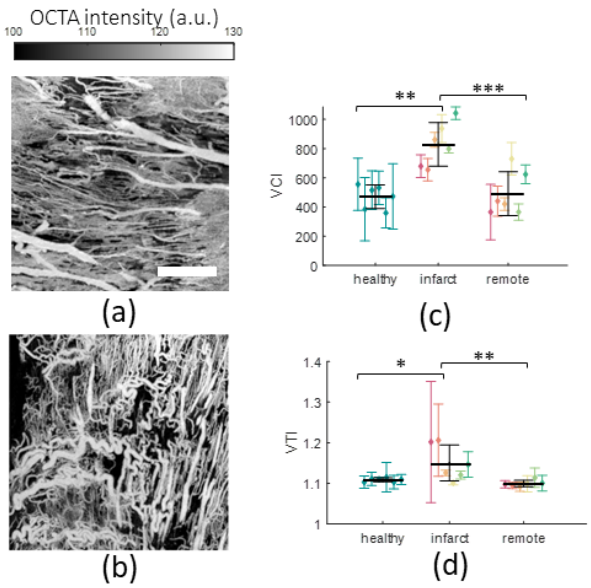

Figure 3.6: Quantification of the vessel structure. (a, b) Representative *en face* OCTA images from infarct regions from 2 different hearts. Scale bar represents 1 mm. (d) Quantification of vessel tortuosity index for larger vessels (< 20 μm). The mean (± SEM) of each group was shown in black. The mean (± SEM) for each animal was shown in color with infarct and remote regions on the same heart shown in the same color. *, **, and *** represents statistical significance of $p < 0.05$, 0.01, and 0.001, respectively.

and quantification of coronary vasculature (5.4). For quantitative analysis, the *en face* image was used to characterize vasculature morphology in each region in terms of its density and vessel size. Qualitatively, the healthy-heart region (5.4b) and remote region of the infarcted heart (5.4h) were not obviously different in microvascular structure, however, the infarct region showed a dramatic reduction in microvascular density (5.4e).

We quantified the vascular density of both capillary (< 20 μm) and arteriole/venule-sized vessels (> 20 μm) using VAD (5.5). The capillary VAD (VAD_C, 5.5d) was approximately 19∼28% lower in the infarct region (37% ± 2%) (mean ± SEM) than in both healthy (56% ± 3%) and remote regions (65% ± 2%), however, VAD for arteriole/venule sized vessels (VAD_L, 5.5e) was 4∼12% greater in the infarct region (37% ± 2%) than in healthy (29% ± 1%) and remote regions (25% ± 1%). This indicates that post-infarct remodeling caused a shift towards larger-sized vessels,

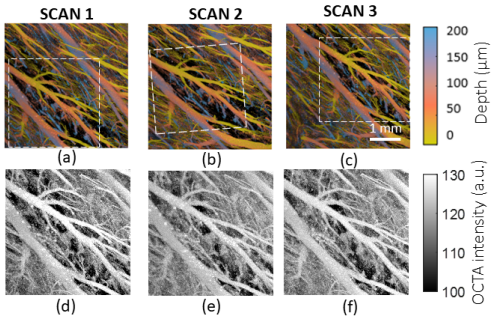

Figure 3.7: Demonstration of repeatability of OCTA imaging on an infarcted heart. (a-c) en face MIP covering a scan area of 4 mm × 4 mm (d-f) cropped area that contains a common region in each scan.

agreeing well with the observations described in the histological studies (3.10 b and d). In combination, the total VAD (comprising of both VAD_C and VAD_L) was also 12∼17% lower in the infarct regions (74% ± 4%) than in healthy (86% ± 3%) and remote regions (91% ± 2%). Additionally, we assessed the flow impairment (i.e., FID, 5.5f), which is the converse of the total VAD. The FID was 6∼20% significantly larger, in the infarct region (23% ± 2%) relative to both healthy (9% ± 1%) and remote regions (3% ± 1%). These results show that vascular remodeling following myocardial infarction leads to more sparse vascularization with a shift towards larger vessels.

Next, we assessed vascular morphology after myocardial infarction using two metrics: VCI and VTI. Visually, the vessels appeared more complex and tortuous in the infarct region than in the healthy region. Figs. 6 a, and b. are two extreme examples of infarction regions with increased microvasculature complexity and tortuosity. Quantitatively, the vessels within the infarct region were more complex with VCI being significantly greater in the infarct region (828 ± 61.1) relative to both healthy (469 ± 33.0) and remote regions (490 ± 61.5). Similarly, the vessels within the infarct region (1.15 ± 0.002) were more tortuous, however, not significantly different compared to the healthy (1.1 ± 0.003) and remote regions (1.1 ± 0.002). Interestingly, three of the six infarct hearts showed an increase in vessel tortuosity. These two metrics quantitatively showed that the microvascular morphology in the infarct region was generally more complex and more tortuous compared to the undamaged and controlled region.

It is noteworthy for the healthy hearts that there was no significant difference in any of the metrics assessed above between the regions similar to those corresponding to the infarct sites and the remote regions, as expected. Taken together, these results indicates that OCTA quantification can be used as an informative tool to assess differences in vascular density and morphology between infarcted and healthy hearts.

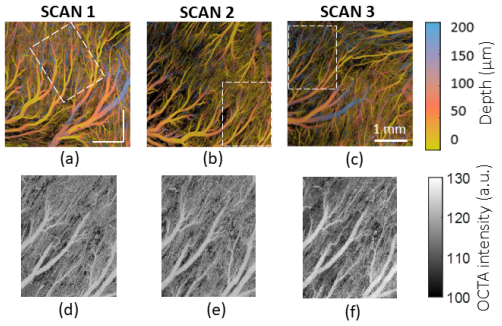

Figure 3.8: Demonstration of repeatability of OCTA imaging on a healthy heart. (a-c) en face MIP covering a scan area of 4 mm × 4 mm. (d-f) en face image from the cropped area that contains an overlapping region in each scan.

Repeatability Testing

The vessel quantification algorithm repeatability was tested using three scans from the same heart that were cropped according to the local overlap (5.7 and 3.7). The testing results are tabulated in Tables I and II, showing high repeatability of the quantification values with relatively small coefficients of variance (with CV <% 5) within the three scans. The global quantitative OCTA parameters have shown low variance regardless of different scans. The results also showed that quantifications for both healthy and infarct hearts were relatively insensitive to differences in user variability from scan to scan.

Histological Analysis

To validate OCTA, histology was performed on healthy and infarcted hearts following OCT imaging. Picrosirius red/fast green staining was used to visualize healthy (stained green) and in-

Table 3.1: Repeatability test on one infarct heart

	VAD_C	VAD_L	VCI	CTI	FID
Scan 1	0.27	0.22	351.15	1.09	0.324
Scan 2	0.29	0.24	319.63	1.09	0.299
Scan 3	0.28	0.23	321.87	1.09	0.299
CV	0.027	0.035	0.053	0.004	0.048

farcted tissue (stained red for collagenous scar) in all hearts to ensure that imaged regions were appropriately characterized. No scars (labeled in picrosirius red) in all hearts to ensure that imaged regions were appropriately characterized. No scars are found in healthy hearts (3.9a). Infarcted hearts contain large regions of picrosirius red+ stains, indicating infarcts were successfully generated by the ischemia/reperfusion surgery (3.9b). Additionally, histological analysis confirmed that the infarcts reached the surface of the heart, the region imaged via OCTA, for all infarcted hearts in this study. All infarcts were appreciable and similar in size (22.96 ± 2.54 % of the left ventricle area). This staining confirms the state of the tissue and that infarcts were present where imaged.

To visualize vascular patterns, histological sections were also stained for Griffonia simplicifolia lectin (GSL), which labels the endothelium. The healthy and remote regions displayed many small, dense lumens, whereas the vasculature in the infarct region appeared highly irregular and void of many small capillaries (3.10a, b). Histological analysis confirmed that the blood vessels occupied a greater portion of the total area in healthy (15.13% ± 0.66%) and remote regions (14.37% ± 0.50%) when compared to infarct regions (7.46% ± 0.58%) (3.10c). There were 300% more vessels per mm^2 in the healthy (1122.64 ± 110.15 mm^2) and remote (1027.13 ± 44.21 mm^2) regions compared to the infarct region (275.75 ± 14.48 mm^2) (3.10d). Additionally, infarct regions (281.83 ± 31.4 mm^2) had greater average vessel sizes than in healthy (140.73 ± 5.69 mm^2) and remote regions (143.14 ± 4.65 mm^2) (3.10e). These results confirm the trends of lower vascular density and larger vessel sizes demonstrated in the OCTA imaging, reaffirming the ability of OCTA to capture relevant differences between infarcted and healthy vasculature.

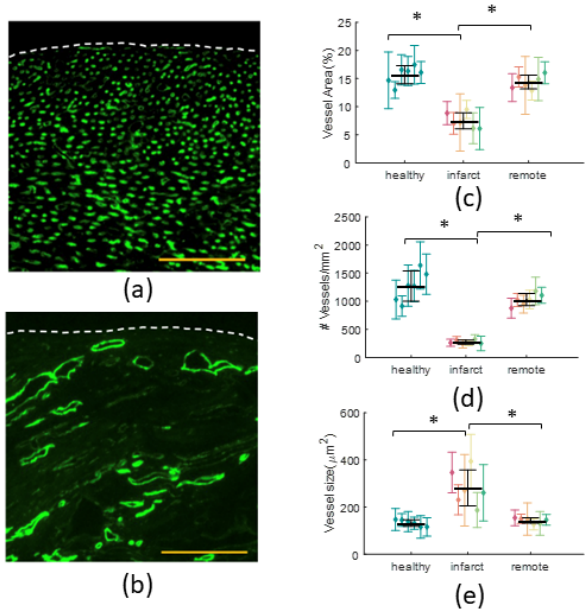

Figure 3.9: Histological analysis of vasculature by Griffonia simplicifolia Lectin (GSL) staining. (a, b) Confocal images of (a) healthy and (b) infarct regions stained for GSL in green. A dashed white line marks the surface of the heart. Scale bar = 200 μm. (c-e) Quantification of (c) vessel area as a percentage of total area, (d) vascular density, and (e) average vessel size per region. * represents statistical significance of $p < 0.05$ using ANOVA.

3.1.4 DISCUSSION

Myocardial infarction leads to deleterious vascular remodeling and is a risk factor for heart failure [139],[165]. In this study, we have demonstrated the use of the OCTA technique to image vascular structural changes in *ex vivo* fixed rat hearts post-infarction. In comparison to other imaging approaches, OCTA offers a user-friendly and fast imaging approach with high repeatability for capturing complex 3D microvascular architecture with high resolution and a relatively wide field of view. This makes it a valuable imaging tool for studying vascular remodeling. Importantly, the technique provides detailed vascular maps with minimal damage to the cardiovascular networks, preserving the heart's condition for further quantitative analysis. In addition, OCTA also avoids artifacts from tissue sectioning, staining, or clearing that other light-based imaging techniques require.

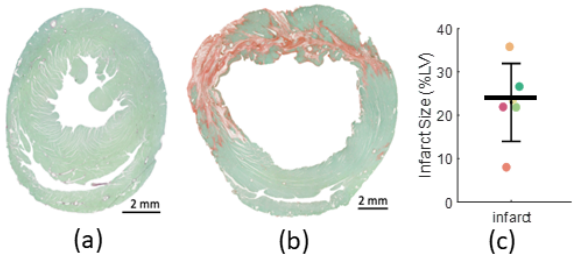

Figure 3.10: Histological analysis of healthy (a) and infarcted (b) hearts by picrosirius red/fast green. Healthy tissue stains green, and infarcted tissue stains red. (c) Quantification of infarct size as a percentage of left ventricle area.

Table 3.2: Repeatability test on one healthy heart

	VAD_C	VAD_L	VCI	CTI	FID
Scan 1	0.65	0.18	129.86	1.10	-
Scan 2	0.60	0.19	126.52	1.09	-
Scan 3	0.63	0.20	131.52	1.09	-
CV	0.040	0.042	0.020	0.006	-

Histological analysis was employed to complement the OCTA measurements, confirming capillary loss and increased remodeling in larger-sized vessels in infarct regions. Although histology has been considered the gold standard for assessing pathological changes in various diseases, traditional 2D histology falls short of providing sufficient information to study the tortuosity and complexity of the vasculature, leading to an incomplete understanding of vascular changes. OCTA, on the other hand, maintains sample integrity while providing valuable morphologic information about the vasculature, enabling a greater understanding of vascular architecture compared to histology.

This study represents the first instance in which both capillary-sized vessels and larger vessels were measured and analyzed separately using wide-field imaging with capillary-level resolution. The quantification framework could offer valuable insights into microvascular remodeling during the development and progression of ischemic heart disease.

Capillary loss is well-recognized in ischemic heart disease, resulting in reduced blood flow to the infarct zone, including its residual heart muscle[68]. In the acute phase of infarction, many

capillary endothelial and perivascular cells are killed by ischemic injury, contributing to the "no-reflow phenomenon" of incomplete reperfusion [128]. In the chronic post-infarct phase, there is a slow loss of microvessels through the poorly understood process of rarefaction [44], which can contribute to the progression of heart failure. Such loss of microvasculature results in a longer diffusion distance to nearby tissue and reduced accessibility for oxygen and nutrients in the infarcted myocardium [10] –[47]. Our quantification matrices yielded measures of the massive capillary loss and vascular remodeling in the infarct region. The decrease in capillary VAD and the increase in FID both indicate severe structural damage to local coronary capillaries as a result of myocardial infarction.

Microvascular remodeling also involves changes in the structure and function of the small blood vessels that supply blood to the heart muscle. These changes can include the formation of new blood vessels (angiogenesis), the dilatory growth of existing blood vessels (arteriogenesis), and the formation of collateral circulation (the development of new pathways for blood flow around blocked or damaged blood vessels). The increase in VAD_L for arteriole/venule-sized vessels within the infarct region observed in this study suggested potential vessel expansion, consistent with other studies [15].

Additionally, newly formed vessels within an infarct region may involve the growth and branching of blood vessels in a more random or tortuous manner. Coronary artery tortuosity has been associated in clinical research with myocardial perfusion defects, impaired relaxation of the left ventricle, hypertension, and chronic pressure overload hypertrophy; It is crucial to analyze this tortuosity at the capillary level, as opposed to the level of larger arteries, due to its direct implications for nutrient exchange, oxygen provision, and angiogenesis about blood flow [123]. Reducing capillaries elevates blood flow resistance in the upstream arterioles and arteries. Increased resistance necessitates greater pressure to maintain blood flow, leading to arterial wall stress [16]. Over time, this resistance can result in arterial remodeling and the formation of tortuous vessels, especially at turning points or bifurcations where hemodynamic forces are most irregular and pronounced [117]. These tortuous vessels are less efficiently perfused and may contribute to ongoing

myocardial ischemia. Vessel tortuosity remains one of the most common pathological biomarkers in impaired myocardial hemodynamics and may be crucial to comprehending the development mechanism of heart failure [74].

The findings from this study revealed a statistically significant increase in VCI within the infarct region, suggesting that this metric holds promise as a reliable indicator for capturing alterations in the geometric characteristics of coronary vasculature following myocardial infarction. In contrast, noticeable morphological changes in the vasculature patterns would be challenging to distinguish with tissue sectioning or without the large field of view provided by OCT imaging.

While the VTI metric is less sensitive to differences between the infarct region and healthy or remote regions, three out of six hearts investigated in this study showed an increase in VTI in the infarct region. This result may suggest that tortuous vessel reconstruction after myocardial infarction might not occur consistently. Indeed, even in the animals where it occurred, tortuosity was spatially quite variable (5.6d). Additionally, VTI might not be sensitive to the *en face* OCTA image because the projection view conceals tortuosity in the z-dimension, and VTI would not be sensitive to infarct regions with a significant lack of vasculature. 3D vessel tracing could be more suitable for case studies on tortuosity quantification on single vessels and should be addressed in future studies.

In addition to identifying quantitative and qualitative differences from the OCTA image between different pathological conditions of the heart, we have demonstrated high consistency of OCTA imaging and our processing framework through a repeatability test. The low CV values in this test indicate that our quantification method was relatively repeatable between scans (CV$<$ 5%). This suggests that most of the variability detected between samples reflected biological variability in microvascular structure. Although the microvasculature patterns vary between different spatial locations, a quantitative assessment performed over the wide field projection image would avoid an inaccurate local quantitative characterization of the microvasculature.

Nonetheless, our research holds promise in advancing the detection and potential prediction of myocardial infarction moving beyond the primarily observational role of quantitative analysis.

The study can be directed toward a more precise and predictive methodology as we expand our dataset and refine clinical profiles. While the feasibility of OCTA to identify differences in vessel morphology between healthy and infarcted hearts has been demonstrated, limitations exist in this study. The uneven surface of the heart and the current transverse resolution of the system impact the sensitivity to capillary visualization near the heart tissue surface, causing slight non-uniformity and blurring of vessels located outside the depth of focus (DOF) region. For this reason, we chose a relatively shallow depth of 50 μm for a more accurate quantitative evaluation of microvascular structures in our study. Mitigating this issue could involve improving the confocal function so that the microvascular features across the whole imaging depth can be quantified, i.e. to increase the DOF, by employing an extended-focus configuration at the sample arm where the illumination and detection beams are engineered to increase the DOF while maintaining a constant transverse resolution[163]. Another solution would be to employ a variable focusing mechanism with an electrically tunable lens in the system [**1**]. While these alternative solutions are plausible, they would inevitably increase the system complexity and reduce overall imaging speed.

Although OCT imaging allows for imaging as thick as 2 mm within non-transparent biological tissues while maintaining cellular resolution [188],[163], only a depth of 400 μm for OCT imaging and 200 μm for OCTA imaging (Fig. 1 f-i) were visualizable in myocardial tissue due to intralipid's high intrinsic scattering property that severely attenuates OCT light penetration. Imaging microvasculature located at tissue depths deeper than 200 μm could be achieved using tissue-clearing methods [9], or variable focusing with a tunable lens [117]. Improving depth-resolved imaging remains an area of focus for OCTA imaging methods.

Note that VCI, VAD_L, and VTI do not include signals from capillaries largely due to the limitation of the transverse resolution of our imaging system (which was $\sim$20 μm), as well as the dense nature of myocardial capillary networks where the inter-capillary spacing is often around 20 μm in a healthy heart. In addition, the binary mask generated by a combination of Otsu's thresholding method and hessian-based Frangi vesselness filtering further limits our ability to accurately quantify the capillary morphologies. For these reasons, the metric of VAD_C should be viewed as

an estimation. However, considering that capillaries generally have an average diameter of around 8 μm and larger vessels exceed this (20-200 μm), a 20 μm threshold provides a logical midpoint to distinguish between the capillaries and the larger blood vessels.

A final limitation is that the current method requires the hearts to be fixed in diastole, which limits the exploration of flow dynamics. To overcome this limitation and investigate microvascular patterns throughout the beating cycle for a detailed understanding of microvasculature remodeling post-ischemic injury, alternative approaches such as retrograde perfusion in beating hearts e.g., with a Langendorff system, along with time-gated OCT, may be necessary. Time-gated OCT canmay be either achieved by integrating advanced cardiac motion compensation algorithms or high-speed imaging technologies such as the line scan OCT that counteracts the beating motion of the beating heart [74],[121]. Exploring flow dynamics during the cardiac cycle would provide valuable insights into microvasculature remodeling following ischemic injury.

3.1.5 CONCLUSION

We have demonstrated capillary-level resolution reconstruction of heart microvasculature using OCTA over a relatively large field of view with depth acquisition. A method for quantifying microvessel morphology was presented to summarize unbiased microvascular characteristics in healthy and infarcted rat hearts with high repeatability. Significant changes in vessel density and morphology observed after myocardial infarction align with the histology analysis. These parameters may serve as valuable pathological biomarkers for investigating infarct conditions in the heart. Using OCTA to visualize the microvasculature down to the capillary level with a wide field of view may provide a valuable means to further understand the microcirculation remodeling processes in cardiac microvascular research.

3.2 Quantification of Microcirculation in Infarcted Rat Hearts Using Optical Coherence Tomography Capillary Velocimetry

Myocardial microcirculation plays a critical role in sustaining the heart's metabolic demands, supplying oxygen and nutrients essential for cellular function, and supporting overall cardiac performance. Following myocardial infarction (MI), effective microcirculation is pivotal for tissue repair and remodeling; however, disruptions in microvascular integrity and flow dynamics can lead to inadequate perfusion, exacerbating tissue damage and impairing recovery. However, microvascular hemodynamic dysfunction post-MI remains poorly characterized, largely due to the limitations of existing imaging methodologies, which fall short in accurately quantifying capillary velocities in cardiac tissue. In this study, we employ Optical Coherence Tomography Angiography (OCTA) within a Langendorff-perfused rat heart model to assess microvascular velocity and hemodynamic alterations following infarction. Using Eigen Decomposition-based optical microangiography (ED-OMAG) and capillary velocimetry (ED-velocimetry), we are able to visualize and quantify capillary velocities to examine the infarct-induced changes in both the microvascular architecture and flow dynamics. Our analysis revealed a 30.4% reduction in vessel area density, a 72% decrease in average capillary velocity, and a 79% decline in perfusion index in infarcted zones relative to healthy myocardium. Additionally, vasculature projection images indicated elevated vessel tortuosity, which was inversely correlated with mean capillary velocity in infarcted regions. These results underscore substantial myocardial microvascular deterioration and remodeling at 4 weeks post-infarction, highlighting a compromised capacity for restoring adequate perfusion. This study establishes the utility of ED-based velocimetry for detailed myocardial hemodynamic assessment and demonstrates the potential of OCTA for detecting coronary microvascular impairment and related perfusion deficits.

3.2.1 Introduction

Myocardial infarction leads to significant structural dysfunction within the coronary microcirculation [56, 64, 77, 141, 164]. Even after successful restoration of blood flow in larger coronary arteries, microcirculatory dysfunction is irreversible and leads to chronic ischemic damages [46, 141]. Approximately 50% of patients fail to recover optimal myocardial perfusion[134]. While coronary microcirculation is responsible for 75% of myocardial blood flow, it is primarily influenced by capillary flow disturbances following myocardial infarction (MI)[159].

Recent studies have shown insights into heart capillaries' structural and functional alterations following MI, including a significant drop in capillary blood volume as well as tortuous and enlarged vessels [135, 136]. The characterization of myocardial perfusion often uses capillary morphology, structural integrity, and RBC passage speed to demonstrate the ischemic damage [70, 135, 136, 146, 186]. Microvascular abnormalities, such as capillary occlusions, endothelial swelling, pericyte constriction, and capillary compression, impede the normal function of the capillaries, leading to irregular perfusion patterns and uneven capillary flow that affect the overall circulation [137].

Dysfunction in myocardial perfusion has been widely reported, with ischemic regions often exhibiting reductions in capillary flow that are accompanied by changes in capillary flow resistance and speed, thereby increasing heterogeneity in microvascular blood passage [90, 100]. This heterogeneity has been identified as a critical factor influencing microcirculation function in the myocardium and is essential for sustaining the heart's metabolic demands [137]. Therefore, alterations in capillary velocity within the infarcted area emerge as key indicators for characterizing perfusion properties post-MI, providing valuable insights into the state of cardiac microvascular function.

However, measuring the capillary velocity requires high spatial and temporal resolution to capture the fine-scale and rapid changes in blood flow within the microvasculature. To spatially resolve blood vessels less than 200m in diameter and to measure velocities in capillaries, OCT is introduced in this study for its ability to provide high-resolution, real-time measurements of cap-

illary velocity in a controlled ex vivo environment. Unlike microscope imaging, which requires tissue clearing or sectioning [132, 167], OCT has demonstrated its capability for intact tissue imaging with its depth penetration, prolonged focusing range, fast imaging speed, and reasonable axial and lateral resolution [161, 187].

The functional OCT, OCT microangiography (OMAG) uses the intrinsic optical signal from the capillary flow fluctuation to obtain the hemodynamic fluctuation [177, 178, 201] and has shown its potential for myocardial microvascular imaging [142, 186]. Further, ED-capillary velocimetry (ED-velocimetry) is a more advanced method that enables the precise measurement of capillary velocities by statistically analyzing dynamic blood flow fluctuation within the microvascular networks. With Eigen decomposition, fluctuations of the OCT complex signal induced by blood flow motion are decomposed in the eigenspace, which is then used for estimation of the frequency of flow. Experimentally, it has been shown that there is a linear relationship between the estimated frequency and the flow velocity for detecting capillary red blood cell velocity to provide detailed hemodynamic information [115, 179]. Both methods allow for accurately resolving capillary morphology, measuring flow velocity, and understanding the myocardial perfusion property.

In our study, we investigated the dynamics of coronary microcirculation and the myocardial perfusion changes in ex vivo rat heart models that follow infarction reperfusion. This study utilizes ex vivo Langendorff retrograde perfused heart models to investigate capillary velocity. Langendorff models allow for the isolated examination of myocardial function, free from peripheral influences, as an ideal solution for studying ischemia-reperfusion injury without non-cardiac stress or arrhythmias [119, 171]. The infarction events were recreated in rat heart models and imaged using OCT while fixed in the diastole phase and perfused in a Langendorff setup. We utilized both the Eigen Decomposition-based optical microangiography (ED-OMAG) [177, 201] and ED- capillary velocimetry (ED-velocimetry) [178] to visualize the vasculature map and measure capillary velocities simultaneously for investigating the alterations in microvascular structure and microcirculatory perfusion from ischemic heart disease [145, 204]. Both angiographic methods demonstrated the potential of OCTA for understanding the myocardial perfusion change of the

heart microcirculation post-infarction and for developing tissue engineering therapies for restoring proper perfusion and preventing further myocardial injury.

3.2.2 Method

Animal preparation

All animal treatments were approved by the University of Washington IACUC (protocol 2225-04) and followed NIH guidelines. Twelve male Sprague-Dawley rats (250–300 g, N=4 per group) were randomly selected to undergo myocardial infarction surgery, with a 60-minute occlusion and reperfusion of the left anterior descending coronary artery. Anesthesia was provided using intraperitoneal ketamine and xylazine, with postoperative analgesia given via buprenorphine. Four weeks post-ischemia, infarcted hearts were harvested, while control hearts (N=4) were collected without surgery. Hearts were perfused with anticoagulants and fixed with paraformaldehyde before imaging. The hearts were fixed overnight in 4% paraformaldehyde before being rinsed and stored in PBS until imaging. Detailed information can be found in our previous study [145].

Optical coherence tomography imaging system

The swept-source OCT (SSOCT) system utilized a vertical-cavity surface-emitting (VCSEL) swept laser source with a 200 kHz sweeping rate at a central wavelength of 1060 nm and a 100 nm spectral bandwidth[58, 161]. The sampling rate of the k-clock is between 200 and 400 MHz. The a-scan rate is at 200 kHz. The imaging probe was installed with a 5x Thorlabs LSM03 objective lens with a 22 μm lateral resolution. The axial resolution is 10 m, and the roll-off is 6 dB over a 3.75mm range. When tested repeatedly with an a-scan using a mirror, the system's phase stability is roughly 50 mrad. The SNR is approximately 45 dB. In this study, a portable imaging probe was mounted on a translational stage to ensure the imaging plane remained stable and properly aligned with the heart's surface. The stage allowed for three-directional (horizontal, vertical, depth-axis) movement. This setup allows real-time adjustments, which compensates for the out-of-focus issues caused by the heart's inherent curvature.

Optical coherence tomography imaging system

The swept-source OCT (SSOCT) system utilized a vertical-cavity surface-emitting (VCSEL) swept laser source with a 200 kHz sweeping rate at a central wavelength of 1060 nm and a 100 nm spectral bandwidth[58, 161]. The sampling rate of the k-clock is between 200 and 400 MHz. The a-scan rate is at 200 kHz. The imaging probe was installed with a 5x Thorlabs LSM03 objective lens with a 22 μm lateral resolution. The axial resolution is 10 m, and the roll-off is 6 dB over a 3.75mm range. When tested repeatedly with an a-scan using a mirror, the system's phase stability is roughly 50 mrad. The SNR is approximately 45 dB. In this study, a portable imaging probe was mounted on a translational stage to ensure the imaging plane remained stable and properly aligned with the heart's surface. The stage allowed for three-directional (horizontal, vertical, depth-axis) movement. This setup allows real-time adjustments, which compensates for the out-of-focus issues caused by the heart's inherent curvature.

Microscope imaging for the microfluidic channel

A syringe pump was used to perfuse fluorescent beads through multilayer microfluidic channels at flow rates of 0, 5, 10, 20, and 30 μL/min, corresponding to inlet velocities of 0, 0.2, 0.4, 0.6, and 0.9 mm/s. Fluorescent videos were captured using a Nikon TiE Inverted Widefield Fluorescence Microscope, focusing on a 2x2 square section containing the first bifurcation. Bead movement was tracked, and flow rate was calculated by dividing the distance traveled by the elapsed time. The same microfluidic channel was imaged using OCT with 1% intralipid at identical flow rates. OCT scanning covered a 1 mm x 1 mm x 3.75 mm volume. The 3D volume was scanned at 1000 frames per second. The OCTA and ED-velocimetry signals were generated simultaneously, and mean velocities in each branch were averaged using the same regions of interest (ROIs) as the microscope imaging for consistency.

OCTA imaging protocol for ex vivo rat heart

After heart fixation, 1% Intralipid (diluted in PBS) was perfused to the coronary arteries during imaging via retrograde perfusion through an aortic cannula. To avoid sample movement during imaging, a 3-D printed mount was used to hold each heart in the center of a Petri dish. Before imaging, the Intralipid was allowed to flow under the constant pressure of 100 mmHg for 10 minutes, and this pressure was maintained throughout the imaging procedure to ensure consistent microvascular perfusion[142]. A drop of glycerol was injected into the surface of the tissue 10 minutes before imaging as an optical cleaning agent [160, 186]. The scan covers a voxel of 1mm×1mm×1mm. Four locations of interest adjacent to the left anterior descending coronary artery (the area closest to the infarct event) and four remote regions on the heart's posterior side were chosen and scanned for the infarcted hearts. Four locations corresponding to the infarct and remote regions of the infarcted hearts were selected from the healthy heart scans. A co-aligned white-light image (12mm×12mm) and wide-field OCTA (4mm×4mm) were captured simultaneously.

OCTA imaging method

Eigen-decomposed optical microangiography (ED-OMAG) is one of the functional OCTA algorithms that can provide detailed microvasculature projection maps for qualitative or quantitative interpretation. It is a three-dimensional blood vessel visualization algorithm that has been extensively used in imaging applications for [26], brain [54, 115], and skin vasculature[25, 36]. ED-OMAG reconstructs the angiographic information by using an Eigen-decomposed filter to isolate the temporal changes from the static components within the OCT scan [177, 201]. ED-velocimetry builds on ED-OMAG by using an advanced statistical approach to quantify capillary velocity. A detailed description can be found in our previous study [178]. It analyzes the fluctuation frequency in the OCT signal, weighted and averaged with the Eigen spectral energy, to estimate mean capillary velocity. This method provides frequency measurement of capillary flow dynamics and is not impacted by imaging angles like Doppler. The linear relationship between

mean angular frequency from ED-velocimetry and mean velocity from microscope measurement is calibrated for this study by using deliberately designed microfluidic channels (3.11d).

Post-imaging processing and quantifications

To visualize the microvasculature map, we used a method commonly adopted in clinical ophthalmology, where en-face images from 3D scans are often used to measure retinal blood vessel networks. The en-face ED-OMAG microvasculature map was generated from the 3D vascular image using the maximum-intensity projection of flow signals; ED-velocimetry maps were projected from the 3D dataset using the averaged capillary velocity along the depth. Both vessel maps were projected across a 50 μm (10 pixels) slab measured from the tissue surface for further quantification. To measure the effects on the capillaries, vessels that are greater than 20 were removed from the vascular map (3.13e). A detailed description was given in our previous study [186]. From the capillary vascular map, five metrics were quantified from the OCTA vascular map and the velocimetry map combined: the vascular area density, vessel tortuosity index, mean velocity, perfusion index, and capillary transit time heterogeneity. All quantifications were performed and developed in MATLAB (MathWorks, Natick, MA). The vascular area density (VAD) and vessel tortuosity index were quantified from the ED-OMAG vascular map. VAD is calculated from the ratio of pixels occupied by vessels in the binary vessel mask to the total number of pixels in the image[186]. Specifically, a binary vessel mask was generated from the projection image, which was 150×150 pixels in size. The VAD was then determined by dividing the number of vessel pixels by the total number of pixels in the image, providing a measure of the proportion of the image area covered by vessels.

The vessel tortuosity index (VTI) was calculated from the skeletonized vessel map of large vessels [186]. The skeletonized vessels were separated into multiple segments by each node and endpoints for VTI calculation. The VTI value was calculated for each vessel using a simple arc-to-chord ratio method. Finally, the global average VTI from all segments was calculated by averaging the local curve lengths.

Capillary mean velocity, perfusion index, and capillary transit time heterogeneity were quantified from the ED-velocimetry map. The mean capillary velocity was calculated by the average velocity of all capillaries present in the velocimetry map (3.13e). The capillary transit time heterogeneity (CTTH) was calculated from the velocity distribution obtained from all imaging sites within the same area of the same heart. First, a histogram was created to measure the velocity distribution across all the imaging sites. The gamma distribution was fitted to the velocity data in the histogram to model the heterogeneity of the flow speed distribution [137]. The probability density function for the gamma distribution is given by:

$$f(\tau;\alpha,\beta) = \frac{1}{\beta^{\alpha}\Gamma(\alpha)}\tau^{\alpha-1}e^{-\tau/\beta}$$

where τ represents the capillary velocity, α is the shape parameter, β is the scale parameter, and $\Gamma(\alpha)$ is the gamma function. The CTTH is derived from the shape of the constructed gamma distribution and is defined by its standard deviation:

$$\text{CTTH} = \sqrt{\alpha\beta}.$$

The perfusion index was calculated to quantify the microvascular perfusion within the imaging region by integrating the mean velocity with the vascular area (measured in mm^3/s). The multiplication of the mean velocity and vessel area was then summed across the entire image to yield the perfusion index. This estimation assumes the microvascular flow in the healthy heart is consistent and uniform:

$$\text{Perfusion Index} = \int (\text{mean velocity}) \times (\text{vessel area}).$$

Additionally, the perfusion index was compared with the Langendorff inflow perfusion under healthy conditions (3.16a). The Langendorff inflow was obtained by measuring the volume of intralipid perfused through isolated hearts in units of mL/min.

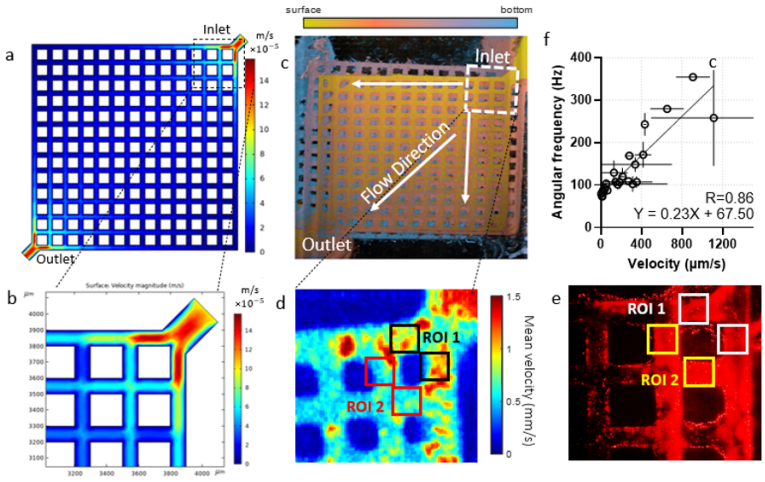

Figure 3.11: Illustration of the microfluidic chip design and the ED-velocimetry calibration result. (a) Design of the microfluidic channel. Velocity distribution was simulated from the shape of the channel network using COMSOL and (b) zoom-in flow distribution of the inlet. (c) Representations of the OCTA of the microfluidic channel showing the design. (d) ED-velocimetry perfused with a 1% Intralipid solution. (e) Microscope images of the microfluidic channels perfused with lectin beads. The white box covers the first branches of the channels, and the yellow boxes cover the second branches. (f) the calibration curve between the frequency measured from velocimetry and microscope based on three different microfluidic channels. All channels was simulated or measured at the perfusion rate of 10 uL/min at the inlet.

To assess the statistical differences between each condition—healthy, ischemic, and remote regions of the hearts—a nested one-way analysis of variance (ANOVA) was conducted to quantify the variations in mean values across the different groups, with statistical significance determined at an alpha level of 0.05. The null hypothesis for the nested one-way ANOVA posits that there is no significant difference in the mean values among the four hearts across the three experimental groups.

3.2.3 Results

Our study utilized a capillary flow phantom to calibrate and validate the capabilities of our ED velocimetry tools for capillary velocity measurements. 3.11a illustrates the design of the microfluidic channel, which branches 12 times in a cross-weave pattern. The flow rate is highest at the inlets of the two proximal branches and is reduced by half in the subsequent second-order branches

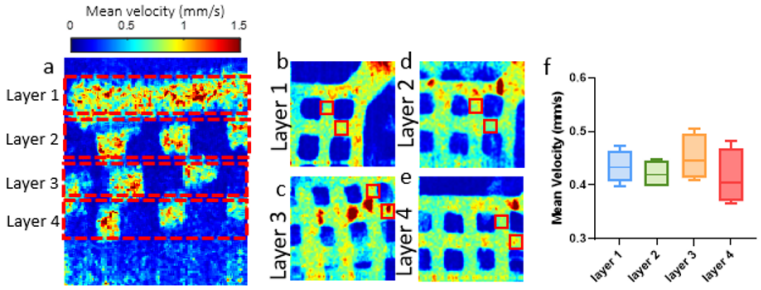

Figure 3.12: Calibration of Microfluidic Device Using Mean Frequency Analysis. (a) Mean frequency map of the microfluidic device, showcasing four distinct layers (Layer 1 to Layer 4). Each layer is outlined by dashed red lines. (b-e) Zoomed-in views of individual layers (Layer 1 to Layer 4) showing detailed frequency distribution. Red boxes indicate regions of interest (ROI) used for quantitative analysis. (f) Box plot of mean velocity (mm/s) for within the ROI. Data shows variation in mean frequency across different layers, with Layer 2 exhibiting the highest mean frequency and Layer 1 the lowest. Color bar in panels (b-e) represents the mean frequency scale from 0 Hz (blue) to 100 Hz (red).

(3.11b). The actual microchannel has four channels overlapping together, sharing the same inlet and outlet, demonstrated by the pseudo-color coding in 3.11c from surface (yellow) to bottom (blue). En-face ED-velocimetry maps and one frame out of the microscope video (3.11d and e) demonstrate the regions of interest (ROI) where flow speeds were measured from the first two primary branches. The velocimetry projection map (3.11d) uses pseudo-color to indicate faster flow in red and slower flow in darker blue. The calibrated linear relationship between the mean frequency (MF) estimated from OCT velocimetry and microscopy measurements (3.11f) validates the feasibility and reliability of the ED velocimetry tools.

The result shown in 3.12 validates the effectiveness of our ED-velocimetry measurement with overlapping microchannels along the depth. The depth-resolved cross-section map (3.12a) shows the four layers of the microfluidic channels. The en face projection from each layer (3.12b to 2e) reveals a slight difference in flow dynamics between each layer due to the variation of the channel morphology, yet most channels show a uniform distribution of flow speed in each branch. The consistent mean velocity observed in the second branch further confirms that the ED-velocimetry measurement accurately measures flow speed regardless of depth or overlapping channels (3.12f).

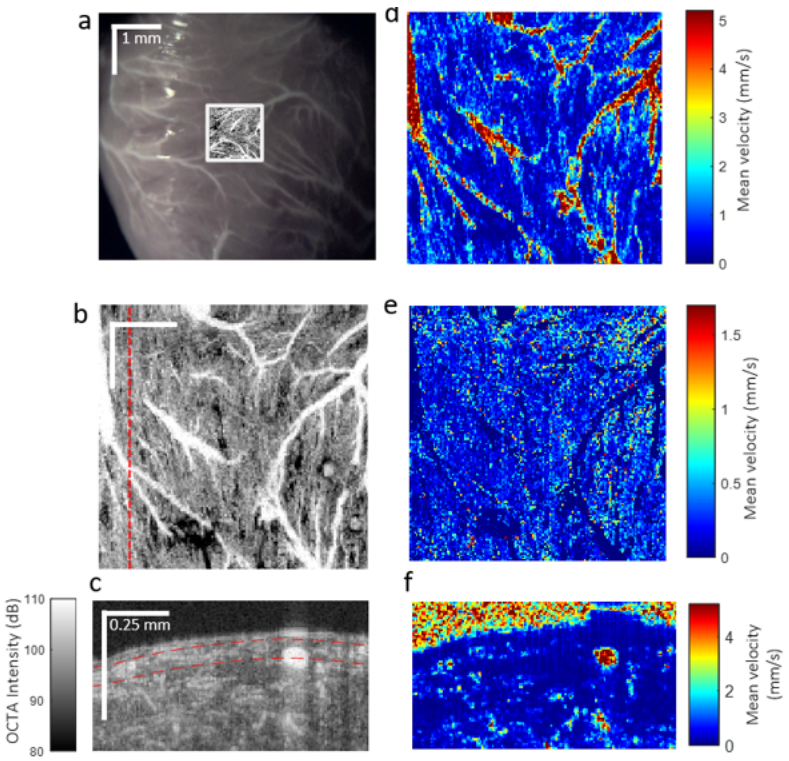

Figure 3.13: Demonstration of the ED-OMAG and Velocimetry map for a healthy rat heart. (a) Representative while a light image overlayed with an en-face OMAG image with matched image size indicating the region of OMAG scans. The scale bar in (a) represents 1 mm. The (b) en-face OMAG image and its (c) cross-section. (e) En-face velocimetry map for the capillary network with the larger vessels removed. Cross-section images (c) of the OMAG and (f) velocimetry scan. The yellow dashed line indicates the location of the cross-section. The scale bar in (b and c) represents 0.25 mm.

3.13 demonstrates en-face OMAG vasculature maps and the associated velocimetry map from a healthy heart. 3.13 b is a traditional OCTA vessel projection map demonstrating the vessel morphology and the same image was stacked on top of the conventional white-light image (3.13a). The capillary was not visible from the white light image. The cross-sectional OMAG and velocimetry images from 3D data sets show the dense capillary and their velocity in deeper tissue layers (Figures 3c and 3f). To evaluate the spatial distribution of the capillary flow, we used a vessel mask to filter larger vessels (3.13e) for the following quantification. From the velocimetry projection maps, heterogeneous flow speeds were observed within different vessels, where larger

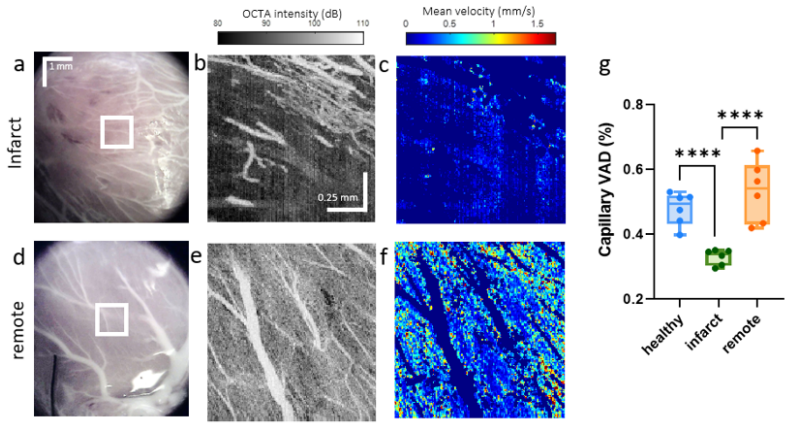

Figure 3.14: Demonstration of the OCTA en face image from infarcted rat hearts. Representative (a, d) white light image, (b, e) en-face ED-OMAG image, and (c, f) en face ED-velocimetry map for the infarcted region, and the remote region, correspondingly. (g) Quantification of the capillary vessel area density (VAD) as a percentage of the total area. Each dot indicates the average VAD measurement from each heart under each condition. ns and **** represent statistical significance of non-significant and $p < 0.0001$, respectively.

vessels distinctly showed higher flow velocities (3.13d), and smaller capillaries showed slower but consistent flow speeds (3.13e).

The same method was also used to demonstrate the microvasculature map and velocity maps for infarct and remote from a post-infarction heart (3.14). Both ED-OMAG and velocimetry projection maps show a significant decline in the capillary distribution (3.14b and c). Contrastingly, no significant difference in the VAD was observed in the remote region of the same infarct heart compared to the healthy hearts (3.14 e-f). The VAD in the infarct region (32.9% ± 2%) is significantly lower compared to the healthy region (47.3% ± 4%) by 30.4% and the remote region (52.9% ± 8%) by 37.8% (3.14g).

The infarct region showed that the capillary's velocity shifted towards a slower flow rate, contrasting with the faster flow speeds observed in the remote and healthy regions (3.15a). The average velocity in the infarct area (0.07 ± 0.03 mm/s) was 72% lower than in the healthy region (0.25 ± 0.09 mm/s) and 50% lower than in the remote region (0.14 ± 0.06 mm/s). We observed a positive correlation between capillary vascular area density (VAD) and mean velocity across healthy,

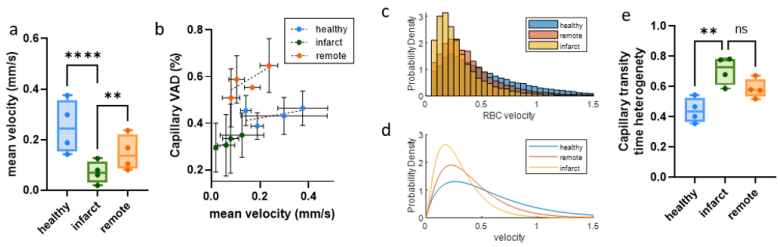

Figure 3.15: Analysis of capillary transit time distribution in infarct and comparison with remote and healthy regions. (a) The mean velocity across three different conditions. (b) Capillary VAD vs mean velocity for three different conditions. (c) Histogram depicting the distribution of Mean velocities measured from one heart to represent the three different conditions. (d) Gamma fitting applied to the histogram distributions. (e) Capillary transit time heterogeneity across the three different conditions. Each dot represents the average measurement of the parameter from each heart. **, ****, and ns represent statistical significance levels of $p<0.01$, $p<0.0001$, and non-significance, respectively.Analysis of capillary transit time distribution in infarct and comparison with remote and healthy regions. (a) The mean velocity across three different conditions. (b) Capillary VAD vs mean velocity for three different conditions. (c) Histogram depicting the distribution of Mean velocities measured from one heart to represent the three different conditions. (d) Gamma fitting applied to the histogram distributions. (e) Capillary transit time heterogeneity across the three different conditions. Each dot represents the average measurement of the parameter from each heart. **, ****, and ns represent statistical significance levels of $p<0.01$, $p<0.0001$, and non-significance, respectively.

infarcted, and remote tissues (3.15b), with healthy tissues displaying higher VAD and higher velocities.

The heterogeneity of velocity distribution in the infarcted region was further calculated using the histogram plots (3.15c). Each histogram represents the combined velocity measurements from the capillaries in four OCT scans of one heart under the same condition. To quantify the hematocrit distribution, a gamma-fitting methodology was employed. 3.15d represents the gamma fitting results applied to the hematocrit distribution. Using this method, we observed a 20.3% increase in the mean capillary transit time heterogeneity in the infarct area (0.71 ± 0.08) compared to the remote region of the infarct heart (0.59 ± 0.03), and a 61.4% increase compared to the healthy region of the healthy heart (0.44 ± 0.06) (3.15e). The results in 3.16 showed the relationship between vascular tortuosity and flow dynamics in healthy, infarcted, and remote regions of heart tissue. The OCTA intensity projection image (3.16a) represents one example of the tortuous vessel structure, with color coding to represent depth. The zoomed-in OCTA image

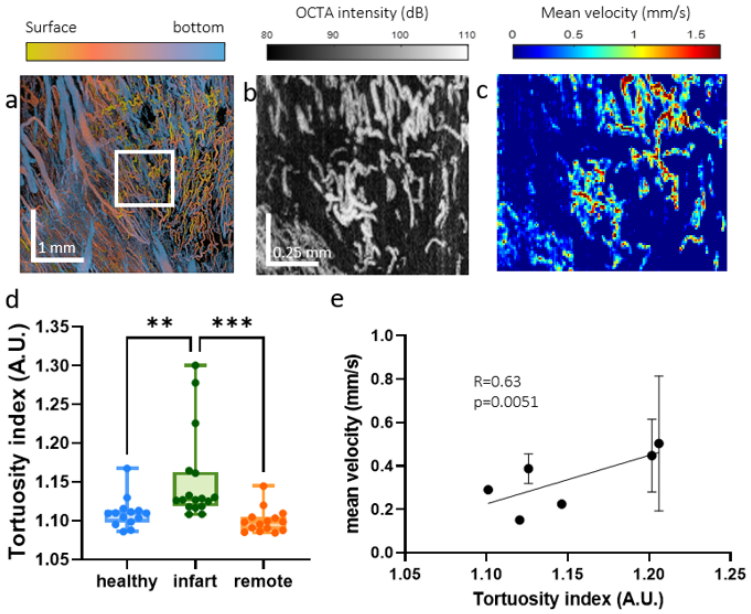

Figure 3.16: Demonstration of Vascular Tortuosity and Flow in Healthy, Infarcted, and Remote Heart Regions. (a) Surface-to-bottom OCTA intensity projection image of heart tissue, with pseudo-color-coding representing depth (surface in yellow/red and bottom in blue). (b) Magnified OCTA image of the region outlined in (a), showing detailed vascular structure. (c) Mean velocity map overlaid on the same region, color-coded from low (blue) to high (red) mean velocity values. (d) Box plot of tortuosity index (arbitrary units) for healthy, infarcted, and remote heart regions. (**$p < 0.01$; ***$p < 0.001$). Each dot represents the average tortuosity index measured from one OCTA scan. (e) Scatter plot depicting the relationship between the tortuosity index and mean velocity (mm/s) across the samples. The linear regression line indicates a positive correlation ($R = 0.63$, $p = 0.0051$). Each dot represents the average of the index measured from each heart.

(3.16b) shows the details of the intricate tortuous vascular network matching the region of ED-velocimetry imaging. The mean velocity map (3.16c) illustrates the spatial distribution of capillary velocity, with higher velocities indicated in red. 3.16d quantitatively compares the tortuosity index across different tissue regions, revealing significantly higher tortuosity in the infarcted area (1.15 ± 0.05), which is on average 3.6% higher than in the healthy region (1.11 ± 0.02) and 4.5% higher than in the remote region (1.10 ± 0.01) ($p < 0.001$).

Furthermore, the scatter plot (3.16e) demonstrates a positive correlation between the tortuosity index and mean velocity ($R = 0.63$, $p = 0.0051$). The results presented in 3.16 demonstrated

the correlation between the perfusion index obtained through the ED-velocimetry technique and whole-heart perfusion measurement measured from the Langendorff perfusion. The scatter plot in 3.16a shows a positive correlation (R=0.8) between the perfusion index and histological measurements (mL/min) measured from the six healthy hearts ($p < 0.051$). Additionally, the bar graph in 3.16b compares the perfusion index across healthy, infarcted, and remote heart regions. The healthy region (599 ± 35 a.u.) exhibits a 79.3% higher perfusion index compared to the infarcted region (334 ± 20 a.u.) and a 61.9% higher perfusion index compared to the remote region (370 ± 25 a.u.). However, there is no significant difference observed between the infarcted and remote regions in the perfusion index.

3.2.4 Discussion

In this study, we demonstrated the potential of using OCT to visualize and characterize myocardial capillary myocardial perfusion degeneration, using ED-OMAG and ED-velocimetry to reflect the impact of ischemic events on the heart. Overall, we have seen significant damage in both the microvasculature morphology and velocity in the myocardial microcirculation post-infarction.

The ischemia-reperfusion injured hearts were used to investigate how changes in the capillary area, morphology, and resistance affect overall circulatory performance and are relevant for understanding the heterogeneity in flow properties and the resulting impaired oxygen extraction efficiency[70, 135, 186]. Since the flow rate is proportional to the capillary size and inversely related to resistance (as described by Poiseuille's law) validated by mathematical and computational simulations, the ex vivo heart can replicate flow disturbances followed by the microfluidic behavior [137]. This model demonstrates how disruptions in myocardial perfusion due to abnormalities at the capillary and microcirculatory levels can impair capillary flow patterns and disrupt circulatory function.

The findings of this study demonstrate a significant reduction in vessel area density (VAD), capillary velocity, and perfusion index in infarcted myocardial tissue. Specifically, a 30.4% decrease in VAD, a 72% reduction in average velocity, and a 79.3% decline in perfusion index were

observed compared to healthy tissue. The positive VAD and mean velocity correlation suggests that capillary density directly influences blood flow efficiency. The reduction in the perfusion-related parameter suggests a substantial impairment in microvascular perfusion in the infarct regions, suggesting the failure to re-establish adequate blood flow to a previously ischemic region of tissue, which could lead to continued tissue ischemia and chronic damage [46].

3.15 employs the gamma-fitting probability method to quantitatively assess changes in capillary velocity distribution by analyzing flow transit time heterogeneity. In 3.15d, the infarcted region shows a broader distribution of flow heterogeneity, with the majority of flow occurring at lower velocities and a long tail extending to higher velocities. This distribution indicates a wider range of capillary flow speeds in the infarcted tissue compared to healthy regions According to Ostergaard et al., the observed decrease in mean velocity in the infarcted region results in longer capillary transit times, which may lead to oxygen shunting. This phenomenon occurs when the flow transit time exceeds the oxygen release time, reducing the efficiency of oxygen off-loading to downstream cardiomyocytes[87, 137]. Consequently, the extended transit time in capillaries can extend oxygen delivery to the myocardial tissue, exacerbating hypoxic conditions and potentially leading to further tissue damage. This finding suggests compromised blood flow dynamics and extended capillary transit time in the infarcted region could exacerbate hypoxic conditions in the downstream myocardial tissue, potentially leading to further myocardial damage [80].

The OCTA vasculature projection images showed increased vessel tortuosity in the infarcted region (3.16a), indicating morphological remodeling of the capillary network as a response to myocardial ischemia. The observed changes in vessel tortuosity are likely a result of vessel enlargement due to increased downstream resistance, as well as compensatory vasodilation mechanisms aimed at maintaining adequate blood flow. These irreversible changes to the circulation system lead to altered flow dynamics, with tortuous vessels often demonstrating higher perfusion rates [123]. The increased resistance downstream causes vessels to dilate in an effort to reduce pressure and facilitate blood flow, which can result in a higher flow rate through these enlarged, tortuous vessels [**g41-g43**]. This compensatory response, although aimed at preserving circulation, can cre-

ate conditions of hyper-perfusion, as indicated by the positive correlation between the tortuosity index and mean velocity (correlation coefficient = 0.63, p = 0.0051) [48, 123, 129]. These findings suggest that while vessel tortuosity represents an adaptive mechanism, it also reflects lasting alterations in the microcirculatory system that may contribute to dysregulated perfusion.

The combination use of en-face OCTA vasculature maps and velocimetry maps effectively provides more information regarding the microvasculature degeneration within the microvasculature of the heart. The strong correlation (R = 0.8) between the perfusion index and the histological perfusion measured in the healthy heart suggests that the OCTA can estimate local tissue and microvascular perfusion in the imaging region (3.16a). The result demonstrated the potential of OCTA perfusion assessments as a non-invasive tool for evaluating microvascular health and detecting perfusion abnormalities in cardiac tissue.

Given the findings of our study, there are several limitations related to the experimental setup that should be acknowledged. The velocity measurements obtained using ED-velocimetry are based on a linear calibration from microfluidic channel models, which do not fully replicate the complexities of capillary flow in biological tissue, particularly the discontinuous passage of red blood cells. Intralipid was used as a contrast agent, but its properties, including smaller particle size, higher density, lower viscosity, and greater scattering, differ significantly from blood. Additionally, the Brownian motion of the intralipid droplets introduces noise and complicates decorrelation estimations. These factors may result in overestimated velocity measurements, requiring cautious interpretation of the data. However, the observed intralipid distribution in infarcted tissue reflects expected disrupted myocardial perfusion patterns, providing useful insights into hemodynamic changes and microvascular alterations in infarcted cardiac tissue.

Second, the study's perfusion setup and fixation of hearts at diastole provide a controlled environment for ex vivo imaging but do not fully replicate the dynamic nature of in vivo heart function, limiting the observation of flow behaviors and microvascular dynamics across the cardiac cycle. Fixing the heart at the diastole restricts the ability to capture perfusion changes throughout different cardiac cycle phases. However, despite this limitation, ex vivo characterization of capil-

laries offers valuable insights by enabling high-resolution imaging of microvascular structures in a controlled setting, free from the complexities of in vivo conditions. This approach is a critical preliminary step, allowing researchers to understand capillary function and flow patterns that could inform future clinical applications. The use of OCTA in this context represents a methodological innovation, and while further study using time-gated or intravital techniques is necessary to capture in vivo microvascular patterns fully, this ex vivo approach provides a foundational basis for developing advanced imaging techniques with potential clinical relevance [4, 96, 109, 113, 156, 171].

Third, the tradeoff between system imaging resolution, focusing range, and field of view also influences the choice of imaging lenses. The use of the LSM02 was chosen for a reasonable balance for its long focusing range, which helps to minimize the effect of the heart's curvature and ensure the imaged region remains in focus. However, the resolution of the OCT system fell short of resolving the details at the capillary level. To resolve individual capillaries, a 10x lens can be used, and the issue of capillaries going out of focus due to the heart's curvature can be addressed with a tunable lens [114, 124]. Although the resolution is insufficient to resolve individual capillaries and interpapillary distances fully, the ED-based statistical method captures the overall fluctuations of the intralipid. The fluctuation correlates with the larger-scale variations in blood flow characteristics within the entire infarcted tissue, providing a reasonable estimation of the infarcted hemodynamic properties that align with histological evidence.

In conclusion, this study demonstrated the capability of OMAG and ED-velocimetry to quantify changes in myocardial capillary perfusion post-infarction, demonstrating significant reductions in vessel area density, capillary velocity, and perfusion index. These findings indicate microvascular degeneration and flow disturbances in response to ischemic injury, providing insights into the relationship between capillary structure and impaired perfusion. The increased capillary transit time and vessel tortuosity further suggest a role in continued myocardial damage. This study builds a foundation for future research to translate these findings into in vivo settings, with the application of time-gated registration methods or intravital techniques that could capture dy-

namic perfusion patterns across the cardiac cycle. Moreover, the application of OCTA and ED-velocimetry has demonstrated its capability to assess myocardial perfusion characteristics and therapeutic strategies, especially for tissue engineering for assessing microvascular health in ischemic heart disease.

4 Optical Coherence Tomography Angiography Measures Blood Pulsatile Waveforms at Variable Tissue Depths

As discussed in previous chapters, Optical Coherence Tomography (OCT) and its angiographic extension, OCT Angiography (OCTA), have demonstrated significant potential in providing high-resolution, non-invasive imaging of microvascular networks and blood flow dynamics. While much of the focus has been on applications in cardiac and dermatological imaging, this chapter extends the utility of OCTA to explore its ability to detect pulsatile waveforms within skin microvascular plexuses, an area of clinical interest traditionally dominated by Photoplethysmography (PPG).

PPG is routinely used to detect the blood pulse signal from skin tissue beds in clinics. However, the origin of the PPG signal remains controversial. This study aims to explore OCTA to indicate pulsatile waveforms in the papillary plexus and dermal plexus separately under different hand elevations. From the 3D OCTA signals, depth-resolved pulsatile blood flow signals were extracted from different skin vascular plexus. The systolic amplitude, crest time, and delta T were measured from the OCTA pulsatile signals when the hand was placed at the positions of 50 cm below, 0 cm, and 50 cm above the heart level.

The pulse signal integrated from all the depths is more consistent and has a similar waveform to that of the PPG. The pulsatile patterns from the papillary plexus and dermal plexus showed distinct morphological changes at different local blood pressures. Less amplitude difference was found from papillary plexus comparing to that of the dermal plexus. Crest time was found in an increasing trend in the OCTA pulsatile waveform from both plexuses when the arm was raised from the position below to above the heart level. In contrast, a decreasing trend of Delta T was detected in the dermal pulsatile but was not observed from that of the papillary plexus, indicating that vascular resistance associated with the arm elevations does not necessarily have the same effect on the two plexuses. This study demonstrated that OCTA can provide depth-resolved pulsatile waveforms within different microvascular plexus within tissue skin beds. This technique could open doors to understanding the mechanisms of how blood flow changes at different skin circulatory plexus.

4.1 Introduction

Photoplethysmography (PPG) is a non-invasive optical technique that is often used to measure the pulsatility of cutaneous blood flow by detecting subtle variations in tissue blood volume through light absorption [21]. PPG signal is composed of a slowly varying DC signal associated with non-pulsatile blood, tissue and bone, and a pulsatile AC waveform that is related to the increase/decrease of blood volume within tissue beds due to each heartbeat. The AC component of the waveform rises during the systolic phase and falls during the diastolic phase, periodically following the same trend as the blood volume change during systolic and diastolic phases of each heartbeat.

PPG signal could be interpreted as a summation of the forward propagation wave generated by vessel contraction and the backward reflective wave generated by vessel relaxation from the periphery [152]. The backward reflective wave is induced as blood travels through the vascular tree and being reflected by the bifurcated vessels or the elastic arterial vessel walls. As pulsatile blood propagates from the central arteries to the periphery vessels, the increased resistance in peripheral vessels would induce more reflection waves. The alternation in the PPG waveform has been

reported to associate with aging or disease processes such as hypertension, diabetes, atherosclerosis, and large vessel stiffening [21], [7], [126]. Although extensive research and application of PPG have shown potential in evaluating the cardiovascular system [131]–[75], hitherto, the origin of the PPG waveform, however, remains elusive and controversial.

Optical coherence tomography (OCT) based angiography (OCTA) has demonstrated the capability to visualize cutaneous blood flow with depth-resolved information and in high resolution [169]–[198]. Blood flow information can be isolated from the static tissue utilizing a motion contrast algorithm, optical microangiography (OMAG), based on an eigen decomposition (ED) approach [198]–[174]. The high imaging resolution from OCT allows the technique to distinguish small blood vessels within capillary beds from relatively large blood vessels at deeper depth locations. The light source of the OCT system is operated at near-infrared wavelength, which is similar to the typical 940 nm PPG light source giving a similar penetration depth and functionality. In particular, ED-OMAG contrasts the moving blood flow with a signal strength proportional to the blood cell flux, i.e., the volume of red blood cells passing through vessel cross-section per unit area [196], [195]. Volumetric flux is in proportion to the volume change and is suggested to be affected by similar vascular mechanisms [105]. Therefore, it would be reasonable to compare the pulsatile blood flows measured by the two technologies. Moreover, benefiting from the depth-resolved imaging, OCTA has the capability to separate pulsatile information from different cutaneous circulatory plexuses. Thus, this capability would provide us with an opportunity to extract and compare the property of blood flow pulsations from both the papillary and dermal plexuses simultaneously.

In this paper, we report a new method that uses the OCTA signals to provide reliable depth-resolved pulsatile blood waveforms within tissue beds. It was suggested that the PPG signal might be associated with arteriole blood pressure not only due to its similarity in waveform but also because of its proportional relationship between arterial blood pressure and blood volume [22], [147]. Similar to the strategy used in PPG studies [35]–[24], we have conducted a hand-raising experiment to understand better how local blood pressure and peripheral resistance affects the mor-

phology of pulse waveforms in the different cutaneous circulatory plexuses. The force of gravity could significantly alter local blood pressure and peripheral blood flow resistance due to cutaneous vessel autoregulation adjustment [35]. When the hand is below the heart level, the increased capillary pressure will induce vasoconstriction of the arterioles, resulting in increased pre-capillary flow resistance and decreased post-capillary flow resistance. Conversely, when the hand is elevated, the decreased capillary pressure would induce arteriole to dilate, resulting in a decrease of pre-capillary flow resistance and increase of post-capillary flow resistance [133]. Such a simple experimental strategy has been utilized by various research groups when developing PPG, Camera-based PPG, laser doppler flowmetry, etc. [79]–[94] to test the validity of the measurements by examining the change in flow resistance at different blood pressures. However, no technique can observe variation in the pulsatile waveform from different circulatory plexus under the effect of hand elevation. Thus, this study could provide valuable clues for understanding the mechanical property of how blood travels through different types of vasculature networks under the effect of flow resistance and elucidate its potential applications in disease assessments.

4.2 Method

The OCTA pulsatile signals were measured in five young, healthy volunteers (n=5; 3 males, two females). We used a hand-held swept-source OCT (SS-OCT) system [162] to collect OCTA signals from fingers in human subjects to represent pulsatile blood waveforms within skin tissue beds. This system employed a 200kHz swept light source operated at a central wavelength of 1310 nm and a spectral bandwidth of 100 nm, providing $\tilde{8}$ μm axial resolution. A laboratory-built transmission mode PPG device was also used to collect the PPG signals from the finger to indicate blood volume changes for reference. The imaging of subjects reported in this study using a laboratory-built investigational device was conducted in accordance with a protocol approved by the Institutional Review Board of the University of Washington, and informed consent was obtained from all subjects. The study followed the tenets of the Declaration of Helsinki and was conducted in compliance with the Health Insurance Portability and Accountability Act.

In this study, OCT datasets were acquired on the index finger at three different hand elevation: above (+50 cm), same (0 cm), and below (-50 cm) heart level (5.1A). The data was collected in a sitting position, with regular breathing and minimal body movement. The OCT hand-held probe was placed on an adjustable hand rest. The height of the chair was adjusted so that the hand could be leveled with the vertical mid-point of the sternum when placed on the probe, which was approximately the level of the heart. The probe could be adjusted to allow the hand placed below or above the heart level, or to form a 45-degree angle between the trunk and arm to avoid building unnecessary tension or stress on the arm. PPG signal was collected from the middle finger on the same hand. We avoided measurement sites that may contain large arteries and asked the volunteer to keep the finger still with minimal pressure applied to the detector to eliminate motion artifacts caused by tissue deformation. Before data collection, the volunteers were asked to rest for at least 5 minutes to accommodate the environment. Measurements were captured in a quiet and controlled room temperature environment at the same hour each day. Two scanning protocols were designed in this study. The first protocol was designed to provide 3D OCT structural and OCTA blood flow images of scanned tissue volume, in which the scans contained 1000 × 5 B-frames (i.e., 1000 scan locations with each position having five repeated B-scans), and each B-frame was composed of 1000 A-scans. The field of view was 2.5 × 2.5 mm^2. The resulted 3D images (5.1 C) were used to guide the depth selection of the cutaneous plexus for the extraction of pulse waveforms. Since the cutaneous vessels consist of horizontal microvascular networks with interweaved arteriole and venules from which the nutritive capillary bed arises, the two plexuses can be separated based on their relative depth and vessel structure from the 3D microvasculature image (Figure.1B and E) [41].

The second protocol was designed to extract pulsatile waveforms from OCTA signals, in which 4000 repeated B-scans were continuously collected at one same position over a period of ĩ0 sec (5.1D). The B-scan consisted of 300 A-scans (covering 1.0 mm), which led to an imaging rate at 400 frames per second, providing sufficient temporal resolution to observe pulsatile blood flow signals.

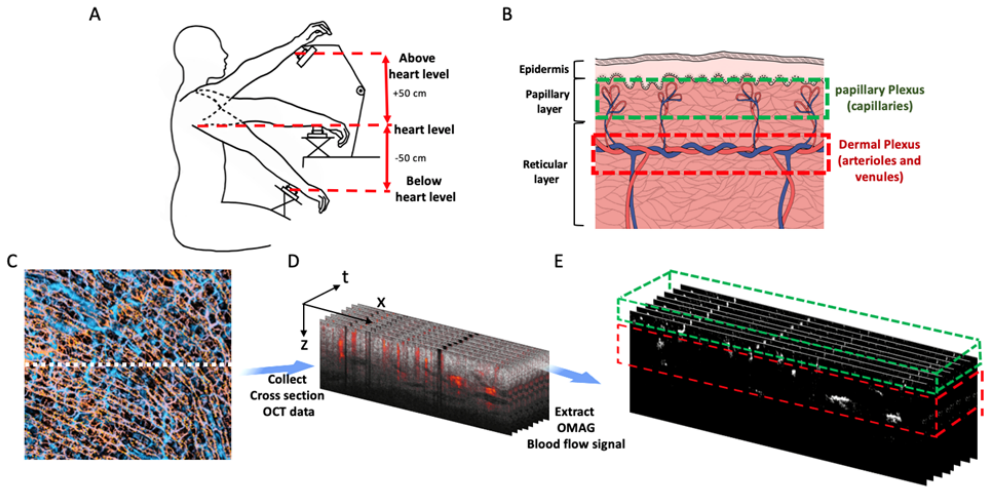

Figure 4.1: Schematic of the experimental design. (A) The set-up of the collection procedure at different hand elevations. The heights of the hand relative to the heart were +50 cm, 0 cm, -50cm, respectively. (B) The relationship between the papillary plexus (capillary bed) and the dermal plexus (arteriole and venous). (C) Representative 3D OCTA microvascular image color-coded by depth information, where orange indicates the papillary capillary vessel networks and blue, indicates the dermal plexus. (D) Time series of repeated OCT scans at the position shown as a dashed line in (C), from which (E) OCTA blood flow signals were extracted. The green dotted box is an illustration of the tissue layer that contains the papillary plexus. The red dotted box is an illustration of the tissue layer that contains the dermal plexus.

All signals were processed and analyzed retrospectively in MATLAB (The MathWorks, Inc., USA). 3D OCTA blood flow image was generated by the OMAG algorithm using an eigen decomposition (ED) approach (5.1C). OMAG contrasts the movement of blood flow from the static tissues by comparing 5 repeated B-frames. The well-known projection artifacts within OCTA blood flow images were removed using an algorithm previously published in [207], [208]. From the 3D OCTA images, we identified approximate depths for proper segmentation of papillary capillary plexus (1̃00 – 300 µm from the skin surface) and dermal plexus (3̃00 – 1500 µm from the skin surface) for the time series of B-scans to evaluate the pulse waveforms (5.1E).

Time series OCTA images were obtained from the repeated B-scans using moving 5 repeated B-scans (Figure D). We assumed the pulse signal from the papillary dermis layer was from the capillary bed, and the pulse signals from the dermal plexus were primarily from the arterioles where

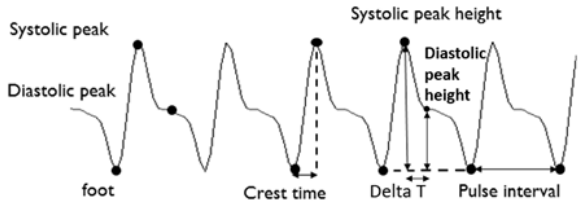

Figure 4.2: Morphology parameters used to assess the pulse waveforms in this study.

the pulsation in the venules could be omitted [106]. The pulse signal from each microvascular plexus was obtained by integrating the intensity signals, *I(t)*, within the region of interest from the temporal OCTA blood flow images, *OCTA(x,y,t)*, and was plotted in a temporal relationship.

$$I(t) = \iint \mathrm{OCTA}(x, y, t)\, dx\, dy \tag{4.1}$$

Where *x* and *y* indicate the pixel indices in the OCTA image. The pulse signal was also measured by integrating the OCTA signals from both plexuses (papillary plexus and dermal plexus). The obtained time-varying signal was then passed through a designed bandpass finite-duration impulse response (FIR) Equiripple filter (0.7-10 Hz) with 40dB attenuation in the stopbands, to obtain the final pulse waveform.

The repeatability of the measured pulse waveforms was assessed by calculating their coefficients of variance. In this test, we conducted five imaging sessions at the same skin position to each collect 10-second temporal OCTA scans where each imaging session was resumed by re-positioning the finger under the OCT probe after the prior session. The resulted pulse waveforms were analyzed for their amplitude and peak to peak interval to demonstrate the repeatability of the technique.

To characterize the OCTA pulsatile waveforms, we followed the convention that is often used in the field of PPG (5.2). The systolic peaks of each pulsatile waveform were found by an adaptive peak finder algorithm implemented in MATLAB (Findpeaks). The systolic foot and diastolic peaks were obtained by the local maximum of the second derivatives. Three parameters (AC amplitude, crest time, and delta T) were measured from the OCTA pulsatile waveform for the assessment of its morphology (5.2). The AC amplitude was measured by the difference in amplitude

between the systolic peak and foot of the waveform. Crest time was measured by the time interval between the foot and systolic peak. This parameter indicates the flow resistance in the forward wave. Delta T was measured by the time interval between the systolic and diastolic peaks. It is associated with a relationship between the forward and reflected waves, which often indicates the peripheral flow resistance. For ease of comparison, the AC amplitude from all plexus was normalized to the geometric mean of the AC amplitudes from all plexus pulsatile measured at heart level. The AC amplitude from the papillary and dermal plexus was normalized to the geometric mean of the AC amplitudes from the dermal plexus at the heart level. The time differences in the morphological values were normalized to the pulse interval of each heartbeat accordingly to eliminate individual differences.

To compare the change in morphologies related to the hand positions, the geometric mean of the morphological variables, and the 95% confidence interval (± 95% CI) were calculated. A one-way ANOVA was used to test for the significance of the difference in mean of the morphological values measured from all plexus. Two-way ANOVA was used to test for the significance of the difference in the mean of the morphological values measured from the papillary plexus and dermal plexus.

4.3 Result

5.3 shows the representative time series of OCTA blood flow and OCT structural signals from the index finger at the heart level (h = 0 cm). In this example, the OCTA blood flow intensity signals (Figs 3A and 3B) showed cycling periods at 0.8 Hz that matched well with that measured by a heart rate monitor. Strong spectral power was observed at the harmonic frequencies produced by Fourier transformation, which usually contains the most biological signals (Fig 3B). A weaker periodical signal was found in the OCT structural signal, which included signals from the blood flow and static tissues (Figs 3C and 3D). The change in temporal intensity signals from the OCTA image (Fig 3E) indicates that blood flow in all vessels spikes with each heartbeat and gradually decays. The repeatability study showed that the coefficients of variance of the amplitude and pulse

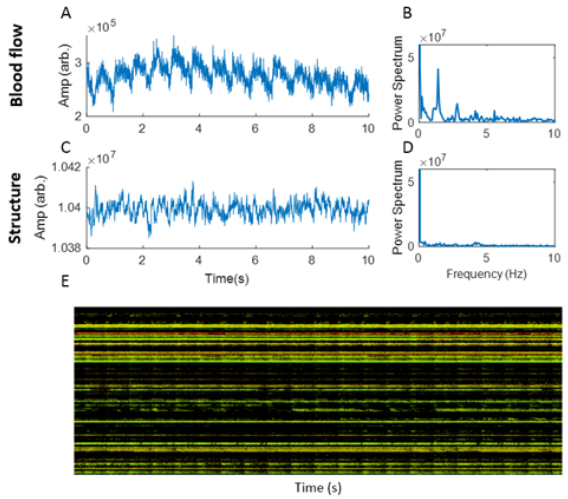

Figure 4.3: Illustration of intensity signal and power spectrum from the OCT structure and OCTA blood flow signals. The temporal intensity signal from (A) OCTA blood flow image, and (C) the OCT structure image. The spectra in (B) and (D) show the frequency power of (A) and (C) correspondingly (FFT). (E) temporal A-scan image extracted from 15-sec repeated B-scans, showing the consistent changes in blood volume of all vessel plexus corresponding to each heartbeat.

interval were around 5%, demonstrating that the OCTA measurement of blood pulse signals is repeatable (Table 1).

Table 4.1: Coefficient of variation of the pulse transit time and heart rate calculated from the processed waveform

	Pulsatile Amplitude (CV)	**Peak to Peak Interval (CV)**
Papillary	3.22%	4.71%
Dermal	1.34%	5.00%
All Plexus	1.47%	5.09%

5.4 illustrates the morphological difference of the representative OCTA pulsatile signals from all plexus (i.e., the integration of all blood flow signals) comparing to PPG pulsatile signals at three hand elevations. It is observed that the diastolic peak was more noticeable when the hand was below the heart level and was less distinguishable from the systolic peak when the hand was above the heart level, consistent with the previous observations described by the PPG measurement [78].

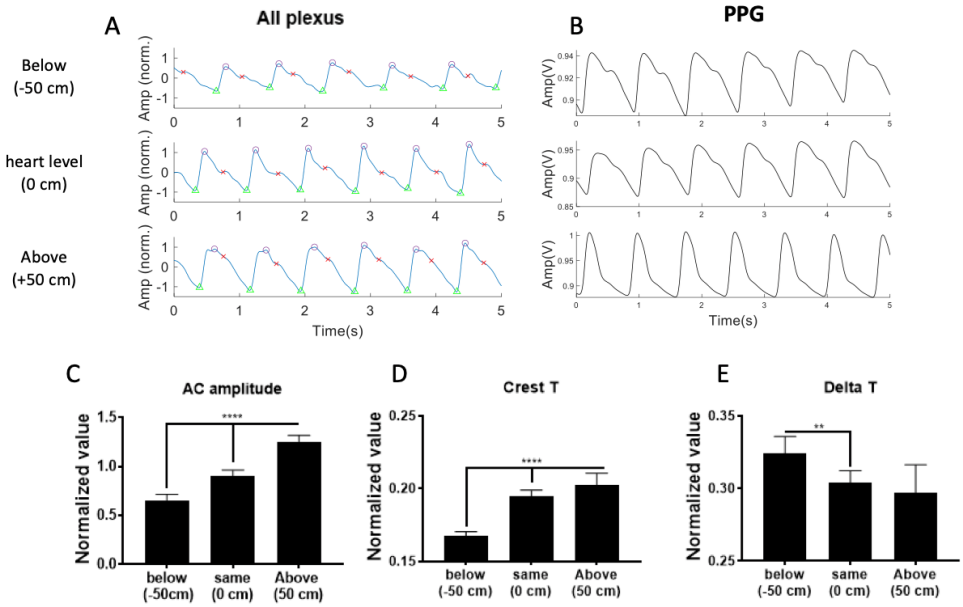

Figure 4.4: 5-second demonstration of the pulsatile waveform from all plexus collected by (A) OCTA and (B) PPG when the hand is below heart level (-50 cm), at heart level (0cm), and above heart level (+50 cm). (C-E) Geometric mean (± 95% CI) of the morphological variables of AC amplitude (C), crest time (D) and delta T (E) from the OCTA pulsatile waveform form. ** indicates $p<0.001$, **** indicates $p<0.0001$

The normalized mean AC amplitude of the pulsatile waveform in all plexus changed in conformity with the position of the hand relative to the heart (5.4C). Mean AC pulsation was the lowest when the hand was below the heart (h= -50 cm) and showed a trend of increase as the hand elevated. Normalized mean crest time and delta T were found significantly different at different hand positions relative to the heart (5.4D). Crest time showed an increasing trend, and delta T showed a decreasing trend when the hand was raised from below heart level (h = -50 cm) to above heart level (h = +50 cm). These observations are consistent with the results observed in the PPG study [78].

5.5 demonstrates the differences in morphology of the pulsatile waveforms from the papillary plexus (5.5A) and dermal plexus (5.5B) at different hand elevations. Similar to the results observed from all plexus (5.4), AC pulsation in dermal plexus showed an increasing trend when the

hand was changed to an elevated position (5.5C). AC pulsation was the greatest in the papillary plexus when the hand was at the heart level, whereas it was decreased when the hand was above or below the heart level. A significant difference in AC pulsation was found between the dermal and papillary pulsatile when the hand was above the heart level (h = +50 cm), whereas no difference was found in the AC pulsation between the papillary plexus and dermal plexus pulsatile when the hand was at heart level and below heart level (5.5C). Approximately, a two-fold difference was found in the AC pulsation from the dermal plexus compared to that of papillary plexus. A longer crest time was observed in both papillary and dermal pulsatile when the hand was elevated (Fig 5D), similar to that of all plexus. Dermal pulsatility showed a decreased trend in delta T as the hand was raised to above the heart level (5.5E). No difference in delta T was observed in the papillary pulsatility at different hand elevations.

4.4 Discussion and Conclusion

In this study, pulsatile signals in the cutaneous circulatory system were successfully extracted with the support of OCTA through an Eigen-decomposition based OMAG approach. The results demonstrated the potential of how OCTA could become a reliable, non-invasive imaging tool measuring the pulsatile waveforms. Although PPG detects the changes based on the light absorption by blood volume, and OCTA detect the changes of the backscattering light due to the difference in the blood volume. We found that OCTA pulsatile waveform has similar morphological changes to the PPG signals at different hand elevations [78] since they are both describing the property of blood volume change between each heartbeat. The PPG AC signal relies on the volumetric change in the cutaneous vessels. In contrast, OCTA gave a measurement that is proportional to the volumetric flux that is associated with the number of red blood cells passed through vessels. The volumetric flux change is driven by the same fluid dynamic mechanism of the source of the AC PPG signal.

Similar to the PPG results reported by Hickey et al. [78] we observed a consistent increase of the AC pulsation derived by integrating all OCTA signals across all plexuses when the hand was

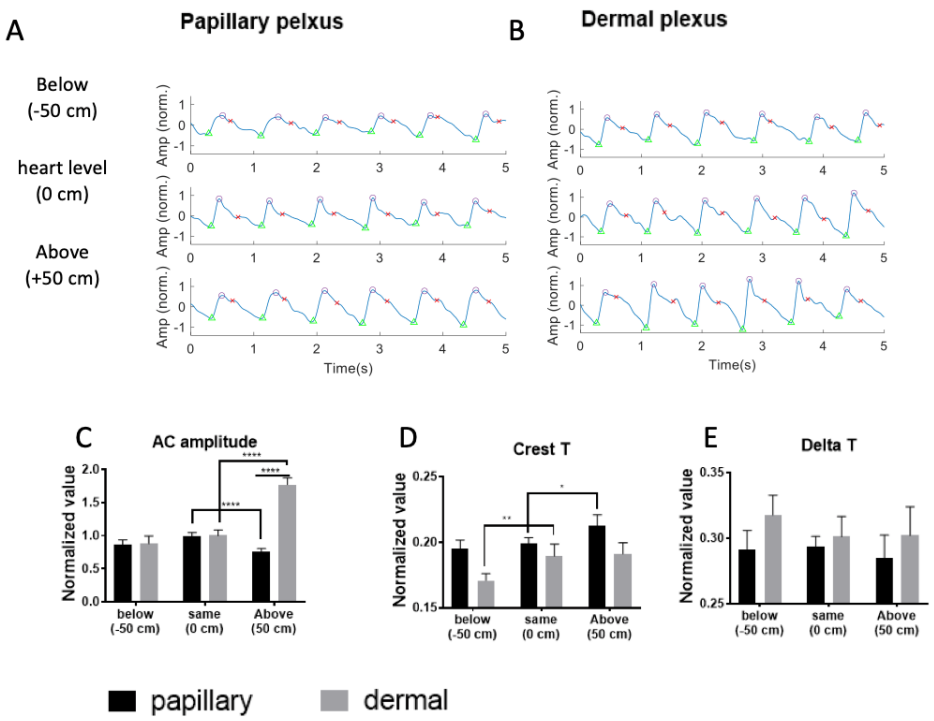

Figure 4.5: 5-second demonstration of the pulsatile waveform from (A) the papillary plexus, and (B) dermal plexus when the hand is below heart level (-50 cm), at heart level (0cm), and above heart level (+50 cm). (C-E) Geometric mean (± 95% CI) of the morphological variables of AC amplitude (C), crest time (D) and delta T (E) from the OCTA pulsatile waveform form from each plexus. * indicates p<0.05, ** indicates p<0.001, **** indicates p<0.0001

raised from below heart level to above heart level. The change of AC pulsation is associated with a change in pulsating blood volume in the cutaneous vessels due to the venoarterial reflex (VAR) [35], [79], [88]. Autoregulation in the arterioles adjusts the blood vessel diameter in response to the disruption in blood flow and perfusion pressure in the venues. When the hand is above the heart level, the hydrostatic effect would cause the venous wall to collapse due to a drop in venous pressure. This effect may cause vasodilation in the arterioles, so that blood volume in the arteriole would increase. When the hand is below the heart level, venous vessels would distend, causing vasoconstriction in the arteriole.

AC pulsation from the papillary plexus and dermal plexus is regulated by the VAR at different hand elevations [35]. But the AC pulsation across the plexus may have a distinct trend due to the difference in the vessel function and mechanical properties. However, due to the nature of its working principle, PPG is not able to track the change in volume trend from the dermal plexus and papillary plexus separately [112].

Consistently, we observed the similar trend in the OCTA pulsatile directly measured from dermal plexus at changing hand elevations. In contrast, a distinct pattern was detected from papillary AC amplitude, which may be induced by the change in pre-capillary blood pressure. When the hand is at heart level and below heart level, the same volume of pulsating blood might be delivered across the plexuses indicated by the same AC amplitude observed from both plexuses. When the hand is above the heart level, reduced pre-capillary blood pressure may lead to a reduction of the number of red blood cells being pushed into capillary vessels so that a decrease in AC pulsation is detected [35].

Crest time, which is the time difference between the foot of the pulsatile signal and the systolic peak, measures the time used for the rapid injection of blood during the systolic phase. Based on previous studies, an increase in crest time is associated with increased blood flow resistance, aging, or disease relative vascular changes [28]–[185]. Increased blood flow resistance would delay the systolic phase. The trend of increasing crest time from all plexus detected by both PPG and OCTA may indicate that there could be an increase in blood flow resistance as the hand changed from below heart level to above heart level. The same trend was observed in the OCTA pulsatile signal detected from both the papillary and dermal plexus, indicating that flow resistance has the same influence on both plexuses. When the hand is changed into an elevated position, vasoconstrictions in the arteriole may cause increased resistance resulted in an increasing trend in Crest time and vice versa [45]. Capillary blood flow resistance is proportional to systemic hematocrit as red blood cells being pushed into the bifurcated small capillary vessels. Hand elevation may induce a drop in local blood pressure that induces flow resistance indicated by a decreased crest time.

When the incident pulse wave moves from the heart to the peripheral vessels, it would come across an impedance mismatch at vessel junctions and in small vessels that have high resistance [152]. The impedance would influence the incoming blood flow generating a reflected pressure wave, which is observed as the diastolic peak. Delta T, which is the time interval between the systolic peak and diastolic peak, measures the time taken for the reflective wave from heart and back. The trend of decrease in Delta T may be associated with the increased vascular tone, and high pulse wave velocity occurred in the arteriole [78]. Both PPG and OCTA pulsatile waveforms showed a decreasing trend in delta T as the hand was elevated above the heart. However, the same pattern was detected in the dermal pulsatile but was not observed from that of the papillary plexus, indicating that the vascular tone and wave velocity did not change in the capillary beds.

However, some morphology values were not significant when comparing under the condition of different hand elevations. A couple of factors may induce high variation or noise. First, the number of subjects tested in this study was limited. Even though geometric mean was used to indicate the central tendency of the set of values, an insufficient sample size would limit the potential to detect significant differences. A large cohort of subject study is warranted to increase the statistical power for the current study. Second, the intensity signal measured at different sites could be profoundly affected by local factors, including microvasculature density, local blood flow activity, skin melanin, epidermal thickness, and so on [127].

In conclusion, we have demonstrated that OCTA is capable of generating pulse waveforms of the blood volume change within the superficial skin tissue beds up to 1.5 mm in depth. OCTA pulsatile waveforms showed similar morphological trend to that of the PPG studies at three different hand elevations. Benefiting from the depth-resolved information, we have found that the trend of change in AC amplitude and delta T behaves differently in the papillary and dermal pulsatility. The pattern of pulsatile morphology change follows the physical properties of the VAR effect, which are due to vessel autoregulation adjustments, pre-capillary blood flow resistance and pressure, and peripheral blood vessel reflectance. This technique may open doors for understanding the mechanisms of how blood flow in different cutaneous plexuses responds to the VAR effect

based on the changes in volumetric flux in blood vessels associated with the number of red blood cells. We expect that it could also be developed for blood pressure measurement, disease assessment, and risk stratification, or health condition of the individual's blood vessel or heart chamber indication.

5 Non-Invasive Characterization of Skin Microstructure and Microvasculature Using OCT Imaging

Functional OCT provides highly sensitive information, allowing early detection and assessment at pre-disease stages to prevent health conditions escalate.

While functional OCT has already proven invaluable in ophthalmology for retinal and corneal imaging, its expansion into dermatology offers unique opportunities to address the limitations of conventional diagnostic methods. This chapter focuses on OCT's application in dermatology, building on its high-resolution capabilities and functional imaging potential highlighted previously.

In dermatology, traditional diagnostic techniques, such as excisional biopsies, remain the gold standard for cellular analysis but are invasive and often impractical for repeated follow-up studies. High-frequency sonography, though widely used, falls short in resolution and contrast for detailed skin imaging. By leveraging the principles of Michelson interferometry and advancements in light-based imaging, OCT provides a non-invasive alternative capable of capturing microscale tissue structures, offering significant diagnostic and monitoring advantages.

Unlike the eye, where OCT imaging benefits from naturally low scattering and high transparency, skin presents distinct challenges due to its opacity and high scattering properties. Building on the principles discussed in earlier chapters, this section explores how OCT utilizes the "diagnostic window" in the 700-1300 nm wavelength range to penetrate deeper into the skin, enabling visualization of tissue inhomogeneities. However, scattering events, absorption by melanin and hemoglobin, and refractive index variations introduce artifacts that must be managed to achieve accurate imaging. Technological advancements, such as systems with high output power and dynamic range, play a crucial role in isolating directly reflected photons that carry critical image information.

Building on the advancements in OCT imaging techniques discussed earlier, this chapter delves into its role in dermatology for detecting skin abnormalities and evaluating suspicious lesions. While dermoscopy combined with biopsy remains the standard for skin lesion evaluation, OCT offers the potential to visualize tissue structures non-invasively, enhancing diagnostic capacity while avoiding the drawbacks of traditional methods. Additionally, functional OCT techniques, as previously introduced, have the potential to expand OCT's accuracy and utility in diagnosing specific conditions, including skin cancer.

The imaging contrast in OCT arises from the backscatter of light as it interacts with structures of varying optical densities. This principle, introduced in earlier discussions, enables OCT to provide both diagnostic and therapeutic insights. For diagnostic applications, OCT leverages tissue optical properties to assess depth-resolved structures, while for therapeutic purposes, it predicts light distribution and energy deposition for treatment planning. By integrating tissue optical properties into light transport models, OCT enables more precise predictions of light behavior, supporting its diagnostic and therapeutic roles in dermatology.

This chapter builds on the foundational modalities of OCT introduced earlier, extending its application to dermatology and emphasizing its ability to provide non-invasive assessments of skin structure and cutaneous capillaries.

5.1 Investigation of the effect of compression pressure in contact OCT imaging on the measurement of epidermis thickness

Optical coherence tomography (OCT) is a noninvasive 3D imaging technique that offers significant advantages over traditional microscopy and biopsy in measuring epidermal thickness (ET) when assessing skin conditions. However, OCT imagining is often required to be in contact mode to mitigate subject movement and uneven skin geometry. It is, however, not known whether the contact would affect the ability of ET measurements. In this study, we investigate the relationship between contact pressure applied during skin imaging and the accuracy of ET measurements. By monitoring real-time pressure on the contact probe, we observed progressive deformation in the epidermis with increased compression forces. We observed a notable decrease of up to 13% ET measurement and a 100% decrease in capillary vessels with contact pressure at 69kPa. We also observed different deformation properties in scar tissue compared to nearby healthy tissue. Our study demonstrated the importance of controlled pressure in contact imaging in dermatology assessment, which is often neglected.

5.1.1 Introduction

Because the epidermis acts as the outermost barrier for protection, immune defense, sensory, and thermoregulation, its proper and accurate measurement has become one of the important biomarkers in the assessment of skin conditions, such as burn injuries [122], [71], inflammation [155], [182], dermatological disorders [203], [39], [89], [1], and cosmetic-related research [53], [101], [111], [34], [149]. Subtle variations in the epidermis can signal the skin's resilience or vulnerability to environmental factors (UV radiation), aging, and skin cancer [1]. Compared to optical microscopy (skin biopsy), optical coherence tomography (OCT) is an optical imaging method with micron-level resolution and the added benefits of millimeter-level penetration depth without invasive biopsy. OCT can provide depth-resolved cross-section images, which could serve as an ideal

tool for precise assessments of the superficial skin layers: stratum corneum, epidermis, and dermis [122], [182], [203], [148], [13], [67]. The epidermis can be segmented from the dermis through the dermal-epidermal junction (DEJ) based on the difference in intrinsic optical properties and tissue architecture between these two skin layers. The utility of observing a subtle change in epidermis thickness with OCT has been demonstrated for disease assessment, for example, skin carcinoma [148], [60] and scleroderma [1] These features make OCT a valuable tool for qualitative and quantitative assessment of subtle changes in epidermal thickness. Additionally, the functional OCT, OCT angiography, enables the simultaneous assessment of the vasculature within skin tissue beds without a need for a contrasting agent while at the same time providing the measurement of epidermal thickness[144], [52], [84]. Although OCT is commonly used as a non-contact imaging technique, its application in in vivo skin measurement is limited by several challenges such as patient movement, uneven skin geometry, and specular reflection from the skin surface. The relatively moderate acquisition speed (1.5 sec per 3D scan) and the relatively bulky and unfixed imaging probe also lead to challenges in aligning the probe with the patient's skin and remaining stable during imaging. Thus, a contact approach is often used in skin imaging to mitigate these challenges [148], [191], [199], [202]. Using a glass window in front of an imaging spacer between the probe and the skin can flatten the skin and stabilize motion during imaging, which is also helpful for locating the imaging region [150]. However, the extent to which the epidermis deforms under compression from the imaging probe is unknown. Under contact pressure, the intrinsic flexibility and cellular composition of the epidermis make it susceptible to deformation, leading to the measurement of the epidermis thickness being underestimated. Recognizing that pressure could influence the accuracy of epidermis thickness measurement, in this paper, we utilized a contact OCT imaging probe integrated with a pressure sensor to assess how the epidermis would deform during contact imaging. By measuring the changes in epidermal thickness and capillary density within the superficial papillary dermis under different pressures, we aim to find the settings for reliably producing reproducible OCT scans and measurements, which is crucial for skin assessment.

5.1.2 Method

Human subjects

The study was approved by the Institutional Review Board (IRB) from the University of Washington. The study involved six volunteers (3 female and 3 male) aged between 20 - 30 years old with Fitzpatrick's phototype II, III, and V skins. Written consent for the research was obtained from each participant before imaging.

OCT imaging system

For our study, we employed an in-house-built swept source OCT system (SS-OCT). The configuration of this system closely resembles the setup used in our previous study [85]. The imaging system utilized a 200 kHz swept laser source (SL1310V1-10048, Thorlabs Inc.) with a central wavelength of 1310 nm and a bandwidth of 100 nm, resulting in an axial resolution of approximately 7.5 μm in air and 5.4 μm in tissue assuming the reflective index of 1.38. An LSM03 objective lens (Thorlabs Inc., USA) was employed to deliver the light onto the sample with a 5mW power. This probe provided a lateral resolution of approximately 25 μm. The system's dynamic range was measured at around 105 dB.

To maintain consistent contact between the probe and the skin of interest during imaging, we affixed a sample spacer to the probe and attached a disposable glass cover window on the space in contact with the skin as described in our previous study [191]. Force sensors were implemented to regulate the pressure exerted on the skin surface during OCT imaging acquisition. These sensors provided real-time force monitoring and recording, allowing for the measurement of the force or pressure applied to the skin surface during imaging [191].

Imaging protocol

Prior to OCT imaging, the imaging area on the forearm of the volunteer was cleaned and disinfected to remove debris. A washable marker was used to label the measuring site to maintain consistency in the imaging location. During scanning, the handheld probe was placed perpendic-

ular to the skin surface. Once a pressure level was stabilized, an OCT volume scan was captured, covering an area of approximately 8 mm $\times$ 8 mm $\times$ 1.5 mm (approximately 500 $\times$ 500 $\times$ 200 pixels) in the x (fast axis), y (slow axis), and z (penetration into the skin) directions, respectively. Each B-scan location within the 3D scan was repeated 8 times for the OCTA imaging protocol. The acquisition time for each 3D scan was approximately 1.5 seconds.

To assess the genuine effects of mechanical stress on OCT imaging by applying different pressure levels (approximately 0, 11, 17, 32, 45, and 69 kPa), the operator generated compression pressure by pressing the imaging probe onto the skin against the volunteer's forearm with the aid from the real time readings of the pressure sensor. To ensure and demonstrate data consistency, reliability, and repeatability, the scanning process was repeated at least three times regarding each pressure application. Between each consecutive scans, the imaging probe was detached and realigned to the same skin region of interest utilizing the white light camera for precise positioning.

Automated Segmentation of the Epidermal Layer

The mean OCT intensity B-scan image was taken for each 8-repeated B-frames and then log-compressed to reconstruct a tissue structural image based on light scattering. Figure 1 demonstrates the 3D rendering of a representative scan of the skin tissue with one representative cross-section scan, showing the depth-resolved information. The epidermis typically exhibits lower OCT intensity than the papillary dermis due to its distinct cellular structure, as demonstrated in Figure 1B. The segmentation of the epidermal layer in the 3D scanned volume was accomplished by detecting the dermal-epidermal junction using the difference between the intrinsic optical properties of the skin layers.

Firstly, the surface of the skin was detected with a semi-automatic segmentation software[184]. Then, the dermal-epidermal junction was detected by the maximum change within the structure intensities (red-line in Figure. 1b), which is based on the maximum derivative points using the differentiation model (the first derivative of Gaussian). Following the completion of segmentation, a manual check was conducted to ensure the segmentation accuracy.

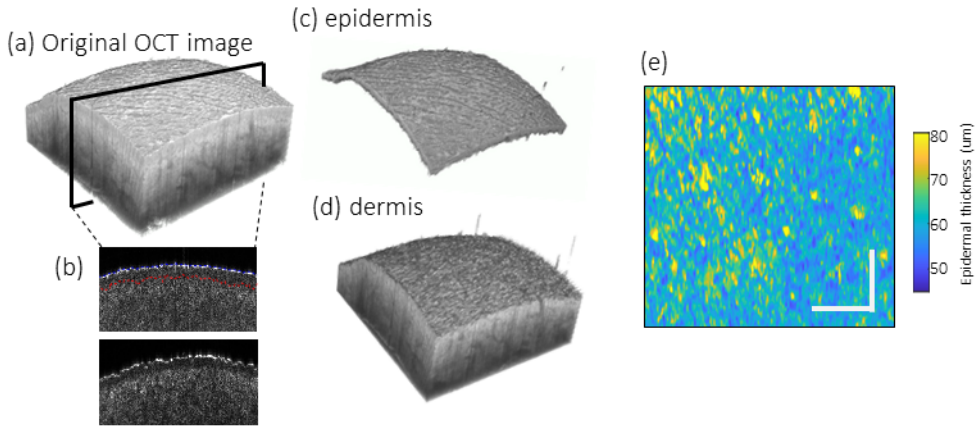

[**d!t**]

Figure 5.1: Workflow from 3D OCT scans to obtain epidermis thickness (ET) map. (a) 3D volume rendering of a representative optical coherence tomography scan, subject to segmentation. (b) representative B-scan showing the segmentation lines representing skin surface (blue line) and dermal-epidermal junction (DEJ, red line). The volume is segmented into two volumes: (c) the epidermis, and (d) the dermis, respectively. (e) en face ET map from the 3D epidermis volume shown in (c), false-color coded with the thickness information

After the surface and DEJ junction segmentation, the segmented volumes of epidermis (Figure. 1c) and dermis (Figure. 1d) were obtained. The epidermis volume was used to calculate the distance between the skin surface and the dermal-epidermal junction and projected to 2D en face maps for visualization of the spatial distribution of the epidermis (Figure. 1e). The thickness measurement was then converted from pixels to microns using the conversion factor that each pixel represents 3.75 microns. For better visualization, the thickness variation was represented with a color-coded en-face map that provides a top-down perspective of the thickness differences (Figure. 1e). Finally, an average epidermal thickness of the imaging region of interest was calculated as the average distance between the top of the skin surface and the DEJ junction within the whole field of view.

Optical Coherence Tomography Angiography

To obtain the skin microvascular information, temporal changes across the eight repeated B-scans were used to reconstruct vascular structures across the field of view (FoV) using the eigendecomposition-

based optical microangiography (ED-OMAG) method to create the OCT angiography (OCTA) images, representing microvascular information with the scanned tissue value [52], [151]. The en-face vasculature images were obtained by the maximum intensity projection from the 3D OCTA volume scan, specifically from the slab extending from the dermal-epidermal junction (DEJ) to 200 micrometers below corresponding to the papillary dermis. The vessel area density (VAD) metric was calculated by the percentage of pixels that are occupied by the capillary blood vessels in the en-face OCT image. Specifically, the grayscale OCTA enface scan was converted to a binary vessel area map for the calculation of the VAD as a ratio[55].

Statistical Analysis

Statistical tests were conducted to understand the extent of subtle epidermis deformation with the applied pressure levels and to pinpoint specific pressure points where the skin undergoes significant changes. A one-way analysis of variance (ANOVA) test was performed to compare the normalized epidermal thickness between imaging sessions. A significance level of $p < 0.05$ was employed to determine statistical significance.

5.1.3 Results

To evaluate the effects of mechanical pressure on the epidermis due to contact, a range of pressures from 0 kPa to 69 kPa was exerted onto the skin regions of interest. Figure 2 demonstrates the visual changes in epidermis thickness and microvasculature over the range of contact pressures applied. The cross-sectional OCT images (Figure 2, panels C and D) were selected to display the depth-specific details of where the epidermal-dermal junction lies.

Figure 3 illustrates the impact of compression on epidermal thickness and vascular imaging measured from OCT and OCTA volumes at the pressure level of 69 kPa. The epidermal thickness before and after compression (Figures 3a and 3b) showed a notable reduction in thickness. Cross-sectional OCT images (Figures 3e and 3g) show the deformation of the epidermis under compression, where the DEJ segmentation becomes closer to the surface segmentation.

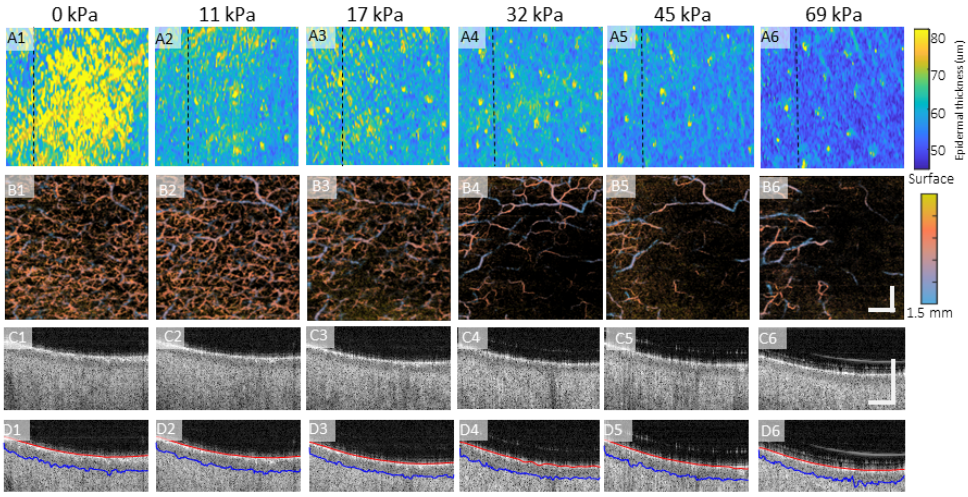

[**d!t**]

Figure 5.2: Visualization of the OCT-derived epidermal thickness (ET) map and microvascular maps illustrating changes under various pressures (as shown in top) applied to the skin regions of interest: (A1-6) Enface ET maps, and (B1-6) OCTA microvascular maps, respectively. (C1-6) representative OCT structural cross-sections B-frames at the positions marked as dashed lines in panel A, overlaid with (D1-6) the segmentation lines of skin surface (red line) and DEJ junction (blue lines). The ET and vascular maps are false-color coded with the color bar shown on the right. The scale bar represents 2 mm

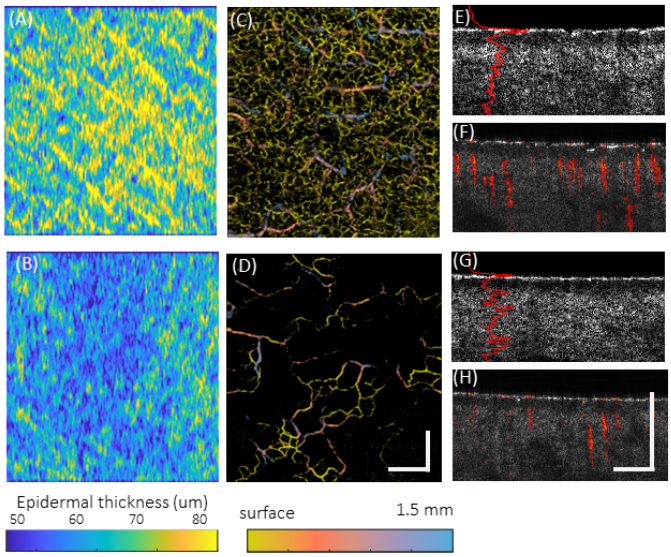

[**d!t**]

Figure 5.3: Comparative OCT and OCTA images between 0kPa and 69kPa. (A) The epidermis projection maps demonstrate the notable changes in thickness (A) without and (B) with contact pressure applied, respectively. The OCTA capillary projection maps of papillary dermis demonstrate the skin microvasculature (C) without and (D) with contact pressure applied, respectively. (E-H) Representative OCT B-scans showing the changes in tissue morphology and vasculature (E,F) before and (G, H) after the pressure is applied on the skin region of interest, where for better appreciation, (E, F) a representative A-scan profile (red) is overlaid on the B-scan image and (F, H) representative OCTA signals are overlaid on the B-scan images, respectively.

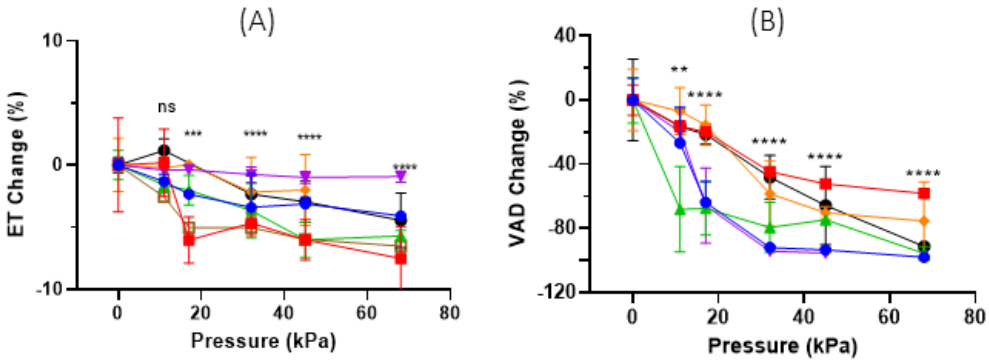

[d!t]

Figure 5.4: Measured changes in (A) epidermal thickness (ET) and (B) vascular density (VAD) as a function of applied pressures, respectively. The curves represent the normalized values against the baseline (no pressure applied). The error bars indicate the standard deviation from three repetitions. Each color corresponds to a different volunteer. ns denotes non-significant, ***, and **** indicate p values of 0.001 and p values < 0.001, respectively.

Without pressure applied on the skin surface, a dense capillary bed can be appreciated within the tissue, particularly in the superficial dermal layer, corresponding to the papillary dermis (Figures 3c and 3f). When a 69 kPa pressure is applied, most of the superficial capillaries become undetectable both in the projection image (Figure 3d) and in the B-scans (Figure 3h).

The measurements of ET and VAD as a function of the applied pressures are displayed in Figure 4. A negligible effect on ET measurement was observed under mild pressure (below 11 kPa) for most participants (Figure 4a), except for one subject. Epidermal deformation became significant when the compression pressure exceeded 17 kPa and continued to decrease as pressure levels increased. The VAD measurements showed a significant decreasing trend under compression (Figure 4b). Specifically, we observed up to a 10% decrease in ET and a 100% decrease in VAD between the two extreme pressure levels (0 kPa and 69 kPa).

Next, we extended our study to a special case by examining the change in ET and VAD on a one-week-old re-epithelialized scar in a 25-year-old participant (Figure 5). Figure 5a shows a photograph of the scar taken with a standard camera using visible light, which does not provide any details about the skin's thickness or blood vessels in the scar tissue. With the ET map from the OCT scan, the scar appears thicker than the surrounding healthy tissue (Figures 5b and 5d), and

no capillary was observed below the scar (Figure 5c). When a pressure of 69 kPa was applied to the scar, the ET map changed differently between the scar tissue and surrounding healthy tissue (Figure 5e), and the capillaries within the papillary dermis of the surrounding healthy tissue were diminished (Figure 5f). We observed a significant decrease in ET quantification in both the scar tissue and surrounding healthy skin (12.5% and 13.8%, respectively), indicating that under the compression pressure of 69 kPa from the imaging probe, the scar deformed 7% less than the healthy tissue.

5.1.4 Discussion and conclusions

In this study, we investigated the impact of contact OCT/OCTA imaging on skin imaging and observed that the epidermis and papillary capillaries are susceptible to subtle external pressures. Despite OCT studies that investigated cutaneous skin characteristics often choosing to use contact imaging [60], [199], [130], none reported the effect of contact pressure. The influence of mechanical stress exerted by the contact imaging probe has often been underestimated. Notably, this finding extends beyond OCT studies alone, as it is also relevant to various contact-based epidermis assessing techniques such as ultrasound [53], [34] and Skin Chips [111].

As shown in Figure 4, even slight pressure can change the epidermis measurements or microvascular perfusion within the tissue beds. This result demonstrated the sensitivity of OCT imaging and how contact imaging could potentially affect the accuracy of the measurements. Maintaining consistent contact pressure helps to minimize variability in measurements of epidermal thickness. This standardization is essential for longitudinal studies, clinical assessments, and treatment monitoring. The high-resolution and non-invasive nature of OCT imaging makes it a perfect tool to detect subtle changes in skin architecture with high precisions, especially the dermal-epidermal junction, which is often indicative of skin healthiness.

Figure 5 demonstrates the capability of discovering different levels of deformation in scar tissue when the imaging was conducted with a contact mode compared to nearby healthy skin. The thickness of cutaneous wounds and angiogenesis microvascular analysis from the surrounding

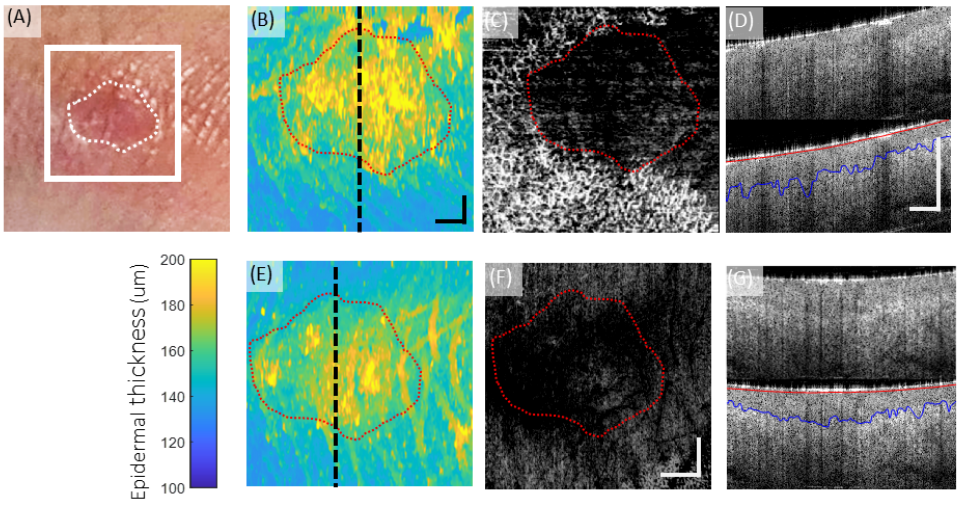

	0 kPa (μm)	69 kPa (μm)	Diff (%)
Scar (Mean ± SD)	168 (± 32)	147 (± 32)	12.5%
Normal	140 (± 30)	121 (± 29)	13.8%

[**d!t**]

Figure 5.5: Evaluation of epidermal thickness and vascular information in a scar tissue before and after a pressure of 69 kPa is applied. (A) white light imaging of the scar tissue. The white box represents the OCT imaging field of view. (B) Measured epidermis thickness map and (C) OCTA vascular map without pressure applied. (D) Representative B-scan with and without segmentation lines overlaid at the position marked by the dashed line in (B). (E) Measured epidermis thickness map and (C) OCTA vascular map with a pressure of 69 kPa applied. (G) Representative B-scan with and without segmentation lines overlaid at the position marked by the dashed line in (B). The table at bottom shows the measured values of epidermal thicknesses before and after the pressure was applied.

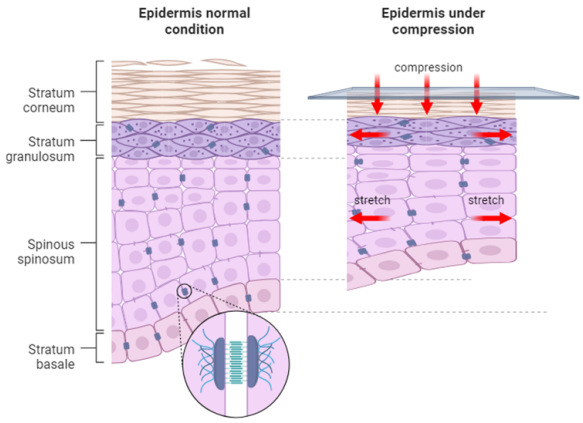

[**d!t**]

Figure 5.6: Mechanical properties and force dynamics in the skin. The left panel illustrates the epidermis components, including the stratum corneum, stratum granulosum, spinous spinosum, and stratum basale. The right panel is demonstrated as a load-bearing layer subject to forces like compression and stretch. These forces are shown as being transmitted within and across the skin layers. (Figure generated by BioRender)

capillary are the important biomarkers indicatives of the wound healing process [59], [102], [32]. Contact compression affects both the scar thickness and the integrity of microvascular information surrounding the scar. These results inferred the importance of precise pressure control during contact OCT imaging to ensure accurate and robust measurement, especially for the real-world scenarios of clinical diagnosis and cosmetic research.

When pressure is applied to the skin, the epidermis can undergo compression due to several intrinsic and extrinsic components that govern its mechanical response (Figure 6). The structure of the epidermis, which is composed of layers of keratinocytes, is designed to provide a barrier and protect underlying tissues. These cells can be compressed closer together under external pressure temporarily, protecting the skin from damage by absorbing and dissipating mechanical forces. A well-hydrated epidermis may exhibit more resilience to compression, while dry skin might be more susceptible to deformation[98].

Our results showed that the epidermis measurement is not susceptible to mild pressure (11 kPa) among all participants, with one subject not showing deformation to the others. This can be attributed to the inherent heterogeneity in skin responses to mechanical stimuli. Studies have

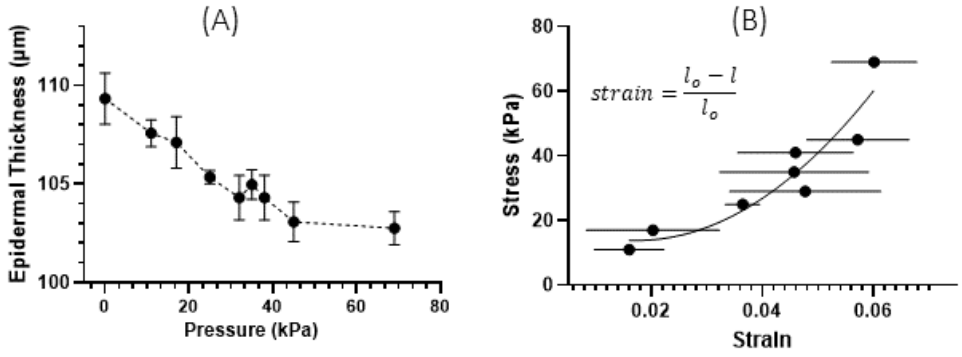

[d!t]

Figure 5.7: (A) Demonstration of the epidermis change of one participant with a finer scale of applied pressure. (B) the corresponding relationship between the strain and stress was calculated from the applied stress.

indicated that skin composition, thickness, and mechanical properties react variably to external pressure, leading to different outcomes in individuals [62]. Research also demonstrated that the epidermis's water content varies among individuals, indicating that the skin's hydration levels and response to pressure can vary [83]. Therefore, the diverse responses observed in the epidermis measurements under mild pressure, including the outlier subject, can be attributed to the complex interplay of variation in skin properties, hydration levels, and structural characteristics of the epidermis among participants.

By being sensitive enough to measure micrometer-scale changes, it may be envisioned, as a byproduct of this study, that the stiffness of the skin may be estimated with contact OCT imaging combined with the pressure sensor[97], [57]. Because of the ability of OCT imaging to measure the subtle changes in the epidermal thickness with known applied pressures, we conducted a preliminary experiment on one subject with a finer scale of pressures applied on the skin surface and then estimated the stress vs strain relationship, which is displayed in Figure. 7. The collagenous tissues like the skin can lead to an approximately exponential relationship between normal stress and strain in determining the nonlinear shear elastic response[97], [120], [31].

Using compression force and the epidermis thickness measurement to measure stress and strain in biological tissues can provide insights into tissue microstructure, but accurately quantifying

stress and strain in the epidermis is challenging due to difficulties correlating measured displacements with actual mechanical properties. The measurement of strain is limited by the boundary condition between the dermal and epidermal structures and the accuracy and homogeneity of the application stress using the design of the pressure sensors. Though we discussed the promising compression-related changes observed in the epidermis with our OCT scans, limitations exist for this study. First, the maximum difference of ET measurement between the two compression pressures is around 5-10%, around the axial resolution of the system in tissue. These subtle changes are reflected in the average ET calculated from the whole field of view (8mmx8mm), assuming a homogeneous epidermal structure. It provides an overall statistical assessment of epidermal deformation that aligns with the system's resolution capabilities. However, the variations in local cellular structure, epidermal thickness, and the presence of hair follicles and sweat glands may exhibit different responses to external forces. These variations could contribute to the epidermis' heterogeneous nature and can influence the overall averaged ET measurements. The local variations in the cutaneous skin under contact pressure should be evaluated in future studies. Additionally, although efforts were made to include volunteers with different skin types at similar age groups to mitigate potential bias, intrinsic factors like age, gender, ethnicity, and skin pigmentation can be further investigated to understand individual and collective impacts on epidermal deformation [101], [82]. Local variations in skin properties can introduce significant challenges in obtaining precise measurements across different anatomic locations and Fitzpatrick skin types[138]. Thus, a more comprehensive analysis with a larger participant size that considers the complex interplay of the aforementioned factors should be considered. In summary, this study investigated the impact of contact optical coherence tomography (OCT) imaging on the epidermis and capillaries. The findings demonstrated the sensitivity of OCT imaging to subtle pressure changes, which can potentially skew the measurement. Despite the common use of contact imaging in in vivo epidermis measurements used in previous OCT studies, the results evaluated the need for careful consideration of the design for contact-based epidermal assessment techniques to ensure accurate and reliable clinical measurements.

5.2 Investigation of the effect of compression pressure in contact OCT imaging on the measurement of epidermis thickness

This study presents a calibrated approach for Optical Coherence Tomography (OCT) to enable quantitative measurements of tissue anisotropy, aimed at improving the understanding of light-tissue interactions across different skin layers. OCT provides noninvasive, depth-resolved imaging with cellular resolution; however, it does not inherently measure scattering properties such as the scattering coefficient (μ_s), reduced scattering coefficient (μ_s'), and anisotropy factor (g). This work calibrated OCT using Mie theory with polystyrene standards to quantify the optical attenuation coefficient (μ) and reflectivity (ρ) from OCT A-scans. Monte Carlo simulations were employed to calculate anisotropy across skin layers, showing the epidermis with high anisotropy ($g = 0.9$) due to small, uniform cells with forward scattering. The papillary and reticular dermis exhibited moderate anisotropy ($g = 0.7 - 0.8$), with less directional scattering from collagen fibers with diffuse scattering. This calibration of OCT measurements facilitates the simulation of light transport in tissues for applications such as laser dosimetry and the quantification of biological parameters like tissue composition. These findings support the use of OCT as a quantitative tool for assessing tissue anisotropy, which has potential implications for tissue analysis in biomedical applications.

5.2.1 Introduction

Optical Coherence Tomography (OCT) has become an essential tool for noninvasive, high-resolution imaging of biological tissues, enabling cellular-level visualization of microstructural details across various layers of the skin. However, while recent OCT studies effectively reveal structural features of the skin using the optical attenuation coefficient [12, 23, 30, 49, 108, 180], it does not inherently quantify optical properties such as the scattering coefficient (μ_s), reduced scattering coefficient (μ_s'), or anisotropy factor (g). These properties are fundamental to understanding how light in-

teracts with biological tissues and are critical for applications requiring precise light transport measurements [81, 193].

Quantifying tissue scattering properties helps understand how light interacts with the distinct structures within skin layers[43, 69, 73, 192]. Each layer exhibits distinct structural and compositional characteristics that influence light transport. As the outermost layer, the epidermis contains densely packed, uniformly sized cells that lead to more forward scattering due to their compact arrangement. Beneath the epidermis, the papillary dermis consists of loosely organized collagen fibers, leading to broader and less directed scattering as light interacts. The reticular dermis, the deepest layer, comprises larger and densely packed collagen fibers, resulting in highly diffuse scattering due to the big collagen bundles. These differences in cell density and collagen fiber organization across layers create unique optical environments that influence how light propagates through each skin layer[50, 73].

To quantify μ_s and g, this study calibrates OCT to align with theoretical predictions based on Mie scattering principles theory to assess tissue properties effectively [38, 81, 95, 125]. Calibration was performed by integrating polystyrene microsphere standards with OCT, allowing for the measurement of the optical attenuation coefficient (μ) and reflectivity (ρ) directly from OCT A-scans. By implementing Monte Carlo simulations to model light propagation through human skin, this study infers reduced scattering coefficients (μ_s') by analyzing the relationship between μ and ρ and using the scattering coefficient (μ_s) and anisotropy factor (g).

This calibrated approach enables OCT to serve as a quantitative tool for assessing tissue composition with anisotropy. It expands its applications in fields that rely on light-tissue interaction modeling, such as laser dosimetry. Additionally, this approach allows for the conversion of optical measurements into biological parameters—such as tissue density, size, and collagen content—which may support clinical decision-making by identifying altered or abnormal tissues. Integrating Mie theory-based calibration and Monte Carlo simulations with OCT structural imaging represents a novel framework for advancing OCT from qualitative imaging to a tool capable

of quantifying scattering properties, thus providing a comprehensive method for understanding and simulating tissue health and composition across various biomedical applications.

5.2.2 Method

Optical Coherence Tomography (OCT) System

A custom-built OCT system operating at a center wavelength of 1310 nm was used to acquire depth-resolved scans. The OCT system has an axial resolution of 6.5 μm and a lateral resolution of 24 μm in tissue. For each measurement, the OCT system acquired B-scans and corresponding A-scans at a frame rate of 50 frames per second. The data were collected in BM mode by capturing a single B-scan at each location before moving to the next B-scan position, continuing this process until the entire volume was scanned. Along the fast axis, each B-scan consisted of 500 A-scans, captured at an A-scan rate of 200 kHz. The complete volume scan consisted of 500 B-scans along the slow axis, covering a total area of 8 mm $\times$ 8 mm $\times$ 3.75 mm. Each scan of the full volume was completed in approximately 1.75 seconds.

Preparation of Polystyrene Microspheres

Polystyrene microspheres were used as a calibration standard to calibrate the OCT measurements to theoretical predictions of light scattering. A solution of polystyrene microspheres with a diameter of 0.1 μm was prepared in a 96-well microplate at different concentrations between 0.1 and 2.5%. The depth-resolved OCT a-scan from these samples was used to extract the attenuation coefficient (μ) and reflectivity (ρ) values.

OCT Imaging and Measurement of Skin Layers

This study involving human skin samples complied with ethical guidelines and was approved by the Institutional Review Board (IRB) of the University of Washington. All procedures adhered to the principles outlined in the Declaration of Helsinki, ensuring participants' safety, privacy, and well-being. Before sample collection, informed consent was obtained from all participants,

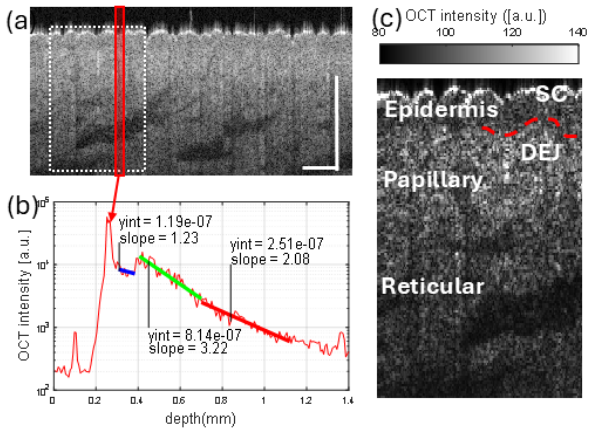

Figure 5.8: Depth-Resolved log-scale OCT Imaging of Skin Layers with A-Scan Analysis for skin. (a) OCT image of skin. The red line indicates the A-scan position. The white box indicates the zoomed-in positions. Unflatten picture co-align surface at 1 plane. (b) Averaged A-scan intensity profile with different slopes corresponding to different layers of the skin from red box in (a). (c) Zoomed OCT intensity map with labeled skin structures. Scale bar represents 1mm

who were fully informed about the study's purpose, procedures, and potential risks. OCT measurements were performed on 15 *in vivo* human skin samples obtained from the forearm of 5 volunteers (M=2, F=3).

To extract OCT depth-resolved a-scans from the skin images, the OCT B-scans were flattened to correct the curvatures in the skin surface. Next, to reduce OCT shot noise and increase the signal-to-noise ratio, every ten adjacent A-scans were averaged to create a single representative OCT scan. Figure 1 demonstrates the structural organization of human skin layers in an OCT B-scan image, which reveals distinct layers, including the epidermis and dermis. In Figure 1(c), the OCT B-scan image shows the depth-resolved cross-section of the skin, revealing distinct layers. Figure 1(b) presents the depth-resolved A-scan intensity profile corresponding to the red line in (a). The epidermis, papillary dermis, and reticular dermis layers were then manually labeled based on distinct changes in OCT signal attenuation and intensity. The layer boundaries were marked at the first noticeable transition in the attenuation profile and OCT intensity, which aligned with each layer's structural and optical characteristics (Figure 1).

Workflow for extracting anisotropy and scattering coefficients

Figure 2 depicts the workflow of this study to obtain the anisotropy (g) and scattering coefficient (μ_s) values. The workflow includes three main stages: standard calibration, calibration correction, and Monte Carlo (MC) simulation.

The initial step involves standard calibration using OCT A-scans for polystyrene samples. The attenuation coefficient and reflectivity of each layer were then calculated using linear regression of the OCT reflectance (ROCT) in log scale by the linear equation ROCT $= (\text{slope} \cdot z_{depth}) +$ y-intercept, where the slope corresponds to the attenuation coefficient (in [**dmm^{-1}**]), and the y-intercept represents the reflectance. A correction is applied to the attenuation and reflectance using the coefficients obtained from the polystyrene standards to correspond with the prediction from Mie Theory (Figure 2).

The corrected values of μ and ρ are inputs for the MC simulation. In the MC simulation, a grid is generated using the scattering parameters (e.g., μ_s, OCT coherence gate length L_{CG}, back scatter factor b, and the numerical aperture NA). The MC simulated grids tell the optical properties, allowing for the calculation of the anisotropy (g), scattering coefficient (μ_s), and reduced scattering coefficient ($\mu_s' = \mu_s(1-g)$), which are essential for characterizing tissue optical properties.

5.2.3 Results

Polystyrene standards were employed to calibrate the OCT system for accurate measurements of tissue scattering and reflectivity (Figure 3). OCT depth profiles were acquired for polystyrene microspheres suspended in a microplate well, spanning concentrations from 2.5% to 0.1%. The theory predicts a linear relationship between particle concentration and attenuation coefficient, and this was confirmed by the data, which demonstrated an excellent linear correlation between particle concentration and the attenuation coefficient. Concentrations below 0.5% were excluded, as the reduced particle density led to decreased scattering efficiency, with water absorption dominating the signal. This resulted in insufficient scattering properties for reliable calibration.

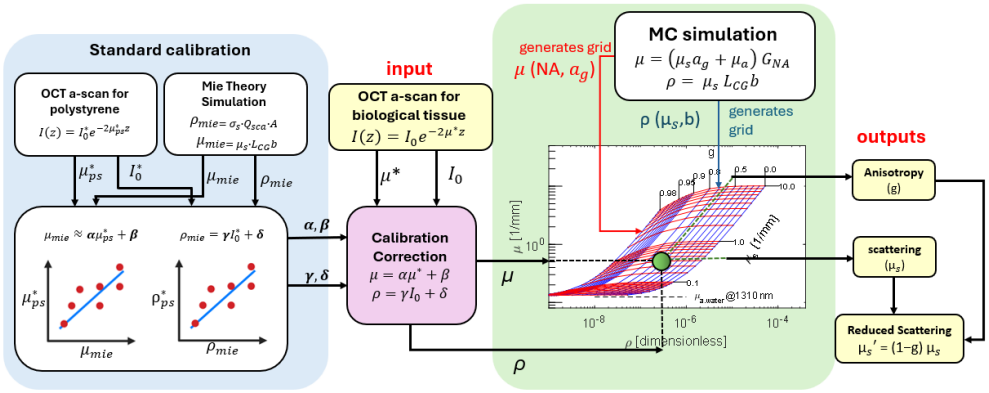

Figure 5.9: Calibration workflow for calculating optical properties of biological tissue using Mie theory and Monte Carlo (MC) simulations. This workflow comprises three main stages: standard calibration, calibration correction, and MC simulation. The Henyey-Greenstein phase function, represented by b, is used to model the angular scattering distribution, described by: $b = p(\cos\theta) = \frac{1-g^2}{(1+g^2-2g\cos\theta)^{3/2}}$. The MC simulation incorporates several factors to refine the model, including the geometric factor $G_{\mathrm{NA}} \approx 1 - \exp\left(-\frac{\mathrm{NA}^2}{2(1-g)}\right)$. Additionally, the scattering coherence modulator a_g is defined as $a_g = 1 - e^{-\left(\frac{1-g}{0.155}\right)^2}$.

In Figure 4(a), the experimental scattering coefficient (μ_{expt}) demonstrates a strong linear correlation with the Mie-predicted scattering coefficient (μ_{mie}), following the equation $\mu_{\mathrm{expt}} = 0.241 + 0.493 \times \mu_{\mathrm{mie}}$. Similarly, Figure 4(b) shows a linear relationship between the dimensionless scattering parameter (ρ_{expt}) and its theoretical counterpart (ρ_{mie}), with a calibration equation $\rho_{\mathrm{expt}} = 4.5 \times 10^5 + 1.0 \times 10^{12} \times \rho_{\mathrm{mie}}$.

Figure 5 presents the relationship between the experimentally measured attenuation coefficient (μ) and the dimensionless reflectivity (ρ), compared against Mie theory predictions. The gridlines illustrate the corresponding theoretical scattering coefficients (μ_s) and anisotropy factors (g) using Monte Carlo simulation. The uncorrected experimental data (green circles) exhibit higher μ values than Mie theory (black line), particularly at lower concentrations. After applying corrections based on Mie theory (cyan circles), the data align more closely with the theoretical predictions. However, the correction using the exponential decay method (red circles) underestimates μ, especially at lower reflectivity values.

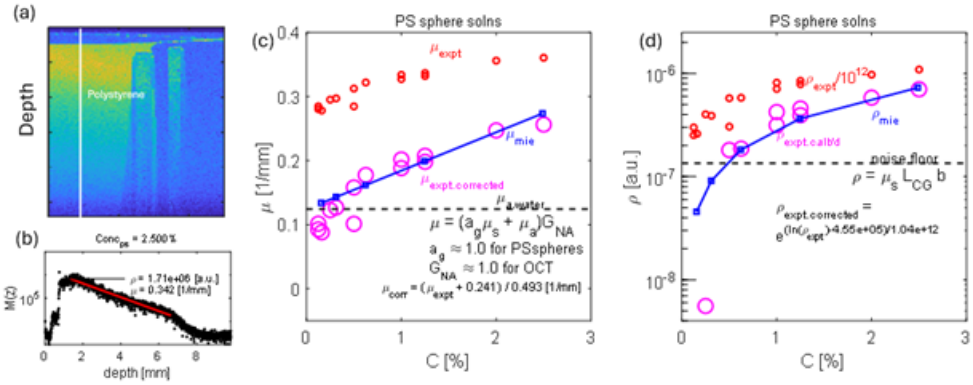

Figure 5.10: Comparison of optical properties of polystyrene samples measured by OCT with Mie theory. (a) Depth profile of polystyrene microspheres in a phantom visualized by OCT. (b) A-scan of polystyrene at 2.5% from the solid white line in (a), showing attenuation and reflectivity. (c) Experimental attenuation coefficient μ_{expt} compared with Mie theory as a function of concentration. (d) Measured reflectivity ρ_{expt} compared with Mie theory as a function of concentration.

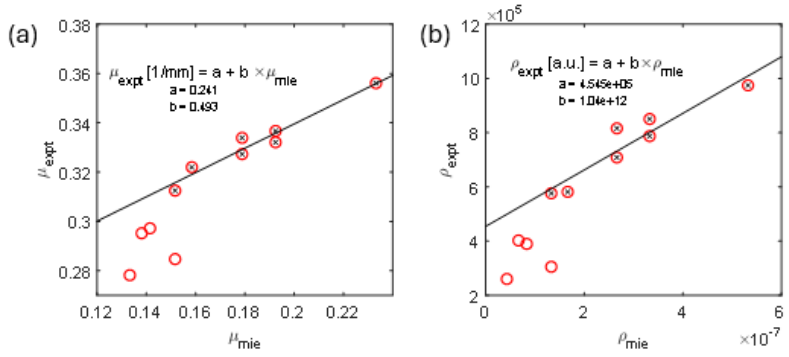

Figure 5.11: Calibration of experimental scattering measurements against Mie theory predictions. (a) Calibration curve for the scattering coefficient (μ_{expt}) in units of [**d1/mm**] compared to the theoretical Mie scattering coefficient (μ_{mie}). (b) Calibration curve for the dimensionless scattering parameter (ρ_{expt}) compared to the Mie-predicted scattering parameter (ρ_{mie}).

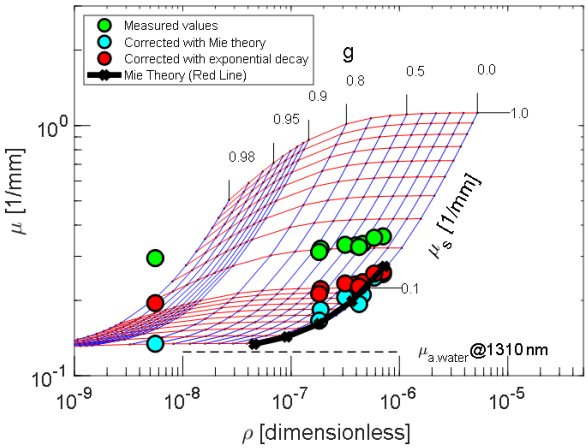

Figure 5.12: Calibration of experimental scattering measurements against Mie theory predictions. (a) Calibration curve for the scattering coefficient (μ_{expt}) in units of [**d1/mm**] compared to the theoretical Mie scattering coefficient (μ_{mie}). (b) Calibration curve for the dimensionless scattering parameter (ρ_{expt}) compared to the Mie-predicted scattering parameter (ρ_{mie}).

Figure 6 illustrates the relationship between the experimentally measured scattering coefficient (μ_s) and dimensionless reflectivity (ρ) across different skin layers—epidermis, papillary dermis, and reticular dermis—alongside Monte Carlo predictions. The scattering coefficient values, μ_s, range from approximately 1 to 3 for the epidermis, 1 to 2 for the papillary dermis, and 0.5 to 1 for the reticular dermis, with corresponding anisotropy factor (g) values of 0.9 to 0.95 for the epidermis, 0.7 to 0.8 for the papillary dermis, and 0.7 to 0.85 for the reticular dermis. The experimental data points form distinct clusters for each layer, reflecting the unique scattering properties (represented by μ_s) and anisotropy factors across skin layers.

5.2.4 Discussion

This study demonstrates the feasibility of calibrating Optical Coherence Tomography (OCT) measurements with theoretical predictions using Mie theory and polystyrene standards to provide a comparative basis for theoretical and experimental data alignment. Through the calibration process, we derived the scattering coefficient (μ_s) and anisotropy factor (g) using Monte Carlo simulations to explore the optical properties across different layers of human skin to quantify op-

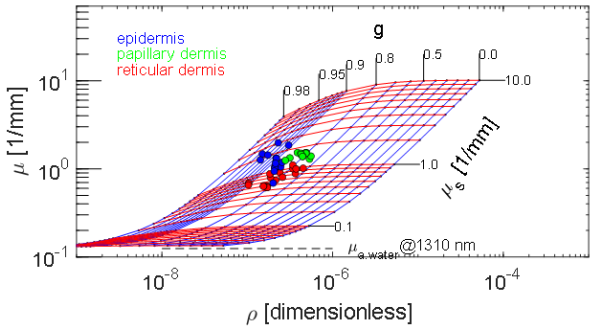

Figure 5.13: Calibration of experimental scattering measurements against Mie theory predictions. (a) Calibration curve for the scattering coefficient (μ_{expt}) in units of **[d1/mm]** compared to the theoretical Mie scattering coefficient (μ_{mie}). (b) Calibration curve for the dimensionless scattering parameter (ρ_{expt}) compared to the Mie-predicted scattering parameter (ρ_{mie}).

tical properties in biological tissues. This framework offers insights into OCT's ability to measure tissue properties quantitatively and potentially advance its application in in vivo diagnostics.

The reflectivity calibration, ρ, was performed by measuring the intensity from OCT A-scans of polystyrene standards and matching it with theoretical predictions from Mie theory. This approach converts OCT intensity values (in arbitrary units) to reflectivity values, effectively correcting for variations in OCT input power, collection efficiency, dynamic range, and numerical aperture (NA), making reflectivity correction straightforward and theoretically predictable [86]. One aspect that requires careful consideration is the variation in viewing angle. Angle changes affect the reflectivity signal's perceived intensity, which cannot be easily corrected through theoretical adjustments alone.

Similarly, the alignment of the scattering coefficient, μ, was achieved by measuring the slope from OCT A-scans of polystyrene standards and matching it with Mie theory. This calibration corrects the focus function and system sensitivity roll-off to reflect correspondence between experimentally observed OCT data and expected values from Mie theory[43, 92].

The scattering coefficient (μ) and anisotropy factor (g) calculated using Monte Carlo simulations introduce new insights into OCT's clinical and research applications. Quantifying these parameters allows for a better understanding of tissue scattering and the directionality of light

propagation, both critical for modeling light behavior in tissues. This quantitative framework enhances OCT's potential as a diagnostic tool by providing more detailed insights into tissue composition, which could support applications such as cellular and molecular characterization, such as density, sizes, and shapes based on scattering properties.

In this study, in vivo OCT measurements of human skin revealed distinctive scattering characteristics across specific tissue layers. The epidermis, which exhibited an anisotropy factor ranging from 0.9 to 0.95, showed lower attenuation than the dermal layers, likely due to its higher density of smaller and more tightly packed keratinocyte cells. In contrast, the papillary dermis displayed an anisotropy factor between 0.7 and 0.8, while the reticular dermis ranged from 0.7 to 0.85. The dermis is notably more collagenous, particularly in the reticular layer, which demonstrated the highest scattering coefficient values (μ), indicating increased light scattering due to its dense collagen composition. These observations align with the known optical properties of skin, supporting the feasibility of calibrated OCT to differentiate between the layered skin structures and compositions effectively.

For applications with low scattering coefficients (typically under 10 mm^{-1}), a single scattering model can adequately represent OCT scattering effects [12, 63, 108]. However, a limitation in this study arises from relying on this single scattering approach to model the attenuation coefficient. This method does not consider multiple scattering contributions from tissue elements like blood, collagen, and cellular structures, which can influence the OCT signal, especially in more complex tissues. This method can also incorporate multiple scattering models if the sample involves higher scattering environments [93, 168].

Moreover, the focus function, system roll-off, and sensitivity response of the optical components—such as the photodetector in the SSOCT system—are challenging to profile precisely[23, 43, 73]. However, for this study, we assumed these factors would attenuate linearly so that the measured attenuation could be calibrated using Mie's theory[92].

The OCT slope method used to estimate the attenuation coefficient in this study exhibits limited sensitivity to concentration changes at lower concentrations, largely due to its reliance on

fitting the exponential decay of the OCT signal. This approach is highly noise-sensitive, mainly when fewer pixels per layer are available or when only a limited number of A-lines are averaged. The insufficient pixel count especially impacts the measured signal quality for the epidermal layer. We implemented manual labeling to maximize accuracy in epidermal measurements; however, some inaccuracy remains. Future work could address these limitations through depth-resolved model-based reconstruction, such as Vermeer's method[12], which can improve accuracy but requires careful calibration to avoid errors introduced by baseline drift or background signal fluctuations.

Lastly, the calibration approach employed in this study was optimized explicitly for the experimental conditions unique to this setup. As such, the calibration is not directly transferable to other studies or imaging systems without recalibration.

In summary, this study establishes a framework for calibrating OCT measurements using Mie theory and demonstrates the method's effectiveness in quantifying optical properties in both polystyrene standards and human skin. The application of correction factors improves the alignment of OCT measurements with theoretical predictions, affirming OCT's potential as a quantitative tool for assessing tissue scattering characteristics. Continued advancements in OCT calibration methods and correction protocols will be instrumental in broadening OCT's utility for biomedical research and clinical diagnostics, particularly in applications requiring detailed analysis of tissue scattering and reflectivity.

5.3 Exploring the Age Factor of Skin Parameters with Optical Coherence Tomography for Skin Aesthetic

A quantitative study of epidermal and dermal skin as a function of age was carried out with Optical Coherence Tomography (OCT) and OCT Angiography (OCTA). OCT and OCTA have the advantage of assessing skin aging by providing non-invasive, high-resolution, depth-resolved imaging capabilities that enable precise visualization of microstructural changes in the skin, such

as epidermal thickness variations, microvascular alterations, and collagen degradation. Our study leveraged eight OCT parameters to quantitatively and qualitatively analyze age-related variations in skin properties on the forearm skin across different age groups. Parameters such as "roughness", "Epidermal Thickness Variability", "Papillary dermis reflectance", "optical attenuation coefficient", and "vessel area density" has shown significant differences between age groups on the forearm indicating their effectiveness in measuring changes due to skin aging. The comprehensive analyses show the potential of OCT and OCTA for measuring skin aging with the aforementioned parameters.

5.3.1 Introduction

Among the major aesthetic concerns, aging is the inevitable process that brings about significant changes in our skin: more wrinkles, reduced elasticity, and variations in hydration levels [154], [37]. These transformations in skin characteristics have long been a subject of interest, particularly in developing effective anti-aging cosmetics[99]. Dermatology measurement in clinics distinguishes the topography of the skin's surface for the assessment of wrinkles as the most important characteristic indicative of aging [110], [76]. On the other hand, most in vivo measurements cannot assess the skin underneath the skin surface. Thus, OCT fills the gap as a noninvasive depth resolve technique to assess and quantify aging subcutaneously.

Optical coherence tomography (OCT) is an optical three-dimensional depth-resolved imaging technology that captures biological tissue images using interference light. The intrinsic signal from OCT structure images can be used to distinguish skin's multilayer structures including the epidermis, and dermis, as well as the micrometer scale components including the collagens [154], [200], [11]. With functional OCT, or OCT Angiography (OCTA), the capillary bed from the same scan can be extracted with micron-level resolution, and millimeters of depth in vivo using a motion-sensitive algorithm [175], [176], [205], [206]. Biophysical parameters from OCT and OCTA combined together can provide high-resolution, non-invasive cross-sectional images of the skin's microstructure and microvasculature for cross-references [61], [116], [72], [118]. Studies

have already shown that OCT is highly beneficial in the evaluation of the efficacy of many skins' aesthetic features, including the assessment of scars [99], [33], [2], [103] and wound healing [103].

The aim of this study was to implement a quantitative method for identifying the impact of chronological aging on skin parameters using OCT and OCTA. We obtained OCT in vivo images of the skin on the forearm across several age groups to evaluate biophysical markers related to aging. The purpose of the study is to analyze the correlation between aging and the corresponding biophysical properties of their skin: skin capillary density, epidermis morphology, and light attenuation property of skin. This study demonstrates the feasibility of using OCT for in-depth skin aging analysis and sets a foundation for future explorations to refine diagnostic or therapeutic approaches in managing age-related skin changes.

5.3.2 Method

Study Design and Participants Recruitment

This study was designed to investigate the correlation between the age of volunteers and the biophysical properties of the skin layers: blood and nutrient supply from the capillary, epidermis morphology, and skin's light-attenuation property. The aim was to discern the trends these skin parameters exhibit across different age groups and to explore their susceptibility to improvement. The study was conducted from clinical studies focusing on in vivo aging evaluation of human skin. The participant cohort comprised approximately 45 subjects, stratified across young (18$\tilde{3}$5 years old) and aged (50$\tilde{6}$2 years old) groups to ensure a comprehensive analysis of aging effects on skin biophysical properties.

The study protocol was reviewed and approved by the Institutional Review Board (IRB) of the University of Washington. All participants provided written informed consent before participation. Participants were selected based on inclusion criteria that required them to be over 18 years of age with no history of skin diseases or conditions that could affect the biophysical properties of the skin, such as psoriasis, eczema, or recent sunburns. Exclusion criteria included the use of

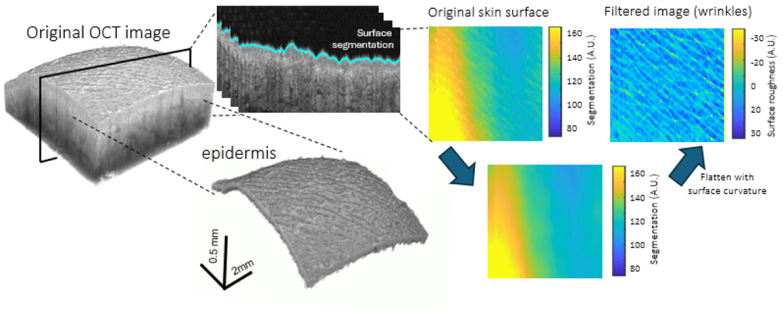

Figure 5.14: Schematic overview of the image processing protocol for obtaining surface topology maps

systemic medications known to affect the skin's physiology and cosmetic procedures within the last six months.

Surface Topology Analysis and epidermis Segmentation

As illustrated in Figure 1, the surface and epidermis segmentation can be obtained from the 3D volume OCT data. The acquired 3D volume data is processed through a projection algorithm to generate a 2D representation of the skin's surface. Following projection, an automated segmentation algorithm is applied to detect the skin's surface from the underlying structures.

The skin surface curvatures in the surface topology maps were removed by applying the medium filter method to reveal the true topography of the skin surface (Figure 1). The flattening is done by transforming the skin surface image into the frequency domain filtering out the slower frequencies and applying the inverse. The decision to choose the filter from other methods was illustrated in the appendix.

The Dermis-Epidermis Junction (DEJ) is identified within the volume data using the optical contrast between the epidermis and dermis. Here, the DEJ serves as an anatomical marker for adjusting the skin's natural curvature in the image-processing phase. The 3D volume data of the skin's surface is flattened according to the location of the DEJ. The curvature-adjusted surface is then analyzed for topographical features, including roughness, and wrinkles.

Optical Attenuation Coefficient (OAC) Methods

The Optical Attenuation Coefficient (OAC) is a key parameter in Optical Coherence Tomography (OCT) that quantifies how much light is reduced in intensity as it propagates through a scattering medium, such as biological tissue. This measurement provides essential insights into tissue properties, enabling quantitative assessment of tissue composition and structural characteristics. The following subsections describe the principles and methods used to calculate the OAC in OCT imaging.

The OAC, denoted by μ, is calculated using the following fundamental equation:

$$\mu = -\frac{1}{d} \log\left(\frac{I(d)}{I_0}\right) \tag{5.1}$$

where μ is The total optical attenuation coefficient,(mm^{-1}), d is the depth or thickness of the tissue through which the light has traveled, measured in meters, $I(d)$ is the intensity of light after it has traveled a distance d through the tissue, I_0 is the initial intensity of the light before entering the tissue.

This equation derives from the Beer-Lambert law, which describes exponential decay in light intensity as it penetrates a scattering medium. It assumes a single scattering model and homogeneity within the analyzed tissue segment.

To ensure accuracy, calibration methods are applied to account for multiple scattering effects that may influence OAC measurements. Calibration involves imaging a known phantom, 100 nm polystyrene beads, which provides a baseline scattering profile. By comparing OCT intensity measurements from the tissue to those from the calibration sample, corrections can be applied to account for system-specific variations and multiple scattering artifacts. Mie theory is often used in the calibration process to calculate the scattering coefficient and efficiency, which are integrated into OCT intensity measurements.

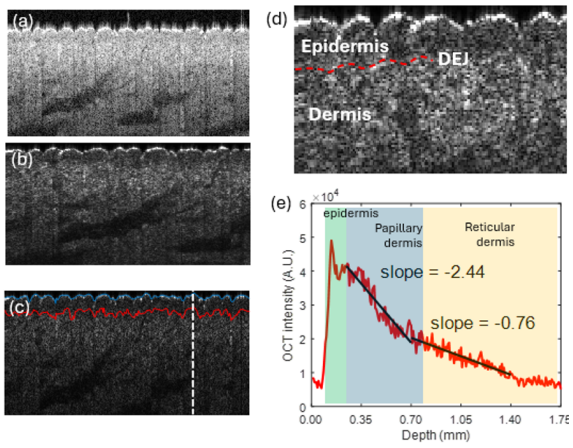

Figure 5.15: Scheme overview of Optical Coherence Tomography (OCT) structure and Optical Attenuation Coefficient (OAC) measurement techniques in the skin. (a) B-scan of OCT backscattering intensity, illustrating the internal structure of the skin. (b) OAC-enhanced contrast of the skin B-scan, highlighting differences in tissue properties. (c) labeling of the skin surface and epidermis within the B-scan. Zoomed-in view of the OAC contrast-enhanced B-scan, showing finer details. (e) A scan demonstrates the attenuation of light as it travels through the skin layers.

OCT measurement parameters

The study employed biophysical measurement on the 3D OCT images to evaluate the skin's capillary density, capillary-tissue diffusion flux, surface roughness, epidermal thickness, epidermal variation, and optical attenuation coefficient (Figure 3).

Statistical Analysis

Data were analyzed by unpaired t-test for the measured biophysical properties of the skin to determine if these properties exhibited any discernible patterns across different age groups. Statistical significance was set at $p < 0.05$.

5.3.3 Results

Figure 4 shows the 3d map, projection map, and the bscan image (forearm skin of a 26- and 50-year-old male) of backscatter light intensity. Notable differences in skin characteristics were ob-

Table 5.1: Description of the OCT parameters and equations

Parameter	Description	Equation
Surface Roughness (Sq)	Root mean square (RMS) height of the surface, which provides a measure of the average height deviations squared on the skin surface topology map from OCT images. $z(x, y)$: The height function of the surface at coordinates. A: The total area over which the surface is being evaluated.	$Sq = \sqrt{\frac{1}{A} \iint Z(x, y)^2 \, dx \, dy}$
Optical Attenuation Coefficient (OAC)	OAC measures how much light is reduced in intensity as it passes through the skin. μ: the total optical attenuation coefficient (m^{-1}); d: depth of the tissue in meters; $I(d)$: intensity of light after traveling a distance d; I_0: initial intensity.	$\mu = -\frac{1}{d} \log\left(\frac{I(d)}{I_0}\right)$
Tissue Reflectivity	Quantitative link between observed OCT intensities and reflectivity. Reflectivity R calibration was derived using intralipid (IL) size distribution, volume fractions, and densities. Mie theory was used to calculate scattering properties, which were integrated with OCT intensity measurements.	$R = 10^{\frac{I_{\text{OCT}} - a}{b}}$, where $a = 7.63 \times 10^4$ and $b = 1.11 \times 10^4$
Epidermal Thickness (Mean and SD)	Average thickness of the epidermal layer, including the standard deviation.	$\bar{E_T} = \frac{1}{A} \iint ET(x, y) \, dx \, dy$ $\sigma_{ET} = \sqrt{\frac{1}{A} \iint ET(x, y)^2 \, dx \, dy}$
Vessel Area Density (VAD)	Proportion of the total area of a tissue section occupied by blood vessels in an OCT en face image, typically expressed as a percentage.	$VAD = \frac{\text{Area of vessels}}{\text{Total Area}} \times 100$
Capillary-to-Epidermal Thickness Ratio (CETR)	Quantifies the ratio between capillary density and epidermis thickness using OCTA, providing insights into nutrient supply relative to skin barrier properties.	$CETR = \frac{VAD}{ET}$

served between younger and older age groups. Specifically, aged skin samples exhibited a 21.8% rougher texture compared to their younger group. This increased roughness was found with evident in the enhanced prominence of wrinkles (figure 5a), and overall surface irregularity for intuitive confirmation of the expected age-related changes in skin topography. The thickness of the epidermis does not show any differences between the two groups on the forearm skin (Figure 5b). However, aged groups showed thickening in local regions of the wrinkle regions, which can also be quantitatively observed by the 37.6 % increase in their epidermal thickness variations to that of the healthy groups (Figure 5c).

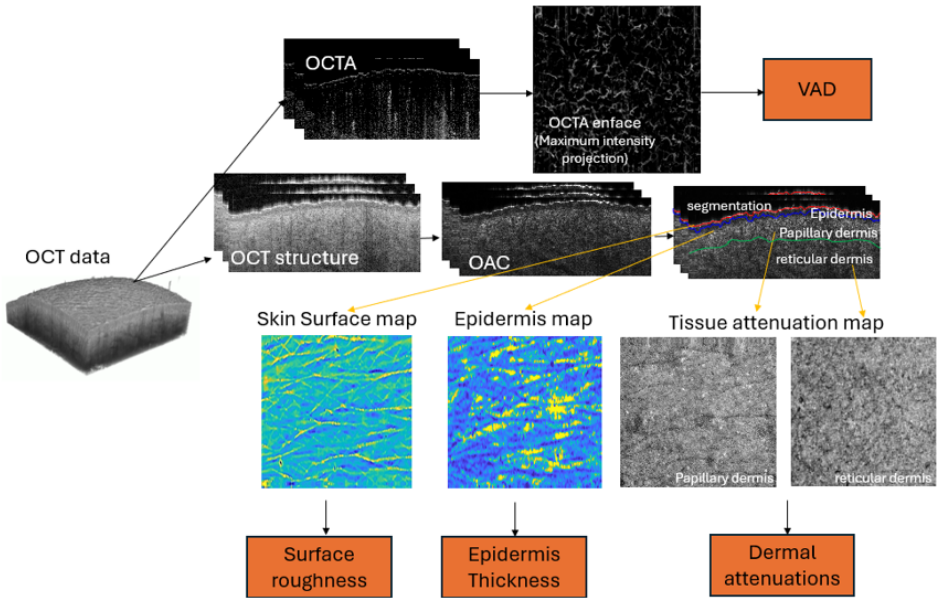

Figure 5.16: Scheme showing the process flow to obtain the biophysical parameters within the skin.

The optical attenuation coefficient is a quantitative measure of how much light is reduced in intensity due to absorption and scattering as it passes through the skin tissue. The attenuation in the papillary dermis is generally higher than in the reticular dermis, due to its denser collagen network and more compact structural arrangement, which influences how light is absorbed and scattered within these layers. In Figure 8, both the OAC and reflectance measurements in the reticular dermis show a significant decrease in aged skin compared to younger skin. However, no significant variation was observed between the papillary dermis with age.

In addition to changes in surface texture, the microvasculature map also provides important information regarding the aging of the skin. In the aging skin, fewer visible capillaries and a general decrease in the density of the vascular network were found in the papillary dermis (Figure 6). However, no significant differences were found in the vasculature structure in the reticular dermis (Figure 7). Aged skin displayed a significant reduction in vascularization (Figure 9a) and capillary tissue perfusion (Figure 9b). The microvascular map and the attenuation of the backscatter map

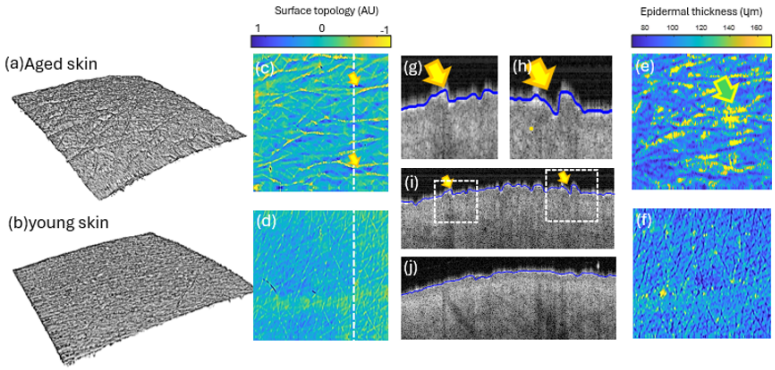

Figure 5.17: Comparison between aged and young skin. (a) and (b) The 3D view of the epidermis. (c) and (d) The surface roughness projection. (i) and (j) the cross-section of the OCT structure at the yellow solid line in (b) and (f) respectively. (g) and (h) zoomed-in wrinkles in the -b-scan cross-section in (i). (e) and (f) The epidermal thickness map. The Yellow arrow identifies the wrinkles in aged skin. The Orange arrow depicts the wrinkles in the aged skin. The green arrow depicts the hyperplasia in the aged skin.

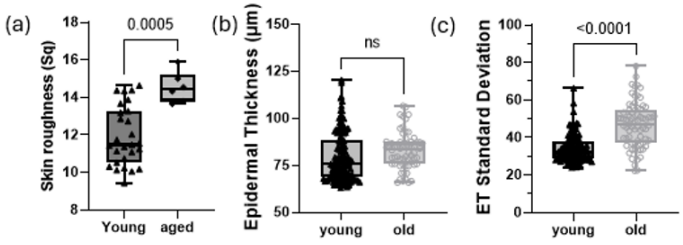

Figure 5.18: Quantification Comparison for (a) The surface roughness (b) The epidermal thickness map between young and aged skin. (c) The standard deviation in the epidermal thickness map. ns: Nonsignificant.

can be separated based on the depth-resolved image and segmentation of the skin layers (epidermis, papillary dermis, and reticular dermis).

5.3.4 Discussion

This study introduces new biophysical characteristics besides epidermal roughness to measure the aging of skin in OCT images. The inner forearm skin of the young and aged skin was measured. We have demonstrated qualitative and quantitative parameters to separate age-related variations in skin properties. OCT enables the depth-resolved visualization of microscopic changes in the skin's

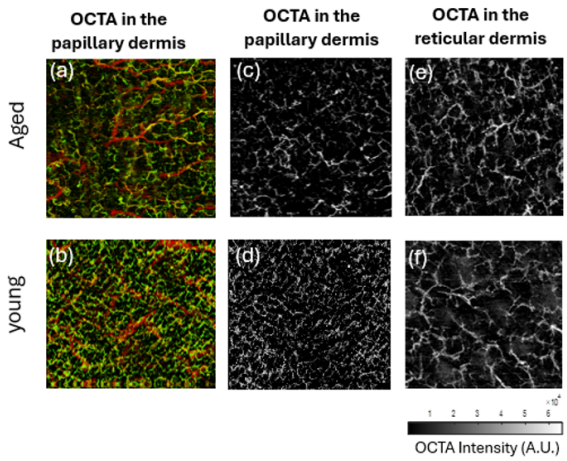

Figure 5.19: Comparison between vessel area density between the young and aged cutaneous capillaries on the forearm. (a) and (c) Capillary vasculature from the papillary dermis. (b) and (d) depth-resolved vasculature of the microvasculature among the whole depth, where the superficial vessels are color-coded in green, and the deeper vessels are color-coded in red.

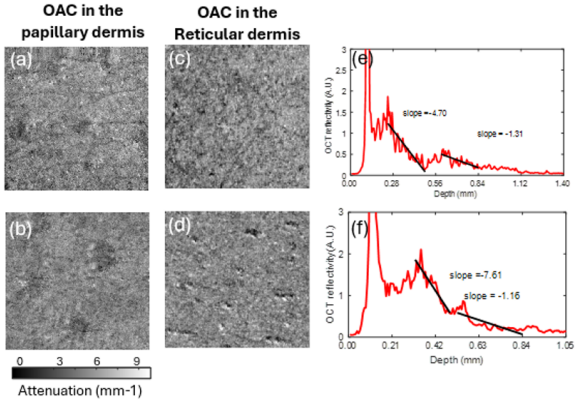

Figure 5.20: Comparison between vessel area density between the young and aged cutaneous capillaries on the forearm. (a) and (c) Capillary vasculature from the papillary dermis. (b) and (d) depth-resolved vasculature of the microvasculature among the whole depth, where the superficial vessels are color-coded in green, and the deeper vessels are color-coded in red.

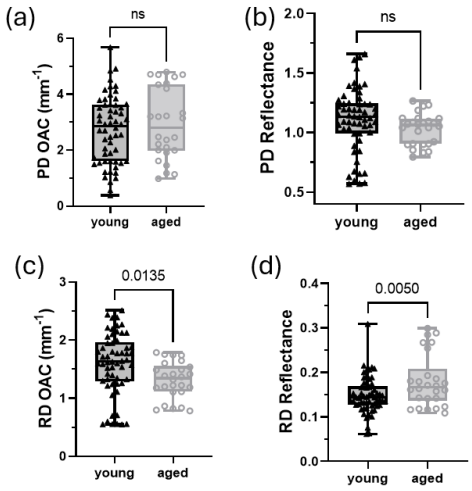

Figure 5.21: Quantification of the quantitative properties between different skin structures. (a) OAC and (b) reflectance in the papillary dermis. (c) OAC and (d) reflectance in the reticular dermis, correspondingly.

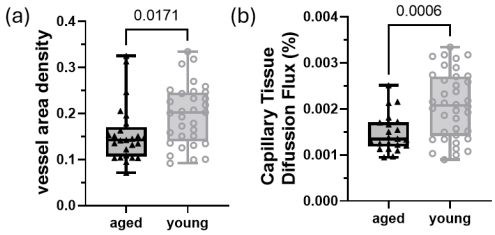

Figure 5.22: Comparative morphological quantification of the capillary bed in the skin samples tissue in aged versus young samples. (a) vessel area density in both aged and young skin samples. (b) Capillary-to-tissue diffusion flux compares the efficiency of nutrient and gas exchange between the microvasculature and surroundings.

structure that occur with aging, allowing for the precise measurement of different parameters that are not exposed externally: epidermal thickness, detection of microvascular changes, and assessment of collagen degradation in the dermis. Recent studies have demonstrated the common parameters that OCT effectively measures age-related changes: epidermal thickness[37], [170], [140], [158], reflectance contrast[170], and dermal collagen birefringence[153]typical of aged skin.

First, from our study, we observed that older skin exhibited a markedly rougher texture, including an increase in wrinkles and surface irregularities as shown in our 3D and projection maps between younger and older individuals. However, this is not necessarily expressed as an increase in epidermal thickness, which is common in unexposed areas [37], [170], [140]. While the overall thickness of the epidermis generally remains stable, a thickening effect in certain areas is often observed due to structural changes like increased collagen cross-linking and alterations in elastin fibers. With aging, there is a 30-50% slowdown in the rate of cell turnover in the epidermis, where older skin cells accumulate on the surface, leading to a rougher texture [172].

The optical attenuation coefficient (OAC) measurements further supported the change in optical properties in aged skin. The papillary dermis typically shows higher attenuation and higher scattering due to its denser collagen network and vascular structure. Conversely, the reticular dermis, which lies beneath the papillary dermis, contains a looser arrangement of collagen fibers and has a different attenuation signature. Aged skin shows a significant decrease in light attenuation and reflectivity in the reticular dermis compared to younger skin, likely due to structural and compositional degradation in skin components—such as collagen, elastin, and water content [33], [107], [40].

While the structural integrity of the epidermis remained relatively unchanged with age, the vasculature within the papillary dermis showed a significant decrease in capillary density and perfusion, as evidenced by OCTA results. These collective findings demonstrate the nature of skin aging, affecting both the visual and functional aspects of the skin. This observation is consistent with the known physiological changes that occur with aging, where reduced vascularization and an increase in skin wrinkles are associated with diminished skin health and appearance.

Aging affects the skin in complex ways: while the overall skin cell replacement gets slower in turnover, the skin composition starts to change gradually with the altered skin microcirculation within the papillary dermis impacting the skin's ability to receive essential nutrients and oxygen. This decreased vascular support not only contributes to increased wrinkle formation and impaired regenerative capabilities but also affects the skin's immune response and healing processes [172]. Thus, while the epidermis maintains its barrier function against environmental assaults, internal structural changes and diminished vascularization compromise the skin's aesthetic quality and overall health.

The principal component analysis (PCA) plot depicted provides a visual representation of the variability in skin properties among aged and young individuals, captured primarily along the first two principal components which explain 35.27% and 26.69% of the variance (together account for 61.96% of the total variance). The plot shows a clear differentiation between the aged and young groups, suggesting significant differences in skin characteristics influenced by age. The vectors on the plot, representing variables like 'VAD', 'Rho', and 'Roughness', point predominantly towards the aged cluster, indicating these features are more pronounced or variable in older skin. "VAD," "Reflectance from Reticular Dermis," and "Roughness," in particular, have a close association with the first main component (35% of the variance), in which we can determine that they may be the crucial indications of skin age.

In summary, OCT helps in understanding the pathophysiology of skin aging by visualizing how different layers of the skin change over time or in response to various treatments. We have observed degradation in the skin surface topology, composition, and microvasculature. The trends in the aging of skin can provide insights into skin health and age-related changes. They offer a non-invasive way to assess skin properties and support the ongoing development of diagnostic and monitoring tools in dermatology and cosmetic science. OCT not only provides visual insights but also allows for quantitative analysis of skin properties, such as measuring the thickness of skin layers and the density of skin capillaries but also provides quantitative data that are essential for objective, measurable benchmarks in aging studies and for correlating clinical outcomes with

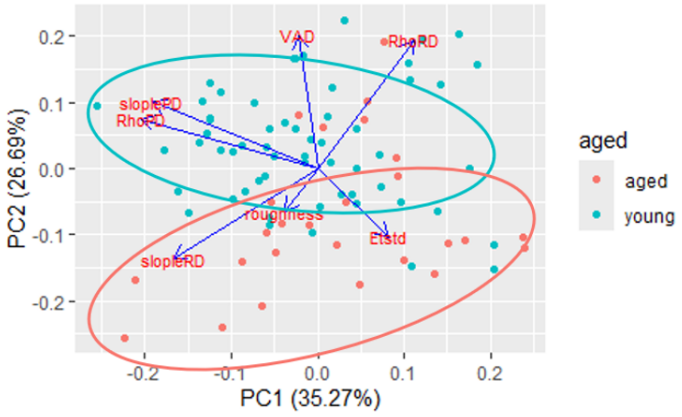

Figure 5.23: PCA plot shows the distribution of skin characteristics between aged and young individuals. Each point represents an individual subject, with aged individuals depicted in red and young individuals in blue. The ellipses encapsulate the general distribution of the aged (red) and young (blue) groups, highlighting the variation within each cohort.

physiological changes in the skin. It demonstrated the potential for researchers to quantify the effectiveness of anti-aging products or therapies. While the findings from our study using OCT provide valuable insights into the aging process of the skin, there are some limitations and areas for future research that should be acknowledged. First, the study focused on the forearm skin of a limited age range, which may not be fully generalizable to other body areas. Additionally, the study does not fully account for external factors such as long-term sun exposure, diet, lifestyle, or the use of skincare products, which can significantly affect skin aging and might confound the observed effects. Furthermore, the current SSOCT systems are also limited in their ability to quantify the effect of collagen or water content which are the major factors for light attenuation in tissue. Future studies can incorporate polarization-sensitive OCT and broad bandwidth OCT to assess the collagen and hydration status to validate the OAC map in understanding aging-related and collagen degradation.

6 Summary and Future Work

Novel functional OCT qualitative and quantitative modalities for non-invasive assessments allow early diagnostics and effective monitoring of microstructural and functional changes before clinical symptoms or detectable structural damage appear.

While the current study provides significant insights into tissue microstructure and vascular dynamics through Optical Coherence Tomography (OCT), one crucial piece of information remains underexplored: the role of collagen in tissue remodeling and scarring. Collagen deposition and structural changes are hallmarks of post-infarction remodeling and scarring, yet their impact on optical properties, such as the optical attenuation coefficient (OAC) and phase retardation, has not been fully investigated. These optical metrics could offer deeper insights into the microstructural and functional changes following myocardial infarction (MI) or tissue scarring.

This gap leads directly to the next phase of research. Future work will focus on studying OAC and phase retardation in infarcted heart tissue or collagenous tissue to characterize tissue remodeling in greater detail. Variations in OAC may reveal shifts in tissue composition, such as increased scattering due to fibrosis, while changes in phase retardation could provide quantitative measures of collagen organization and density. Together, these parameters could serve as key indicators of structural integrity and alignment in fibrous tissues.

Preliminary work has already been conducted to support this direction, as presented in this study. By leveraging OCT to analyze optical properties, the current results highlight the potential to detect subtle differences between healthy and scarred tissue regions, even when structural

damage is not visually apparent. These preliminary findings lay the foundation for future investigations aimed at correlating these optical biomarkers with physiological and pathological states. This expanded scope will enhance our ability to monitor cardiac remodeling, assess disease progression, and evaluate therapeutic interventions in cardiovascular disease.

By addressing this missing information and advancing the use of functional OCT for collagen and fibrous tissue analysis, the proposed research seeks to fill a critical gap in understanding post-infarction remodeling and support the development of targeted diagnostic and therapeutic strategies.

6.1 Summary of the Thesis

This thesis explores the versatile capabilities of Optical Coherence Tomography (OCT) and Optical Coherence Tomography Angiography (OCTA) in addressing key cardiovascular and dermatological imaging challenges. By leveraging OCT's high-resolution, non-invasive imaging capabilities, this thesis demonstrated its potential to provide both structural and functional insights, offering new pathways for diagnostics, disease monitoring, and therapeutic assessment.

6.1.1 Cardiovascular Applications

The studies presented in this thesis demonstrated the value of OCTA in assessing microvascular involvement in infarcted hearts, focusing on the structural and hemodynamic changes within the coronary microcirculation following myocardial infarction (MI). MI is a life-threatening condition that causes coronary microvascular dysregulation and heart muscle damage, significantly impacting the heart's ability to meet its metabolic needs. One of the primary characteristics of MI is capillary loss, which contributes to the progression of cardiovascular dysfunction. The microvasculature, essential for heart health by supplying oxygen and nutrients, undergoes significant remodeling and impairment during and after infarction.

To study these changes, OCTA was employed to analyze the coronary microcirculation in fixed rat hearts. The analysis revealed significant post-infarction microvascular remodeling, character-

ized by decreased capillary density, arteriole- and venule-sized vessel enlargement, and increased vascular tortuosity and complexity. Quantitative assessments of angiographic metrics, including vessel area density, vessel complexity index, vessel tortuosity index, and flow impairment, provided a detailed view of coronary microvascular health. These pathological differences, identified through OCTA, were further corroborated with histological analysis, confirming OCTA's reliability in offering qualitative and quantitative insights into coronary vascular network remodeling during disease progression and therapeutic response.

Building on these findings, the study also investigated the hemodynamic dysfunction of the microvasculature following MI, an area that remains inadequately understood due to limitations in existing methodologies. Current approaches often rely on computational models and theoretical constructs, as accurate measurement of capillary velocity in cardiac tissues has been challenging. To address these limitations, OCTA was integrated into a Langendorff perfusion setup, enabling simultaneous visualization and measurement of capillary velocities using Eigen Decomposition-based Optical Microangiography (ED-OMAG) and ED-capillary velocimetry (ED-velocimetry). This innovative approach provided detailed assessments of the vasculature and velocity maps in infarcted rat hearts.

The hemodynamic analysis revealed a 30.4% reduction in vessel area density, a 72% decline in average velocity, and a 79% decrease in perfusion index in infarcted regions compared to healthy tissue. Additionally, vascular projection images showed increased vessel tortuosity, which correlated with the mean capillary velocity in infarcted regions. These findings demonstrate significant myocardial microvascular deterioration and remodeling four weeks post-infarction, highlighting a failure to restore adequate perfusion in the affected regions.

6.1.2 Heart pulsation signal Applications

Photoplethysmography (PPG) is routinely used in clinics to detect blood pulse signals from skin tissue beds. However, the origin of the PPG signal remains controversial. The purpose of this study is to explore optical coherence tomography angiography (OCTA) to indicate pulsatile wave-

forms in the papillary plexus and dermal plexus separately under different hand elevations. Optical microangiography (OMAG) algorithm was used to obtain 3D OCTA signals, from which the depth-resolved pulsatile blood flow signals were extracted from different skin vascular plexus. The systolic amplitude, crest time, and delta T were measured from the OCTA pulsatile signals when the hand was placed at the positions of 50 cm below, 0 cm, and 50 cm above the heart level. The pulse signal integrated from all the depths is more consistent and has a similar waveform to that of the PPG. The pulsatile patterns from the papillary plexus and dermal plexus showed distinct morphological changes at different local blood pressures. Less amplitude difference was found from the papillary plexus than the dermal plexus. Crest time was found to be an increasing trend in the OCTA pulsatile waveform from both plexuses when the arm was raised from the position below to above the heart level. In contrast, a decreasing trend of Delta T was detected in the dermal pulsatile. Still, it was not observed in the papillary plexus, indicating that vascular resistance associated with the arm elevations does not necessarily have the same effect on the two plexuses. OCTA can provide depth-resolved pulsatile waveforms within different microvascular plexus within tissue skin beds. This technique could open doors to understanding the mechanisms of how blood flow changes at different skin circulatory plexus.

6.1.3 Dermatological Applications

The structure and function of human skin are important health indicators and can reveal underlying dermatological conditions. OCT provides a non-invasive, high-resolution method for assessing skin microstructure and microvascular characteristics, enabling early detection of changes due to external factors like pressure and UV exposure and intrinsic factors such as aging. This chapter examines OCT's role in capturing these changes through advanced imaging parameters, offering new insights for dermatological research, diagnostics, and personalized skincare.

Building on this foundation, accurate and repeatable skin and cutaneous measurements are key to assessing and quantifying cutaneous characteristics in dermatological research. Ultrasound and OCT are the two most common tools for non-invasive epidermis thickness assessment in

vivo. However, considering these techniques rely on contact imaging to improve imaging quality, variations in the pressure exerted on the skin can significantly affect epidermal measurements. To address this challenge, this study investigated the integration of pressure sensors into a handheld OCT probe to assess the effect of compression pressure on epidermal evaluation. By exploring the relationship between applied pressure and changes in epidermal thickness, the study found that increasing compression force leads to significant deformation of the epidermis tissue and capillary area density, with differences of up to 10% and 51%, respectively. These findings underscore the importance of controlled pressure for contact imaging, which could enhance the reliability of clinical assessments in dermatology and cosmetics.

In addition to cutaneous-related factors, UV sensitivity in human skin presents another avenue for understanding subtle microvascular and structural changes. UV exposure induces microvascular responses, such as erythema involving blood vessel dilation, even without visible redness or sunburn. Previous studies have established that UV exposure can increase the epidermis and stratum corneum's thickness. Our findings expand on this by demonstrating that OCT can detect epidermal thickening accompanied by early signs of erythema, such as vessel dilation before visible redness appears. These results highlight OCT's potential as a tool for identifying subclinical changes in the skin, enabling earlier detection and intervention. By offering a non-invasive method to capture these subtle alterations, OCT facilitates timely photoprotection strategies and improves skin health monitoring.

To further enhance OCT's capabilities, this study explored the calibration of OCT measurements for quantitative analysis of light-tissue interactions. Using Mie theory and Monte Carlo simulations, we calibrated OCT to accurately measure optical properties such as attenuation coefficient (μ) and reflectivity (ρ), validated against 100 nm polystyrene bead standards. These calibrated measurements provided new insights into light scattering in biological tissues, including the epidermis, papillary dermis, and reticular dermis. Incorporating Monte Carlo simulations allowed us to derive additional parameters, such as the reduced scattering coefficient (μ_s) and anisotropy factor (g), offering a more comprehensive understanding of tissue optical properties

across different layers. These findings advance our ability to model and interpret light-tissue interactions, enhancing OCT's potential for both quantitative and qualitative assessments.

Finally, this chapter examines the application of OCT and OCTA in studying skin aging. By leveraging OCT's high-resolution, depth-resolved imaging capabilities, we quantitatively analyzed age-related variations in skin properties on the forearm across different age groups. Parameters such as "roughness," "epidermal thickness variability," "papillary dermis reflectance," "optical attenuation coefficient," and "vessel area density" demonstrated significant differences between age groups. These metrics effectively captured microstructural and vascular changes associated with aging, highlighting the utility of OCT and OCTA for comprehensive skin assessments. The results show that OCT and OCTA are promising tools for non-invasively evaluating skin aging, providing qualitative and quantitative insights that could inform personalized skincare strategies and dermatological research.

Together, these studies illustrate the versatility and potential of OCT in dermatology, from addressing challenges in contact imaging and UV-induced changes to advancing quantitative analysis and skin aging assessments. By integrating advanced imaging parameters and calibrations, OCT continues to establish itself as an indispensable tool for non-invasive, high-resolution dermatological diagnostics.

6.1.4 Summary and Broader Implications

This thesis bridges the gap between structural imaging and functional analysis, addressing the limitations of conventional Optical Coherence Tomography (OCT), which primarily focuses on tissue morphology. Integrating functional OCT techniques—such as OCT velocimetry, OCT angiography (OCTA), and optical attenuation methods—enhances the understanding of tissue dynamics, including capillary blood flow and collagen remodeling. These advancements demonstrate OCT's potential to detect early pathological changes in both cardiac and dermatological tissues, offering quantitative biomarkers for monitoring disease progression and evaluating therapeutic interventions.

In cardiovascular applications, OCTA enables precise assessment of coronary microcirculation, providing critical insights into post-myocardial infarction (MI) care. The studies presented in this thesis illustrate how OCTA can analyze structural and functional changes in coronary microcirculation, as well as quantify microvascular perfusion velocity impairments using a Langendorff perfusion setup. These findings highlight the capability of OCTA to detect perfusion abnormalities and visualize vascular remodeling, thereby advancing non-invasive cardiovascular assessments.

In dermatological applications, this thesis explores the integration of OCT with pressure sensors to address challenges associated with contact imaging. Controlled pressure was shown to improve the accuracy and repeatability of epidermal thickness measurements, an essential parameter in dermatological and cosmetic assessments. OCT also demonstrated its ability to detect early subclinical changes in skin microvasculature and structure caused by ultraviolet (UV) exposure, such as vessel dilation and epidermal thickening, before visible erythema appears. Furthermore, OCT's quantitative parameters, including epidermal thickness, capillary density, and optical attenuation, proved effective in assessing skin aging, offering detailed insights into age-related microstructural and vascular changes.

By combining these capabilities, this work shows OCT and OCTA's transformative potential in both cardiac and dermatological diagnostics. The ability to reveal subclinical changes before detectable clinical symptoms enhances early detection and timely intervention. However, despite these advancements, the broader adoption of OCT across diverse fields is limited by its reliance on conventional structural imaging, which does not capture detailed functional insights. Addressing this gap will require the continued development of functional OCT techniques, such as OCTA and polarization-sensitive OCT, to expand its diagnostic and therapeutic applications.

In summary, this thesis demonstrates how OCT and OCTA can provide both structural and functional insights into skin and cardiovascular conditions, bridging critical gaps in current imaging methodologies. By advancing functional imaging and introducing quantitative modalities, this work establishes a foundation for future innovations to address unmet clinical needs and expand the utility of OCT in diverse medical fields.

6.2 Future Work: Leveraging Polarization-Sensitive Optical Coherence Tomography (PS-OCT) for Non-Invasive Assessment of UV-induced change in skin

While the current study provides significant insights into microvascular dynamics and tissue characteristics, one critical piece of information remains underexplored: the role of collagen and its structural organization in disease progression and tissue remodeling. Collagen is a key component of the extracellular matrix, and its degradation or reorganization is central to conditions such as myocardial infarction, skin aging, and UV-induced damage. The future direction of this thesis focuses on incorporating quantitative measurements of collagen, such as phase retardation, birefringence properties, and optical attenuation properties, which are particularly suited for polarization-sensitive OCT (PS-OCT).

Previous study has already demonstrated the feasibility of using PS-OCT to detect changes in optical attenuation coefficients and phase retardation in collagen-rich tissues. These results indicate that PS-OCT can provide complementary information about tissue microstructure and collagen integrity. By expanding the focus to include collagen-specific imaging, future studies can bridge the gap in understanding structural and functional changes, enabling a more comprehensive assessment of tissue health and pathology. This approach will advance the diagnostic and therapeutic applications of OCT and functional OCT techniques, offering deeper insights into the interplay between microvascular dynamics and collagen remodeling.

6.2.1 Introduction

Skin is a critical barrier against environmental factors, with its layered structure of epidermis, dermis, and hypodermis providing both protection and resilience. The dermis, in particular, contains extracellular matrix (ECM) components like collagen and elastin, which give skin its structural integrity and elasticity. However, exposure to ultraviolet (UV) light poses a significant threat to skin health, inducing oxidative stress, inflammation, and collagen degradation. Prolonged UV expo-

sure leads to collagen fragmentation and disruption of fiber arrangement, accelerating skin aging and weakening its protective capabilities.

The effects of different wavelengths of light on the skin vary significantly, impacting both short-term and long-term skin health. UVB light, part of the ultraviolet spectrum, is highly erythemogenic, causing redness and inflammation due to its stimulating inflammatory mediators like cytokines, histamines, and prostaglandins. In contrast, UVA light penetrates deeper into the skin. It can trigger immediate erythema and delayed effects that may appear after 6 hours, causing vasodilation and increased blood flow through the release of nitric oxide. Visible light (VL) at high doses also induces erythema, which usually resolves within 2 hours. This effect results from the interaction with chromophores in the skin, leading to heat generation and subsequent vasodilation. Infrared (IR) light primarily has a thermal effect, with erythema lasting for less than an hour due to heat-induced vasodilation.

Optical imaging techniques have proven valuable for studying skin's layered architecture, especially in detecting collagen-related changes often seen in skin burns and photo-aging conditions. Polarization-sensitive optical coherence tomography (PS-OCT) is a particularly promising approach, as it combines standard structural imaging with birefringence information by detecting the polarization state of reflected light within tissues. This birefringence property highlights the presence and orientation of collagen fibers, making PS-OCT a useful tool for examining collagen integrity in various dermatological applications.

In addition to phase retardation, the optical attenuation coefficient (OAC) measured by PS-OCT provides valuable information about skin structural variations, particularly regarding collagen content. The OAC reflects the degree to which light is scattered and absorbed as it travels through skin layers, with higher values often indicating denser or more organized tissue structures, such as healthy collagen networks. OAC changes can reveal skin architecture alterations, including collagen degradation or fragmentation due to UV exposure or aging. By capturing these subtle structural differences, OAC measurements offer another non-invasive avenue to assess collagen integrity and skin health, complementing phase retardation metrics and enhancing PS-OCT's

capability to monitor early-stage collagen changes related to environmental damage or intrinsic aging processes.

This chapter leverages optical attenuation coefficient (OAC) and phase retardation measurements through Polarization-Sensitive Optical Coherence Tomography (PSOCT) to assess subsurface changes in skin structure following UV exposure. By capturing these two complementary metrics, PSOCT provides a detailed view of structural alterations, particularly in collagen content and organization, which are critical markers of skin health. Importantly, this approach allows for the non-invasive, early detection of erythema and collagen degradation—before visible symptoms arise—offering a sensitivity that surpasses traditional clinical methods. This work highlights the potential of PSOCT as an advanced tool for dermatological research, enabling more precise assessments of UV-induced damage and other environmental impacts on skin health.

6.2.2 Methods

Study Design and UV Exposure Protocol

This study aimed to investigate the effects of UV exposure on collagen structure in human skin, focusing on phase retardation and optical attenuation coefficient (OAC) measurements using Polarization-Sensitive Optical Coherence Tomography (PSOCT). Skin samples were exposed to varying doses of UV radiation, ranging from sub-minimal erythema doses (sub-MED) to multiple minimal erythema doses (MED), to evaluate collagen changes under controlled conditions. The UV doses used were 0.6, 0.9, 1.4, 2.1, 3.0, and 3.5 MED, administered to different regions of the skin. Baseline measurements were obtained before UV exposure, followed by post-exposure measurements on days 1, 2, 3, 6, and 8.

In 6.1, we observe the effects of varying UV doses on skin pigmentation and erythema, assessed through RGB imaging, Individual Typology Angle (ITA) mapping, and Redness mapping at baseline and 24 hours post-exposure. The six marked positions (P1–P6), receiving incremental UV doses from 0.622 to 3.5 MED, display progressively increased pigmentation and erythema responses with higher doses. At baseline, all areas appear relatively uniform with minimal visi-

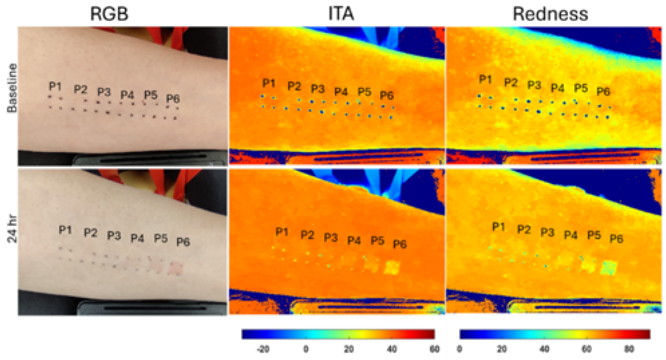

Position	UV dosage [MED]
P1	0.622
P2	0.933
P3	1.4
P4	2.1
P5	3.0
P6	3.5

Figure 6.1: Baseline and 24-hour post-UV exposure assessment of skin color changes across different UV doses. The RGB images (left column) show visible skin responses, while the Individual Typology Angle (ITA) and Redness maps (middle and right columns) provide quantitative evaluations of pigmentation and erythema, respectively. The six labeled positions (P1–P6) correspond to UV doses ranging from 0.622 to 3.5 MED, as shown in the adjacent table. The ITA and Redness maps highlight the increase in pigmentation and erythema after 24 hours, with higher UV doses producing more pronounced responses.

ble erythema. However, 24 hours after UV exposure, distinct changes are evident, particularly in the higher dose positions (P4–P6), where visible erythema and increased redness are prominent. The ITA and Redness maps provide a quantitative measure of these changes, with the ITA map indicating a reduction in pigmentation and the Redness map showing a dose-dependent increase in erythema. These results highlight the sensitivity of ITA and Redness metrics in detecting early skin responses to UV exposure, especially in higher dosages, where erythema is markedly enhanced.

Phase retardation

Phase retardation is calculated by measuring the difference in the phase of light as it passes through birefringent tissues, like collagen-rich skin layers. As polarized light interacts with the organized collagen fibers, it undergoes phase shifts depending on the tissue's optical properties. PSOCT captures these shifts by detecting the changes in polarization states as light reflects back from the sample. By comparing the polarization states across depth-resolved layers, the phase retardation can be quantified, providing a metric that reflects collagen content and organization within the

tissue. This parameter is particularly useful for assessing structural changes in collagen, such as those induced by UV exposure or aging.

Optical Attenuation Coefficient (OAC) Analysis

The optical attenuation coefficient (OAC) was calculated for each skin region to evaluate changes in tissue composition and scattering properties. OAC, which reflects the absorption and scattering characteristics of the tissue, was derived by analyzing the intensity decay of OCT signals with depth. Baseline OAC values were recorded prior to UV exposure, with subsequent measurements taken post-UV exposure at the designated time points to observe variations due to collagen degradation or remodeling.

6.2.3 Results

Following UV exposure, both phase retardation and optical attenuation coefficient (OAC) changes were tracked to assess structural alterations in the skin's collagen. 6.2 displays the changes in phase retardation in skin tissue following varying doses of UV exposure, ranging from 0.6 to 3.5 minimum erythema doses (MED). Each row represents a different UV dose, while each column represents different time points post-exposure: Baseline (pre-exposure), Day 1 (D1), Day 2 (D2), Day 3 (D3), Day 6 (D6), and Day 8 (D8). The color scale on the right denotes the phase retardation values in degrees, with blue indicating lower and red indicating higher phase retardation.

Higher UV doses result in increased phase retardation immediately post-exposure, suggesting changes in collagen organization and structure within the skin. Over time, especially by Day 8, the phase retardation values tend to stabilize and decrease slightly, indicating a potential recovery in collagen structure or adaptation of the skin to UV-induced stress. The variation in color intensity across time points provides insight into how skin collagen responds dynamically to both the dose and duration post-exposure, with higher doses generally leading to more pronounced changes and slower recovery.

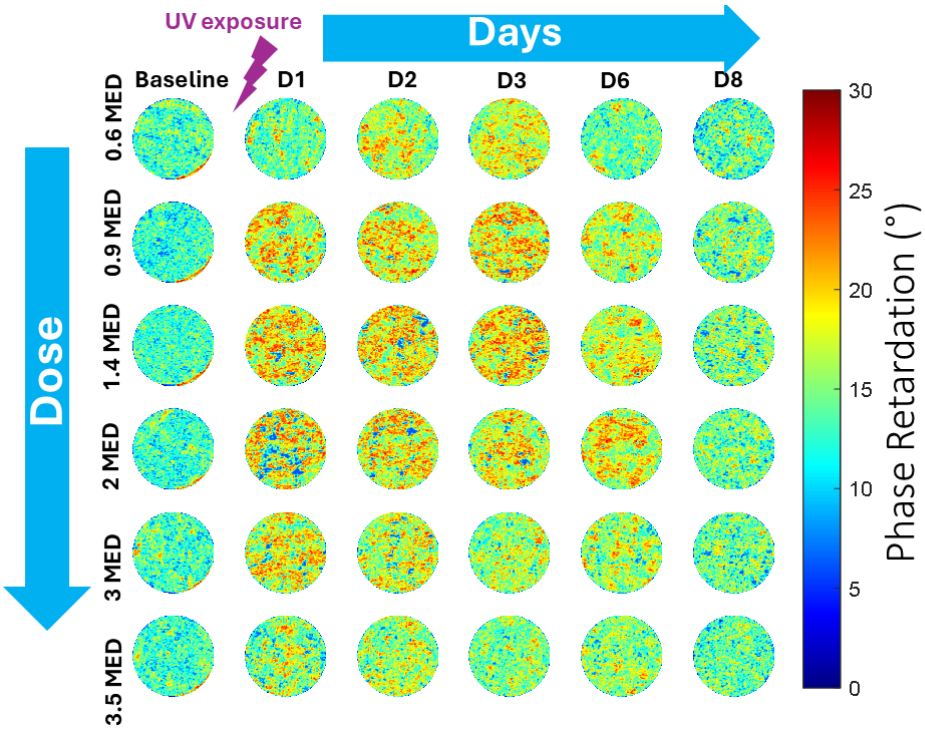

Figure 6.2: Phase retardation maps of skin samples over time following exposure to varying UV doses, ranging from 0.6 to 3.5 Minimum Erythema Doses (MED). Columns represent different time points: baseline, Day 1 (D1), Day 2 (D2), Day 3 (D3), Day 6 (D6), and Day 8 (D8) post-exposure. Rows correspond to increasing UV exposure levels (in MED). Each map uses a color scale to indicate the degree of phase retardation, with values ranging from 0° (blue) to 30° (red), representing changes in collagen birefringence within the dermal layer. Higher phase retardation values, observed as warmer colors, suggest increased collagen disorganization or degradation. This figure illustrates how both the intensity and duration of UV exposure impact collagen structure within the skin over time.

6.3a shows the phase retardation data over an 8-day period across three UV dosage groups: sub-1 MED (blue circles), >1 MED (red squares), and >2 MED (green triangles).

In the >1 MED and >2 MED groups, phase retardation initially increased, peaking around day 2 or day 3. This early increase suggests UV-induced changes in collagen birefringence, potentially due to structural modifications within the collagen matrix. The sub-1 MED group showed minimal change in phase retardation, indicating that lower doses of UV exposure may not cause significant collagen alterations.

In 6.3b, the change in optical attenuation coefficient (ΔOAC) over time reveals a dose-dependent effect. Higher UV dosages (>2 MED) resulted in a marked decrease in OAC, particularly in the initial days following exposure. This reduction in OAC suggests an alteration in skin microstructure, which may correspond to UV-induced collagen fragmentation or tissue degradation. The sub-1 MED group showed minimal changes in ΔOAC.

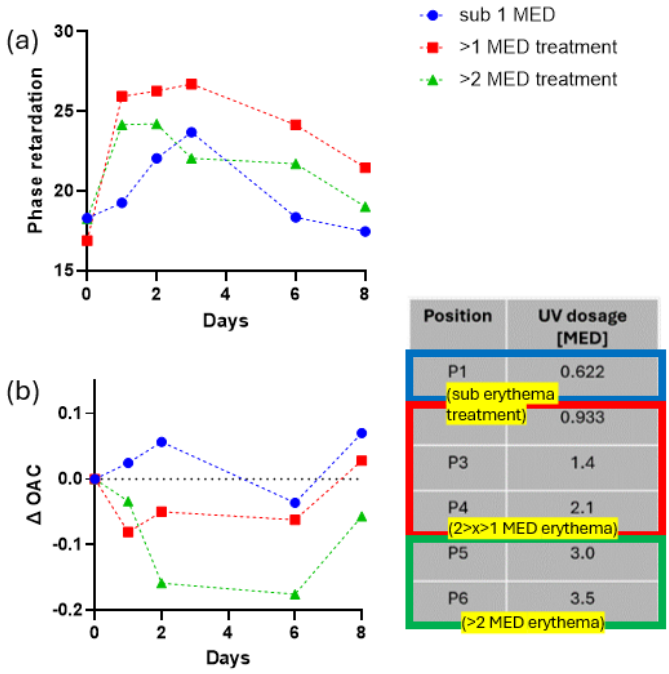

Figure 6.3: (a) Phase retardation measurements over time for different UV dosage groups following UV exposure. The groups are categorized by UV dosage: sub-1 MED (blue circles), >1 MED (red squares), and >2 MED (green triangles).(b) Change in Optical Attenuation Coefficient (ΔOAC) over time across the same UV dosage groups. The accompanying table lists the UV dosages (in MED) applied to each position, categorized as sub-erythema treatment (P1), erythema range (>1 MED) treatments (P2 and P3), and high-dosage (>2 MED) treatments (P4, P5, and P6). The color-coded boxes correlate with each dosage category shown in the plots.

6.2.4 Conclusion and Discussion

This study used Polarization-Sensitive Optical Coherence Tomography (PS-OCT) to evaluate changes in collagen structure in human skin following UV exposure by measuring phase retar-

dation and optical attenuation coefficient (OAC). The findings demonstrate that PS-OCT is sensitive to early UV-induced structural alterations in the skin, providing a valuable, non-invasive method for monitoring collagen degradation and changes in collagen organization. The increase in phase retardation observed in higher UV dosage groups (>1 MED) suggests collagen fiber disorganization or structural modification, while the decrease in OAC at high doses (>2 MED) indicates potential fragmentation and loss of collagen integrity.

These results align with established knowledge on UV-induced skin damage, where prolonged UV exposure induces oxidative stress, inflammation, and collagen degradation, contributing to skin aging and structural deterioration. The study adds to this body of knowledge by demonstrating that PS-OCT can quantify these microstructural changes non-invasively and in real time. Additionally, the dose-dependent response observed in both phase retardation and OAC indicates that PS-OCT metrics may be useful for differentiating between subclinical and more advanced stages of UV damage.

6.4 demonstrates the dynamic structural changes in collagen fibers under different physiological and environmental conditions—erythema, normal, and heated states. Under normal conditions, collagen fibers are tightly and uniformly organized, providing the skin with essential strength, elasticity, and resilience against environmental stress. This well-arranged collagen structure is vital for maintaining a youthful and healthy appearance, serving as a baseline for evaluating any structural changes caused by external factors.

When exposed to UV light, the skin enters an erythema state, where inflammation and oxidative stress cause collagen fibers to separate. Water molecules and inflammatory mediators infiltrate the collagen matrix, disrupting its organization and leading to visible redness. This separation weakens the skin's structural integrity, potentially accelerating aging if UV exposure is repeated or prolonged. In response to heating, collagen fibers contract and tighten, resulting in a denser structure. This thermal effect is often used in skin treatments to improve firmness and reduce wrinkles. Controlled heating promotes collagen contraction and reorganization, enhancing skin elasticity; however, excessive heat can risk collagen damage. These collagen transformations—normal

organization, separation with erythema, and tightening through heating—underscore the skin's adaptability and provide insights for optimizing dermatological treatments and protective measures.

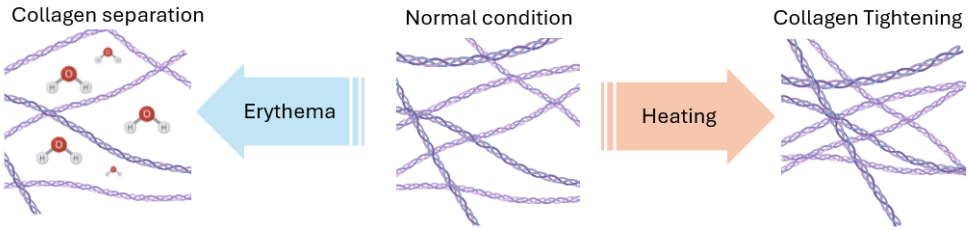

Figure 6.4: Illustration of collagen fiber arrangement in different skin states.

Despite the promising results, this study acknowledges several limitations in the use of PS-OCT for evaluating UV-induced collagen changes in skin. First, PS-OCT faces challenges in capturing the complex structure of skin, where collagen fibers are intricately arranged across multiple layers with varying orientations. This layered complexity makes it difficult to accurately quantify collagen changes, particularly for subtle structural alterations that fall below the system's resolution. Additionally, the heterogeneity in collagen distribution across different skin regions further complicates PS-OCT imaging, as variations in collagen density and orientation can influence the interpretation of results, especially when assessing localized UV-induced changes.

Another significant limitation is the need to establish a robust correlation between the phase retardation values obtained from PS-OCT and the actual collagen content in the skin. While previous studies have shown that collagen organization affects PS-OCT phase retardation measurements in heart tissues, further research is essential to confirm and quantify this relationship specifically for the skin. Validating this correlation would enhance the interpretability of phase retardation as an indicator of collagen degradation or synthesis, enabling more accurate assessments of UV-induced damage in the skin.

Bibliography

1. G. Abignano et al. “Virtual skin biopsy by optical coherence tomography: The first quantitative imaging biomarker for scleroderma”. *Ann Rheum Dis* 72:11, 2013, pp. 1845–1851. DOI: 10.1136/annrheumdis-2012-202682.

2. M. Abrouk, C. Gianatasio, Y. Li, J. Holmes, and J. Dong. *An Atlas of Optical Coherence Tomography (OCT): Elucidating In Vivo Differences of Scar Types Using OCT in Order to Guide Laser Treatment Parameters*. 2022.

3. e. a. Ahmed Ibrahim. “Multi-Models of Analyzing Dermoscopy Images for Early Detection of Multi-Class Skin Lesions Based on Fused Features”. *Processes* 11:3, 2023, p. 910. DOI: 10.3390/pr11030910.

4. S. Ahn, J. Yoon, and P. Kim. “Intravital imaging of cardiac tissue utilizing tissue-stabilized heart window chamber in live animal model”. *European Heart Journal - Imaging Methods and Practice* 2, 2024. DOI: 10.1093/ehjimp/qyae062.

5. C. L. C. et al. “Peripapillary retinal nerve fiber layer vascular microcirculation in eyes with glaucoma and single-hemifield visual field loss”. *JAMA Ophthalmol* 135:5, 2017, pp. 461–468. DOI: 10.1001/jamaophthalmol.2017.0261.

6. D. M. et al. “Heart disease and stroke statistics-2016 update a report from the American Heart Association”. *Circulation* 133:4, 2016. DOI: 10.1161/CIR.0000000000000350.

7. F. B. et al. "'Small Blood Vessels: Big Health Problems?': Scientific Recommendations of the National Institutes of Health Workshop". *J. Am. Heart Assoc.* 5:11, 2016, e004389. DOI: 10.1161/JAHA.116.004389.

8. G. H. et al. "Cardiovascular remodelling in coronary artery disease and heart failure". *The Lancet* 383:9932, 2014, pp. 1933–1943. DOI: 10.1016/S0140-6736(14)60107-0.

9. I. N. et al. "3D imaging in CUBIC-cleared mouse heart tissue: going deeper". *Biomed Opt Express* 7:9, 2016, p. 3716. DOI: 10.1364/boe.7.003716.

10. J. L. et al. "Vascular remodeling after ischemic stroke: Mechanisms and therapeutic potentials". *Progress in Neurobiology* 115, 2014, pp. 138–156. DOI: 10.1016/j.pneurobio.2013.11.004.

11. J. X. et al. "Scalable wide-field optical coherence tomography-based angiography for in vivo imaging applications". *Biomed Opt Express* 7:5, 2016, p. 1905. DOI: 10.1364/boe.7.001905.

12. K. A. V. et al. "Depth-resolved model-based reconstruction of attenuation coefficients in optical coherence tomography". *Biomedical Optics Express* 5:1, 2013, pp. 322–337.

13. K. V. L. et al. *Noninvasive Blood Glucose Monitoring With Optical Coherence Tomography: A pilot study in human subjects*. Available online. URL: http://diabetesjournals.org/care/article-pdf/25/12/2263/646548/dc1202002263.pdf.

14. M. A. R. et al. "Patterned human microvascular grafts enable rapid vascularization and increase perfusion in infarcted rat hearts". *Nat Commun* 10:1, 2019. DOI: 10.1038/s41467-019-08388-7.

15. P. G. et al. "Deciphering microvascular changes after myocardial infarction through 3D fully automated image analysis". *Sci Rep* 8:1, 2018. DOI: 10.1038/s41598-018-19758-4.

16. P. J. M. et al. "Imaging of cortical structures and microvasculature using extended-focus optical coherence tomography at 13 um". *Opt Lett* 43:8, 2018, p. 1782. DOI: 10.1364/ol.43.001782.

17. Q. Z. et al. “Projection Artifact Removal Improves Visualization and Quantitation of Macular Neovascularization Imaged by Optical Coherence Tomography Angiography”. *Ophthalmol Retina* 1:2, 2017, pp. 124–136. DOI: 10.1016/j.oret.2016.08.005.

18. S. D. et al. “A Unique Collateral Artery Development Program Promotes Neonatal Heart Regeneration”. *Cell* 176:5, 2019, 1128–1142.e18. DOI: 10.1016/j.cell.2018.12.023.

19. S. F. M. et al. “Contemporaneous 3D characterization of acute and chronic myocardial I/R injury and response”. *Nat Commun* 10:1, 2019. DOI: 10.1038/s41467-019-10338-2.

20. Z. C. et al. “Quantitative assessment of the retinal microvasculature using optical coherence tomography angiography”. *J Biomed Opt*, 2016. DOI: 10.1117/1.jbo.21.6.066008.

21. J. Allen. “Photoplethysmography and its application in clinical”. *Physiol. Meas.* 28:3, 2007, R1–R39. DOI: 10.1088/0967-3334/28/3/R01.

22. J. Allen and A. Murray. “Modelling the relationship between peripheral blood pressure and blood volume pulses using linear and neural network system identification techniques”. *Physiol. Meas.* 20:3, 1999, pp. 287–301. DOI: 10.1088/0967-3334/20/3/306.

23. M. Almasian, N. Bosschaart, T. Leeuwen, and D. Faber. “Validation of quantitative attenuation and backscattering coefficient measurements by optical coherence tomography in the concentration-dependent and multiple scattering regime”. *Journal of Biomedical Optics* 20:12, 2015, p. 121314.

24. N. E. Almond, D. P. Jones, and E. D. Cooke. “Noninvasive Measurement of the Human Peripheral Circulation: Relationship Between Laser Doppler Flowmeter and Photoplethysmograph Signals from the Finger”. *Angiology* 39:9, 1988, pp. 819–829. DOI: 10.1177/000331978803900906.

25. L. An, J. Qin, and R. Wang. “Ultrahigh sensitive optical microangiography for in vivo imaging of microcirculations within human skin tissue beds”. *Optics Express* 18, 2010, p. 8220. DOI: 10.1364/oe.18.008220.

26. L. An and R. Wang. “In vivo volumetric imaging of vascular perfusion within human retina and choroids with optical micro-angiography”. *Optics Express* 16, 2008, p. 11438. DOI: 10.1364/oe.16.011438.

27. L. An and R. K. Wang. “In vivo volumetric imaging of vascular perfusion within human retina and choroids with optical micro-angiography”. *Opt Express* 16:15, 2008, p. 11438. DOI: 10.1364/oe.16.011438.

28. G. Angius, D. Barcellona, E. Cauli, L. Meloni, and L. Raffo. “Myocardial infarction and Antiphospholipid Syndrome: A first study on finger PPG waveforms effects”. In: *Comput. Cardiol. (2010)*. Vol. 2012. 2012, pp. 517–520.

29. e. a. Aumann Silke. “Optical Coherence Tomography (OCT): Principle and Technical Realization”. In: *High Resolution Imaging in Microscopy and Ophthalmology: New Frontiers in Biomedical Optics*. Springer, 2019, pp. 59–85.

30. K. Avanaki, A. Podoleanu, J. Schofield, C. Jones, M. Sira, Y. Liu, and A. Hojjat. “Quantitative evaluation of scattering in optical coherence tomography skin images using the extended Huygens–Fresnel theorem”. *Applied Optics* 52:8, 2013, p. 1574.

31. K. M. K. B. F. Kennedy and D. D. Sampson. “Optical Coherence Elastography”. *Opt. Photon. News* 26:4, 2015, pp. 32–39. DOI: 10.1364/OPN.26.4.000032.

32. K. A. E.-M. B. S. Atiyeh and R. Dham. “Scar quality and physiologic barrier function restoration after moist and moist-exposed dressings of partial-thickness wounds”. *Dermatologic Surgery* 29:1, 2003, pp. 14–20. DOI: 10.1046/j.1524-4725.2003.29002.x.

33. O. Babalola, A. Mamalis, H. Lev-Tov, and J. Jagdeo. “Optical coherence tomography (OCT) of collagen in normal skin and skin fibrosis”. *Archives of Dermatological Research* 306:1, 2014, pp. 1–9. DOI: 10.1007/s00403-013-1417-7.

34. A. M. Băbțan et al. “High-frequency ultrasound assessment of skin and oral mucosa in metabolic syndrome patients—A cross-sectional study”. *J Clin Med* 10:19, 2021. DOI: 10.3390/jcm10194461.

35. Z. Bahadir, E. Tisdell, A. A. A. Esquivel, D. A. Dobrosielski, and M. A. Welsch. “Influence of venous emptying on the reactive hyperemic blood flow response”. *Dyn. Med.* 6:3, 2007, pp. 1–7. DOI: 10.1186/1476-5918-6-3.

36. U. Baran, L. Shi, and R. Wang. “Capillary blood flow imaging within human finger cuticle using optical microangiography”. *Journal of Biophotonics* 8, 2015, pp. 46–51. DOI: 10.1002/jbio.201300154.

37. I. Besné, C. Descombes, and L. Breton. “Effect of Age and Anatomical Site on Density of Sensory Innervation in Human Epidermis”.

38. C. F. Bohren and D. R. Huffman. *Absorption and Scattering of Light by Small Particles*. Wiley, 1983.

39. M. Boric, I. Skopljanac, L. Ferhatovic, A. J. Kadic, A. Banozic, and L. Puljak. “Reduced epidermal thickness, nerve degeneration and increased pain-related behavior in rats with diabetes type 1 and 2”. *J Chem Neuroanat* 53, 2013, pp. 33–40. DOI: 10.1016/J.JCHEMNEU.2013.10.001.

40. M. C. Branchet, S. Boisnic, C. Frances, C. Lesty, and L. Robert. *Morphometric analysis of dermal collagen fibers in normal human skin as a function of age*. 1991.

41. I. M. Braverman. “The cutaneous microcirculation”. *J. Investig. Dermatology Symp. Proc.* 5:1, 2000, pp. 3–9. DOI: 10.1046/j.1087-0024.2000.00010.x.

42. A. L. Bui, T. B. Horwich, and G. C. Fonarow. “Epidemiology and risk profile of heart failure”. *Nat Rev Cardiol* 8:1, 2011, pp. 30–41. DOI: 10.1038/nrcardio.2010.165.

43. G. Buist, J. Kuebler, J. Fischer, A. Amelink, and J. F. de Boer. “Validation of OCT Monte Carlo simulations by optical phantom OCT measurements”. In: *European Conference on Biomedical Optics*. Optica Publishing Group. 2023.

44. E. Bullitt, C. H. Nc, W. Lin, and S. R. Aylward. “Measuring Tortuosity of the Intracerebral Vasculature from MRA”. 22:9, 2008, pp. 1163–1171. DOI: 10.1109/TMI.2003.816964.

45. A. Burkert, A. Scholze, and M. Tepel. “Noninvasive continuous monitoring of digital pulse waves during hemodialysis”. *ASAIO J.* 52:2, 2006, pp. 174–179. DOI: 10.1097/01.mat.0000199892.82612.8e.

46. G. Caiazzo and E. Navarese. “State of the Art: No-Reflow Phenomenon”. *Cardiology Clinics* 38, 2020, pp. 563–573.

47. P. G. Camici, C. Tschöpe, M. F. D. Carli, O. Rimoldi, and S. V. Linthout. “Coronary microvascular dysfunction in hypertrophy and heart failure”. *Cardiovascular Research* 116:4, 2020, pp. 806–816. DOI: 10.1093/cvr/cvaa023.

48. P. Camici, C. Tschöpe, M. Di Carli, O. Rimoldi, and S. Van Linthout. “Coronary microvascular dysfunction in hypertrophy and heart failure”. *Cardiovascular Research* 116, 2020, pp. 806–816.

49. T. M. Cannon, B. E. Bouma, and N. Uribe-Patarroyo. “Layer-based, depth-resolved computation of attenuation coefficients and backscattering fractions in tissue using optical coherence tomography”. *Biomedical Optics Express* 12:8, 2021, pp. 5037–5056.

50. S. Chang and A. K. Bowden. “Review of methods and applications of attenuation coefficient measurements with optical coherence tomography”. *Journal of Biomedical Optics* 24:9, 2019, p. 090901.

51. C. Chen and R. K. Wang. “Optical coherence tomography based angiography [Invited]”. *Biomed Opt Express* 8, 2017, pp. 1056–1082. DOI: 10.1364/BOE.8.001056.

52. C.-L. Chen and R. K. Wang. “Optical coherence tomography based angiography [Invited]”. *Biomed Opt Express* 8:2, 2017, pp. 1056–1082. DOI: 10.1364/boe.8.001056.

53. E. Chirikhina, A. Chirikhin, S. Dewsbury-Ennis, F. Bianconi, and P. Xiao. “Skin characterizations by using contact capacitive imaging and high-resolution ultrasound imaging with machine learning algorithms”. *Applied Sciences (Switzerland)* 11:18, 2021. DOI: 10.3390/app11188714.

54. W. Choi, Y. Li, W. Qin, and R. Wang. “Cerebral capillary velocimetry based on temporal OCT speckle contrast”. *Biomedical Optics Express* 7, 2016, p. 4859. DOI: 10.1364/boe.7.004859.

55. Z. Chu et al. “Quantitative assessment of the retinal microvasculature using optical coherence tomography angiography”. *J Biomed Opt*, 2016. DOI: 10.1117/1.jbo.21.6.066008.

56. G. Crystal and P. Pagel. “Right Ventricular Perfusion: Physiology and Clinical Implications”. *Anesthesiology* 128, 2018, pp. 202–218.

57. C. H. Daly and G. F. “Age-related Changes in the Mechanical Properties of Human Skin”, 1979.

58. A. Deegan, J. Lu, R. Sharma, S. Mandell, and R. Wang. “Imaging human skin autograft integration with optical coherence tomography”. *Quantitative Imaging in Medicine and Surgery* 11, 2021, pp. 784–796. DOI: 10.21037/QIMS-20-750.

59. L. A. DiPietro. “Angiogenesis and wound repair: when enough is enough”. *J Leukoc Biol* 100:5, 2016, pp. 979–984. DOI: 10.1189/jlb.4mr0316-102r.

60. A. Dubois et al. “Line-field confocal optical coherence tomography for high-resolution noninvasive imaging of skin tumors”. *J Biomed Opt* 23:10, 2018, p. 1. DOI: 10.1117/1.jbo.23.10.106007.

61. A. Dubois et al. “Line-field confocal optical coherence tomography for high-resolution noninvasive imaging of skin tumors”. *J Biomed Opt* 23:10, 2018, p. 1. DOI: 10.1117/1.jbo.23.10.106007.

62. e. a. F. M. Hendriks. “A numerical-experimental method to characterize the non-linear mechanical behavior of human skin”. *Skin Research and Technology* 9:3, 2003, pp. 274–283. DOI: 10.1034/j.1600-0846.2003.00019.x.

63. D. J. Faber, F. J. van der Meer, M. C. Aalders, and T. G. van Leeuwen. “Quantitative measurement of attenuation coefficients of weakly scattering media using optical coherence tomography”. *Optics Express* 12:19, 2004, pp. 4353–4365.

64. G. Fibich, Y. Lanir, N. Liron, and M. Abovsky. “Modeling of coronary capillary flow”.

65. A. F. Frangi, W. J. Niessen, K. L. Vincken, and M. A. Viergever. “Multiscale Vessel Enhancement Filtering”. *Med Image Anal*, 1998.

66. V. Fuster, B. B. Kelly, and R. Vedanthan. “Global cardiovascular health: Urgent need for an intersectoral approach”. *J Am Coll Cardiol* 58:12, 2011, pp. 1208–1210. DOI: 10.1016/j.jacc.2011.05.038.

67. C. G. G. Lee and A. R. Pirkle. “Specificity of noninvasive blood glucose sensing using optical coherence tomography technique: a pilot study”, 2003.

68. F. M. Gabhann and S. M. Peirce. “Collateral capillary arterialization following arteriolar ligation in murine skeletal muscle”. *Microcirculation* 17:5, 2010, pp. 333–347. DOI: 10.1111/j.1549-8719.2010.00034.x.

69. B. Ghosh, M. Mandal, P. Mitra, and J. Chatterjee. “Attenuation corrected-optical coherence tomography for quantitative assessment of skin wound healing and scar morphology”. *Journal of Biophotonics* 14:4, 2021, e202000357.

70. P. Gkontra and A. Arroyo. “Deciphering microvascular changes after myocardial infarction through 3D fully automated image analysis”. *Scientific Reports* 8, 2018, pp. 1–19.

71. P. Gong et al. “In vivo label-free lymphangiography of cutaneous lymphatic vessels in human burn scars using optical coherence tomography”. *Biomed Opt Express* 7:12, 2016, p. 4886. DOI: 10.1364/boe.7.004886.

72. P. Gong et al. “In vivo label-free lymphangiography of cutaneous lymphatic vessels in human burn scars using optical coherence tomography”. *Biomed Opt Express* 7:12, 2016, p. 4886. DOI: 10.1364/boe.7.004886.

73. P. Gong, M. Almasian, G. van Soest, D. M. de Bruin, T. G. van Leeuwen, D. D. Sampson, and D. J. Faber. “Parametric imaging of attenuation by optical coherence tomography: review of models, methods, and clinical translation”. *Journal of Biomedical Optics* 25:4, 2020, p. 040901.

74. O. A. Grishina, S. Wang, and I. V. Larina. "Speckle variance optical coherence tomography of blood flow in the beating mouse embryonic heart". *J Biophotonics* 10:5, 2017, pp. 735–743. DOI: 10.1002/jbio.201600293.

75. V. Hartmann, H. Liu, F. Chen, Q. Qiu, S. Hughes, and D. Zheng. "Quantitative comparison of photoplethysmographic waveform characteristics: Effect of measurement site". *Front. Physiol.* 10:198, 2019, pp. 1–8. DOI: 10.3389/fphys.2019.00198.

76. F. Henry, C. Piérard-Franchimont, G. Cauwenbergh, and G. E. Piérard. "Age-related changes in facial skin contours and rheology". *J Am Geriatr Soc* 45:2, 1997, pp. 220–222. DOI: 10.1111/j.1532-5415.1997.tb04512.x.

77. G. Heusch and L. Opie. "Cardiovascular remodelling in coronary artery disease and heart failure". *The Lancet* 383, 2014, pp. 1933–1943. DOI: 10.1016/S0140-6736(14)60107-0.

78. M. Hickey, J. P. Phillips, and P. A. Kyriacou. "Investigation of peripheral photoplethysmographic morphology changes induced during a hand-elevation study". *J. Clin. Monit. Comput.* 30:5, 2016, pp. 727–736. DOI: 10.1007/s10877-015-9761-0.

79. M. Hickey, J. P. Phillips, and P. A. Kyriacou. "The effect of vascular changes on the photoplethysmographic signal at different hand elevations". *Physiol. Meas.* 36:3, 2015, pp. 425–440. DOI: 10.1088/0967-3334/36/3/425.

80. C. Honig and C. Odoroff. "Calculated dispersion of capillary transit times: significance for oxygen exchange". *Journal Name*.

81. J. Hope, M. Goodwin, and F. Vanholsbeeck. "Inverse spectroscopic optical coherence tomography (IS-OCT) for characterization of particle size and concentration". *OSA Continuum* 4:8, 2021, p. 2260.

82. T. P. J. Sandby-Møller and H. C. Wulf. "Epidermal Thickness at Different Body Sites: Relationship to Age, Gender, Pigmentation, Blood Content, Skin Type and Smoking Habits". *Acta Derm Venereol* 83:6, 2003, pp. 410–413. DOI: 10.1080/00015550310015419.

83. e. a. J. Wang. "THz in vivo measurements: the effects of pressure on skin reflectivity". *Biomed Opt Express* 9:12, 2018, p. 6467. DOI: 10.1364/boe.9.006467.

84. e. a. J. Xu. "Scalable wide-field optical coherence tomography-based angiography for in vivo imaging applications". *Biomed Opt Express* 7:5, 2016, p. 1905. DOI: 10.1364/boe.7.001905.

85. e. a. J. Xu W. Wei. "Scalable wide-field optical coherence tomography-based angiography for in vivo imaging applications". *Biomed Opt Express* 7:5, 2016, p. 1905. DOI: 10.1364/boe.7.001905.

86. V. Jaedicke, S. Agcaer, F. Robles, M. Steinert, D. Jones, S. Goebel, and M. Hofmann. "Comparison of different metrics for analysis and visualization in spectroscopic optical coherence tomography". *Biomedical Optics Express* 4:12, 2013, p. 2945.

87. S. Jespersen and L. Østergaard. "The roles of cerebral blood flow, capillary transit time heterogeneity, and oxygen tension in brain oxygenation and metabolism". *Journal of Cerebral Blood Flow and Metabolism* 32, 2012, pp. 264–277. DOI: 10.1038/jcbfm.2011.153.

88. M. J. Joyner, N. M. Dietz, and J. T. Shepherd. "From Belfast to Mayo and beyond: The use and future of plethysmography to study blood flow in human limbs". *J. Appl. Physiol.* 91, 2001, pp. 2431–2441. DOI: 10.1152/jappl.2001.91.6.2431.

89. A. J. Kadic, M. Boric, M. Vidak, L. Ferhatovic, and L. Puljak. "Changes in epidermal thickness and cutaneous innervation during maturation in long-term diabetes". *J Tissue Viability* 23:1, 2014, pp. 7–12. DOI: 10.1016/j.jtv.2013.11.002.

90. H. Kagan and R. Hajjar. "Coronary capillary blood flow in a rat model of congestive heart failure". *Journal of Applied Physiology* 124, 2018, pp. 632–640.

91. N. Kalia. "A historical review of experimental imaging of the beating heart coronary microcirculation in vivo". *Journal of Anatomy* 242:1, 2023, pp. 3–16. DOI: 10.1111/joa.13801.

92. J. Kalkman. "Fourier-Domain Optical Coherence Tomography Signal Analysis and Numerical Modeling". *International Journal of Optics* 2017:1, 2017, p. 9586067.

93. J. Kalkman, A. Bykov, D. Faber, and T. Leeuwen. “Multiple and dependent scattering effects in Doppler optical coherence tomography”. *Optics Express* 18:4, 2010, p. 3883.

94. A. A. Kamshilin, T. V. Krasnikova, M. A. Volynsky, S. V. Miridonov, and O. V. Mamontov. “Alterations of blood pulsations parameters in carotid basin due to body position change”. *Sci. Rep.* 8:13663, 2018, pp. 1–9. DOI: 10.1038/s41598-018-32036-7.

95. M. Kassinopoulos, E. Bousi, I. Zouvani, and C. Pitris. “Correlation of the derivative as a robust estimator of scatterer size in optical coherence tomography (OCT) [invited]”. *Biomedical Optics Express* 8:3, 2017, p. 1598.

96. D. Kavanagh, A. Lokman, G. Neag, A. Colley, and N. Kalia. “Imaging the injured beating heart intravitally and the vasculoprotection afforded by haematopoietic stem cells”. *Cardiovascular Research* 115, 2019, pp. 1918–1932. DOI: 10.1093/cvr/cvz118.

97. K. M. Kennedy et al. “Quantitative micro-elastography: Imaging of tissue elasticity using compression optical coherence elastography”. *Sci Rep* 5, 2015. DOI: 10.1038/srep15538.

98. M. A. Kirby et al. “Probing elastic anisotropy of human skin in vivo with light using non-contact acoustic micro-tapping OCE and polarization sensitive OCT”. *Sci Rep* 12:1, 2022. DOI: 10.1038/s41598-022-07775-3.

99. M. Kislevitz, Y. Akgul, C. Wamsley, J. Hoopman, and J. Kenkel. “Use of Optical Coherence Tomography (OCT) in Aesthetic Skin Assessment—A Short Review”. *Lasers in Surgery and Medicine* 52:8, 2020, pp. 699–704. DOI: 10.1002/lsm.23219.

100. S. Koudstaal and S. Chamuleau. “Assessment of coronary microvascular resistance in the chronic infarcted pig heart”. *Journal of Cellular and Molecular Medicine* 17, 2013, pp. 1128–1135.

101. I. L. Kruglikov and P. E. Scherer. “Skin aging as a mechanical phenomenon: The main weak links”. *Nutr Healthy Aging* 4:4, 2018, pp. 291–307. DOI: 10.3233/NHA-170037.

102. M. Kuck et al. “Evaluation of optical coherence tomography as a non-invasive diagnostic tool in cutaneous wound healing”. *Skin Research and Technology* 20:1, 2014, pp. 1–7. DOI: 10.1111/srt.12077.

103. M. Kuck et al. “Evaluation of optical coherence tomography as a non-invasive diagnostic tool in cutaneous wound healing”. *Skin Research and Technology* 20:1, 2014, pp. 1–7. DOI: 10.1111/srt.12077.

104. M. A. Laflamme and C. E. Murry. “Heart regeneration”. *Nature* 473:7347, 2011, pp. 326–335. DOI: 10.1038/nature10147.

105. N. Lai, G. M. Saidel, M. Iorio, and M. E. Cabrera. “Non-invasive estimation of metabolic flux and blood flow in working muscle: Effect of blood-tissue distribution”. In: *Adv. Exp. Med. Biol.* Vol. 645. 2009, pp. 155–160. DOI: 10.1007/978-0-387-85998-9_24.

106. M. H. Laughlin et al. “Peripheral circulation”. *Compr. Physiol.* 2:1, 2012, pp. 321–447. DOI: 10.1002/cphy.c100048.

107. C. K. Lee et al. “Evaluation of moisture-related attenuation coefficient and water diffusion velocity in human skin using optical coherence tomography”. *Sensors (Switzerland)* 13:4, 2013, pp. 4041–4050. DOI: 10.3390/s130404041.

108. P. Lee, W. Gao, and X. Zhang. “Performance of single-scattering model versus multiple-scattering model in the determination of optical properties of biological tissue with optical coherence tomography”. *Applied Optics* 49:18, 2010, pp. 3538–3544.

109. S. Lee, C. Vinegoni, P. Feruglio, L. Fexon, R. Gorbatov, M. Pivoravov, A. Sbarbati, M. Nahrendorf, and R. Weissleder. “Real-time in vivo imaging of the beating mouse heart at microscopic resolution”. *Nature Communications* 3, 2012. DOI: 10.1038/ncomms2060.

110. J. L. Lévêque. “EEMCO guidance for the assessment of skin topography”. *Journal of the European Academy of Dermatology and Venereology* 12:2, 1999, pp. 103–114. DOI: 10.1111/j.1468-3083.1999.tb00998.x.

111. J. L. Lévêque and B. Querleux. “SkinChip®, a new tool for investigating the skin surface in vivo”. *Skin Research and Technology* 9:4, 2003, pp. 343–347. DOI: 10.1034/j.1600-0846.2003.00043.x.

112. J. R. Levick and C. C. Michel. “The effects of position and skin temperature on the capillary pressures in the fingers and toes”. *J. Physiol.* 274, 1978, pp. 97–109. DOI: 10.1113/jphysiol.1978.sp012136.

113. W. Li, D. Goldstein, and D. Kreisel. “Intravital 2-photon imaging, leukocyte trafficking, and the beating heart”. *Trends in Cardiovascular Medicine* 23, 2013, pp. 287–293.

114. Y. Li, P. Tang, S. Song, A. Rakymzhan, and R. Wang. “Electrically tunable lens integrated with optical coherence tomography angiography for cerebral blood flow imaging in deep cortical layers in mice”. *Optics Letters* 44, 2019, pp. 5037–5040. DOI: 10.1364/OL.44.005037.

115. Y. Li, W. Wei, and R. Wang. “Capillary flow homogenization during functional activation revealed by optical coherence tomography angiography based capillary velocimetry”. *Scientific Reports* 8, 2018. DOI: 10.1038/s41598-018-22513-4.

116. Y. Li et al. “Aging-associated changes in cerebral vasculature and blood flow as determined by quantitative optical coherence tomography angiography”. *Neurobiol Aging* 70, 2018, pp. 148–159. DOI: 10.1016/j.neurobiolaging.2018.06.017.

117. Y. Li, P. Tang, S. Song, A. Rakymzhan, and R. K. Wang. “Electrically tunable lens integrated with optical coherence tomography angiography for cerebral blood flow imaging in deep cortical layers in mice”. *Opt Lett* 44:20, 2019, pp. 5037–5040. DOI: 10.1364/OL.44.005037.

118. Y. Li, P. Tang, S. Song, A. Rakymzhan, and R. K. Wang. “Electrically tunable lens integrated with optical coherence tomography angiography for cerebral blood flow imaging in deep cortical layers in mice”. *Opt. Lett.* 44:20, 2019, pp. 5037–5040. DOI: 10.1364/OL.44.005037.

119. R. Liao, B. Podesser, and C. Lim. "The continuing evolution of the Langendorff and ejecting murine heart: new advances in cardiac phenotyping". *American Journal of Physiology-Heart and Circulatory Physiology* 303, 2012, pp. 156–167. DOI: 10.1152/ajpheart.00333.2012.

120. A. J. Licup et al. "Stress controls the mechanics of collagen networks". *Proc Natl Acad Sci U S A* 112:31, 2015, pp. 9573–9578. DOI: 10.1073/pnas.1504258112.

121. A. L. Lopez, S. Wang, and I. V. Larina. "Embryonic mouse cardiodynamic OCT imaging". *Journal of Cardiovascular Development and Disease* 7:4, 2020, pp. 1–19. DOI: 10.3390/jcdd7040042.

122. J. Lu et al. "Application of OCT-Derived Attenuation Coefficient in Acute Burn-Damaged Skin". *Lasers Surg Med* 53:9, 2021, pp. 1192–1200. DOI: 10.1002/lsm.23415.

123. P. Marchand, D. Szlag, J. Extermann, A. Bouwens, D. Nguyen, M. Rudin, and T. Lasser. "Imaging of cortical structures and microvasculature using extended-focus optical coherence tomography at 13 m". *Optics Letters* 43, 2018, p. 1782. DOI: 10.1364/ol.43.001782.

124. P. Marchand, D. Szlag, J. Extermann, A. Bouwens, D. Nguyen, M. Rudin, and T. Lasser. "Imaging of cortical structures and microvasculature using extended-focus optical coherence tomography at 13 m". *Optics Letters* 43, 2018, p. 1782. DOI: 10.1364/ol.43.001782.

125. C. Mätzler. *MATLAB Functions for Mie Scattering and Absorption*. Technical report IAP Research Report No. 8. University of Bern, 2002.

126. S. C. Millasseau, R. P. Kelly, J. M. Ritter, and P. J. Chowienczyk. "Determination of age-related increases in large artery stiffness by digital pulse contour analysis". *Clin. Sci.* 103:4, 2002, pp. 371–377. DOI: 10.1042/cs1030371.

127. S. C. Millasseau, J. M. Ritter, K. Takazawa, and P. J. Chowienczyk. "Contour analysis of the photoplethysmographic pulse measured at the finger". *J. Hypertens.* 24:8, 2006, pp. 1449–1456. DOI: 10.1097/01.hjh.0000239277.05068.87.

128. W. P. Miller, S. H. Nellis, A. J. Liedtke, L. Whitesell, B. A. Effron, and B. A. E. Coro. *Coronary hyperperfusion and ventricular function in intact and isovolumic pig hearts*. 1990.

129. W. Miller, S. Nellis, A. Liedtke, L. Whitesell, B. Effron, and B. Coro. "Coronary hyperperfusion and ventricular function in intact and isovolumic pig hearts". *Journal Name*, 1990.

130. J. Monnier et al. "In vivo characterization of healthy human skin with a novel, non-invasive imaging technique: line-field confocal optical coherence tomography". *Journal of the European Academy of Dermatology and Venereology* 34:12, 2020, pp. 2914–2921. DOI: 10.1111/jdv.16857.

131. W. Murray and P. A. Foster. "The peripheral pulse wave: Information overlooked". *J. Clin. Monit.* 12, 1996, pp. 365–377. DOI: 10.1007/BF02077634.

132. I. Nehrhoff, D. Bocancea, J. Vaquero, J. Vaquero, J. Ripoll, M. Desco, and M. Gómez-Gaviro. "3D imaging in CUBIC-cleared mouse heart tissue: going deeper". *Biomedical Optics Express* 7, 2016, p. 3716. DOI: 10.1364/boe.7.003716.

133. R. T. Netea, J. W. M. Lenders, P. Smits, and T. Thien. "Both body and arm position significantly influence blood pressure measurement". *J. Hum. Hypertens.* 17:7, 2003, pp. 459–462. DOI: 10.1038/sj.jhh.1001573.

134. G. Niccoli and F. Crea. "Myocardial No-Reflow in Humans". *Journal of the American College of Cardiology* 54, 2009, pp. 281–292.

135. N. Nicolas and E. Roux. "3D imaging and quantitative characterization of mouse capillary coronary network architecture". *Biology (Basel)* 10, 2021.

136. C. Olianti and L. Sacconi. "3D imaging and morphometry of the heart capillary system in spontaneously hypertensive rats and normotensive controls". *Scientific Reports* 10, 2020.

137. L. Østergaard and H. Bøtker. "The role of capillary transit time heterogeneity in myocardial oxygenation and ischemic heart disease". *Basic Research in Cardiology* 109, 2014.

138. T. Phan et al. “Characterizing reduced scattering coefficient of normal human skin across different anatomic locations and Fitzpatrick skin types using spatial frequency domain imaging”. *J Biomed Opt* 26:02, 2021. DOI: 10.1117/1.jbo.26.2.026001.

139. M. Potente, H. Gerhardt, and P. Carmeliet. “Basic and therapeutic aspects of angiogenesis”. *Cell* 146:6, 2011, pp. 873–887. DOI: 10.1016/j.cell.2011.08.039.

140. F. Pouradier et al. “Functional and structural age-related changes in the scalp skin of Caucasian women”. *Skin Research and Technology* 19:4, 2013, pp. 384–393. DOI: 10.1111/srt.12057.

141. A. Pries, W. Kuebler, and H. Habazettl. “Coronary Microcirculation in Ischemic Heart Disease”. *Current Pharmaceutical Design* 24, 2018, pp. 2893–2899. DOI: 10.2174/1381612824666180625142341.

142. W. Qin and R. Wang. “Depth-resolved 3D visualization of coronary microvasculature with optical microangiography”. *Physics in Medicine Biology* 61, 2016, p. 7536. DOI: 10.1088/0031-9155/61/21/7536.

143. W. Qin, M. A. Roberts, X. Qi, C. E. Murry, Y. Zheng, and R. K. Wang. “Depth-resolved 3D visualization of coronary microvasculature with optical microangiography”. *Phys Med Biol*, 2016. DOI: 10.1088/0031-9155/61/21/7536.

144. e. a. R. K. Wang S. L. Jacques. “Three dimensional optical angiography”. *Opt Express* 15:7, 2007, p. 4083. DOI: 10.1364/oe.15.004083.

145. M. Redd, N. Zeinstra, W. Qin, W. Wei, A. Martinson, Y. Wang, R. Wang, C. Murry, and Y. Zheng. “Patterned human microvascular grafts enable rapid vascularization and increase perfusion in infarcted rat hearts”. *Nature Communications* 10, 2019. DOI: 10.1038/s41467-019-08388-7.

146. R. Reif and R. Wang. “Quantifying optical microangiography images obtained from a spectral domain optical coherence tomography system”. *International Journal of Biomedical Imaging* 2012, 2012.

147. A. Reisner, P. A. Shaltis, D. McCombie, and H. H. Asada. “Utility of the photoplethysmogram in circulatory monitoring”. *Anesthesiology* 108:5, 2008, pp. 950–958. DOI: 10.1097/ALN.0b013e31816c89e1.

148. C. Ruini et al. “In-vivo lc-oct evaluation of the downward proliferation pattern of keratinocytes in actinic keratosis in comparison with histology: First impressions from a pilot study”. *Cancers (Basel)* 13:12, 2021. DOI: 10.3390/cancers13122856.

149. H. R. S. H. Mathes and U. Graf-Hausner. “The use of skin models in drug development”. *Adv Drug Deliv Rev*, 2014. DOI: 10.1016/j.addr.2013.12.006.

150. e. a. S. Truzzi. “Handheld contact-type OCT and color fundus system for retinal imaging”. *Biomed Opt Express* 15:4, 2024, p. 2681. DOI: 10.1364/BOE.520735.

151. J. Q. S. Yousefi and R. K. Wang. “Super-resolution spectral estimation of optical microangiography for quantifying blood flow within microcirculatory tissue beds in vivo”. *Biomed Opt Express* 4:7, 2013, pp. 1214–1228. DOI: 10.1364/boe.4.001214.

152. M. E. Safar. “Arterial aging-hemodynamic changes and therapeutic options”. *Nat. Rev. Cardiol.* 7, 2010, pp. 442–449. DOI: 10.1038/nrcardio.2010.96.

153. S. Sakai et al. “In vivo three-dimensional birefringence analysis shows collagen differences between young and old photo-aged human skin”. *Journal of Investigative Dermatology* 128:7, 2008, pp. 1641–1647. DOI: 10.1038/jid.2008.8.

154. J. Sandby-Møller, T. Poulsen, and H. C. Wulf. “Epidermal Thickness at Different Body Sites: Relationship to Age, Gender, Pigmentation, Blood Content, Skin Type and Smoking Habits”. *Acta Derm Venereol* 83:6, 2003, pp. 410–413. DOI: 10.1080/00015550310015419.

155. J. Sandby-Møller, T. Poulsen, and H. C. Wulf. “Influence of Epidermal Thickness, Pigmentation and Redness on Skin Autofluorescence”. *Photochem Photobiol* 77:6, 2007, pp. 616–620. DOI: 10.1562/0031-8655(2003)0770616ioetpa2.0.co2.

156. R. Schramm, M. Menger, S. Kirsch, F. Langer, Y. Harder, J. Hamacher, and H. Schäfers. "The subepicardial microcirculation in heterotopically transplanted mouse hearts: An intravital multifluorescence microscopy study". *Journal of Thoracic and Cardiovascular Surgery* 134, 2007. DOI: 10.1016/j.jtcvs.2007.02.018.

157. e. a. Schuetzenberger. "Comparison of optical coherence tomography and high frequency ultrasound imaging in mice for the assessment of skin morphology and intradermal volumes". *Scientific Reports* 9:1, 2019, p. 13643. DOI: 10.1038/s41598-019-50055-7.

158. I. L. Shlivko et al. "Complex assessment of age-specific morphofunctional features of skin of different anatomic localizations". *Skin Research and Technology* 19:1, 2013. DOI: 10.1111/j.1600-0846.2012.00613.x.

159. M. Silva and L. Gonçalves. "Microcirculation function assessment in acute myocardial infarction: A systematic review". *Frontiers in Cardiovascular Medicine* 9, 2022.

160. T. Son and B. Jung. "Cross-evaluation of optimal glycerol concentration to enhance optical tissue clearing efficacy". *Skin Research and Technology* 21, 2015, pp. 327–332. DOI: 10.1111/srt.12196.

161. S. Song, J. Xu, and R. Wang. "Long-range and wide field of view optical coherence tomography for in vivo 3D imaging of large volume object based on akinetic programmable swept source". *Biomedical Optics Express*, 2016. DOI: 10.1364/boe.7.004734.

162. S. Song, J. Xu, S. Men, T. T. Shen, and R. K. Wang. "Robust numerical phase stabilization for long-range swept-source optical coherence tomography". *J. Biophotonics* 10:11, 2017, pp. 1398–1410. DOI: 10.1002/jbio.201700034.

163. S. Song, J. Xu, and R. K. Wang. "Long-range and wide field of view optical coherence tomography for in vivo 3D imaging of large volume object based on akinetic programmable swept source". *Biomed Opt Express*, 2016. DOI: 10.1364/boe.7.004734.

164. T. Stiermaie, H. Thiele, and I. Eitel. "Coronary Microvascular Obstruction". *Circulation: Cardiovascular Imaging* 10, 2017, pp. 1–2.

165. M. G. S. J. Sutton and N. Sharpe. “Left ventricular remodeling after myocardial infarction: Pathophysiology and therapy”. *Circulation*, 2000. DOI: 10.1161/01.cir.101.25.2981.

166. S. A. Taqi, S. A. Sami, L. B. Sami, and S. A. Zaki. “A review of artifacts in histopathology”. *Journal of Oral and Maxillofacial Pathology* 22:2, 2018, p. 279. DOI: 10.4103/jomfp.JOMFP_125_15.

167. S. Taqi, S. Sami, L. Sami, and S. Zaki. “A review of artifacts in histopathology”. *Journal of Oral and Maxillofacial Pathology* 22, 2018, p. 279.

168. L. Thrane, H. T. Yura, and P. E. Andersen. “Analysis of optical coherence tomography systems based on the extended Huygens–Fresnel principle”. *JOSA A* 17:3, 2000, pp. 484–490.

169. P. H. Tomlins and R. K. Wang. “Theory, developments and applications of optical coherence tomography”. *J. Phys. D. Appl. Phys.* 38:15, 2005, pp. 2519–2535. DOI: 10.1088/0022-3727/38/15/002.

170. C. Trojahn, G. Dobos, C. Richter, U. Blume-Peytavi, and J. Kottner. “Measuring skin aging using optical coherence tomography in vivo: a validation study”. *J Biomed Opt* 20:4, 2015, p. 045003. DOI: 10.1117/1.jbo.20.4.045003.

171. C. Vinegoni, A. Aguirre, S. Lee, and R. Weissleder. “Imaging the beating heart in the mouse using intravital microscopy techniques”. *Nature Protocols* 10, 2015, pp. 1802–1819. DOI: 10.1038/nprot.2015.119.

172. D. Výbohová, M. Adamkov, and G. Hešková. *Qualitative changes of the capillary bed in aging human skin*. 2012. DOI: 10.14670/HH-27.961.

173. R. K. Wang, S. L. Jacques, Z. Ma, S. Hurst, S. R. Hanson, and A. Gruber. “Three-dimensional optical angiography”. *Opt Express* 15:7, 2007, p. 4083. DOI: 10.1364/oe.15.004083.

174. R. K. Wang, Q. Zhang, Y. Li, and S. Song. “Optical coherence tomography angiography-based capillary velocimetry”. *J. Biomed. Opt.* 22:6, 2017, p. 66008. DOI: 10.1117/1.jbo.22.6.066008.

175. R. K. Wang, Q. Zhang, Y. Li, and S. Song. “Optical coherence tomography angiography-based capillary velocimetry”. *J Biomed Opt* 22:6, 2017, p. 66008. DOI: 10.1117/1.jbo.22.6.066008.

176. R. K. Wang, Q. Zhang, Y. Li, and S. Song. “Optical coherence tomography angiography-based capillary velocimetry”. *J Biomed Opt* 22:6, 2017, p. 066008. DOI: 10.1117/1.jbo.22.6.066008.

177. R. Wang. “Optical microangiography: A label-free 3-D imaging technology to visualize and quantify blood circulations within tissue beds in vivo”. *IEEE Journal on Selected Topics in Quantum Electronics* 16, 2010, pp. 545–554. DOI: 10.1109/JSTQE.2009.2033609.

178. R. Wang and S. Song. “Optical coherence tomography angiography-based capillary velocimetry”. *Journal of Biomedical Optics* 22, 2017, p. 066008. DOI: 10.1117/1.jbo.22.6.066008.

179. R. Wang and S. Song. “Optical coherence tomography angiography-based capillary velocimetry”. *Journal of Biomedical Optics* 22, 2017, p. 66008. DOI: 10.1117/1.jbo.22.6.066008.

180. Y. Wang, S. Wei, and J. U. Kang. “Depth-dependent attenuation and backscattering characterization of optical coherence tomography by stationary iterative method”. *Journal of Biomedical Optics* 28:8, 2023, p. 085002.

181. A. Watson. “Perimetric Complexity of Binary Digital Images”. *Math J* 14, 2012. DOI: 10.3888/tmj.14-5.

182. J. Welzel, M. Bruhns, and H. H. Wolff. “Optical coherence tomography in contact dermatitis and psoriasis”. *Arch Dermatol Res* 295:2, 2003, pp. 50–55. DOI: 10.1007/s00403-003-0390-y.

183. X. Wu, M. R. Reboll, M. Korf-Klingebiel, and K. C. Wollert. “Angiogenesis after acute myocardial infarction”. *Cardiovascular Research* 117:5, 2021, pp. 1257–1273. DOI: 10.1093/cvr/cvaa287.

184. J. R. C. X. Yin and R. K. Wang. "User-guided segmentation for volumetric retinal optical coherence tomography images". *J Biomed Opt* 19:8, 2014, p. 086020. DOI: 10.1117/1.jbo.19.8.086020.

185. M. X. Xiao, H. C. Wei, Y. J. Xu, H. T. Wu, and C. K. Sun. "Combination of R-R interval and crest time in assessing complexity using multiscale cross-approximate entropy in normal and diabetic subjects". *Entropy* 20:7, 2018, p. 497. DOI: 10.3390/e20070497.

186. Z. Xie and R. Wang. "Quantifying Microvascular Structure in Healthy and Infarcted Rat Hearts Using Optical Coherence Tomography Angiography". *IEEE Transactions on Medical Imaging*, 2024.

187. J. Xu, W. Wei, S. Song, X. Qi, and R. Wang. "Scalable wide-field optical coherence tomography-based angiography for in vivo imaging applications". *Biomedical Optics Express* 7, 2016, p. 1905. DOI: 10.1364/boe.7.001905.

188. J. Xu, W. Wei, S. Song, X. Qi, and R. K. Wang. "Scalable wide-field optical coherence tomography-based angiography for in vivo imaging applications". *Biomed Opt Express* 7:5, 2016, p. 1905. DOI: 10.1364/boe.7.001905.

189. X. Xu and R. K. Wang. "Synergistic effect of hyperosmotic agents of dimethyl sulfoxide and glycerol on optical clearing of gastric tissue studied with near infrared spectroscopy". *Phys Med Biol* 49:3, 2004, pp. 457–468. DOI: 10.1088/0031-9155/49/3/008.

190. X. Xu and R. K. Wang. "The role of water desorption on optical clearing of biotissue: Studied with near infrared reflectance spectroscopy". *Med Phys* 30:6, 2003, pp. 1246–1253. DOI: 10.1118/1.1576228.

191. e. a. Y. Shi. "Integrating a pressure sensor with an OCT handheld probe to facilitate imaging of microvascular information in skin tissue beds". *Biomed Opt Express* 13:11, 2022, p. 6153. DOI: 10.1364/boe.473013.

192. Y. Yang, T. Wang, N. Biswal, X. Wang, M. Sanders, M. Brewer, and Q. Zhu. "Optical scattering coefficient estimated by optical coherence tomography correlates with collagen content in ovarian tissue". *Journal of Biomedical Optics* 16:9, 2011, p. 090504.

193. J. Yi and V. Backman. "Imaging a full set of optical scattering properties of biological tissue by inverse spectroscopic optical coherence tomography". *Optics Letters* 37:21, 2012, p. 4443.

194. X. Yin, J. R. Chao, and R. K. Wang. "User-guided segmentation for volumetric retinal optical coherence tomography images". *J Biomed Opt* 19:8, 2014, p. 086020. DOI: 10.1117/1.jbo.19.8.086020.

195. S. Yousefi, J. Qin, and R. K. Wang. "Super-resolution spectral estimation of optical microangiography for quantifying blood flow within microcirculatory tissue beds in vivo". *Biomed. Opt. Express* 4:7, 2013, pp. 1214–1228. DOI: 10.1364/boe.4.001214.

196. S. Yousefi and R. K. Wang. "Simultaneous estimation of bidirectional particle flow and relative flux using MUSIC-OCT: Phantom studies". *Phys. Med. Biol.* 59:22, 2014, pp. 6693–6708. DOI: 10.1088/0031-9155/59/22/6693.

197. S. Yousefi, Z. Zhi, and R. K. Wang. "Eigendecomposition-based clutter filtering technique for optical microangiography". *IEEE Trans Biomed Eng* 58:8, 2011, pp. 2316–2323. DOI: 10.1109/TBME.2011.2152839.

198. S. Yousefi, Z. Zhi, and R. K. Wang. "Eigendecomposition-based clutter filtering technique for optical microangiography". *IEEE Trans. Biomed. Eng.* 58:8, 2011, pp. 2316–2323. DOI: 10.1109/TBME.2011.2152839.

199. X. Yu et al. "Multiscale skin imaging in vivo using optical coherence tomography". *Laser Phys Lett* 15:7, 2018. DOI: 10.1088/1612-202X/aabb2f.

200. X. Yu et al. "Multiscale skin imaging in vivo using optical coherence tomography". *Laser Phys Lett* 15:7, 2018. DOI: 10.1088/1612-202X/aabb2f.

201. Y. Z and R. Wang. “Eigendecomposition-based clutter filtering technique for optical microangiography”. *IEEE Transactions on Biomedical Engineering* 58, 2011, pp. 2316–2323. DOI: 10.1109/TBME.2011.2152839.

202. e. a. Z. Xie. “Optical coherence tomography angiography measures blood pulsatile waveforms at variable tissue depths”. *Quant Imaging Med Surg* 11:3, 2021, pp. 907–917. DOI: 10.21037/QIMS-20-778.

203. P. Zakharov, M. S. Talary, I. Kolm, and A. Caduff. “Full-field optical coherence tomography for the rapid estimation of epidermal thickness: Study of patients with diabetes mellitus type 1”. *Physiol Meas* 31:2, 2010, pp. 193–205. DOI: 10.1088/0967-3334/31/2/006.

204. N. Zeinstra, A. Frey, Z. Xie, L. Blakely, R. Wang, C. Murry, and Y. Zheng. “Stacking thick perfusable human microvascular grafts enables dense vascularity and rapid integration into infarcted rat hearts”. *Biomaterials* 301, 2023. DOI: 10.1016/j.biomaterials.2023.122250.

205. A. Zhang, Q. Zhang, C.-L. Chen, and R. K. Wang. “Methods and algorithms for optical coherence tomography-based angiography: a review and comparison”. *J Biomed Opt* 20:10, 2015, p. 100901. DOI: 10.1117/1.jbo.20.10.100901.

206. A. Zhang, Q. Zhang, C.-L. Chen, and R. K. Wang. “Methods and algorithms for optical coherence tomography-based angiography: a review and comparison”. *J Biomed Opt* 20:10, 2015, p. 100901. DOI: 10.1117/1.jbo.20.10.100901.

207. A. Zhang, Q. Zhang, and R. K. Wang. “Minimizing projection artifacts for accurate presentation of choroidal neovascularization in OCT micro-angiography”. *Biomed. Opt. Express* 6:10, 2015, pp. 4130–4143. DOI: 10.1364/boe.6.004130.

208. Q. Zhang et al. “Projection Artifact Removal Improves Visualization and Quantitation of Macular Neovascularization Imaged by Optical Coherence Tomography Angiography”. *Ophthalmol. Retin.* 1:2, 2017, pp. 124–136. DOI: 10.1016/j.oret.2016.08.005.

209. Q. Zhang, J. Wang, and R. K. Wang. "Highly efficient eigen decomposition based statistical optical microangiography". *Quant Imaging Med Surg* 6:5, 2016, pp. 557–563. DOI: 10.21037/qims.2016.10.03.